

Numerical investigation of buoyancy induced turbulent flows in partially open enclosures

R.Harish

A Dissertation Submitted to
Indian Institute of Technology Hyderabad
In Partial Fulfillment of the Requirements for
The Degree of Doctor of Philosophy

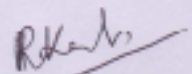


Department of Mechanical & Aerospace Engineering

August 2014

Declaration

I declare that this written submission represents my ideas in my own words, and where ideas or words of others have been included, I have adequately cited and referenced the original sources. I also declare that I have adhered to all principles of academic honesty and integrity and have not misrepresented or fabricated or falsified any idea/data/fact/source in my submission. I understand that any violation of the above will be a cause for disciplinary action by the Institute and can also evoke penal action from the sources that have thus not been properly cited, or from whom proper permission has not been taken when needed.



(Signature)

R. HARISH

(Student Name)

ME10P005

(Roll No.)

Approval Sheet

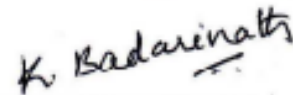
This dissertation entitled "Numerical investigation of buoyancy induced turbulent flows in partially open enclosures" by R.Harish is approved for the degree of Doctor of Philosophy from IIT Hyderabad.



Prof. S.Vengadesan (External Examiner)
Department of Applied Mechanics
Indian Institute of Technology Madras



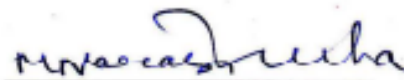
Prof. Manab Kumar Das (External Examiner)
Department of Mechanical Engineering
Indian Institute of Technology Kharagpur



Dr. Karri Badarinath (Internal Examiner)
Department of Mechanical & Aerospace Engineering
Indian Institute of Technology Hyderabad



Dr. K. Venkatasubbaiah (Adviser)
Department of Mechanical & Aerospace Engineering
Indian Institute of Technology Hyderabad



Dr. Narasimha Mangadoddy (Chairman)
Department of Chemical Engineering
Indian Institute of Technology Hyderabad

Acknowledgements

I express my sincere gratitude to my adviser Dr.K.Venkatasubbaiah for his valuable guidance, support and encouragement throughout my research. His interest and confidence in me has helped immensely for the successful completion of this work.

I would like to thank my doctoral committee members, Prof. Vinayak Eswaran, Dr. Raja Banerjee and Dr.Narasimha Mangadoddy for their insightful comments and valuable suggestion during my research.

I am grateful to Prof.U.B.Desai (Director, Indian Institute of Technology Hyderabad) for providing good research environment and excellent facilities. I am also grateful to MHRD for providing scholarship during my PhD program.

I would also like to thank all my friends in IIT Hyderabad for making my stay at IIT Hyderabad, memorable and enjoyable.

Finally, I would like to thank my parents for their support, blessings and motivation throughout my work.

R.Harish

Dedicated To My Parents

Synopsis

The buoyancy induced turbulent flows in ventilated enclosure with internal heat source has important applications in building ventilations, solar energy receivers, thermal management of electronic devices and enclosure fire dynamics. In naturally ventilated buildings, the fluid flow is mainly driven by buoyancy and air exchange through ventilation openings provides thermal comfort for building occupants. During fire accidents in buildings and in long tunnels, larger temperature difference induces strong buoyant plumes and the hot gas flow characteristics are important for the design of fire safety and ventilation systems. The air flow patterns through vertical openings such as doorways and windows are widely studied but very few investigations are performed with horizontal or ceiling openings. The horizontal vents are openings in ceilings, floors or smoke vent at roof top. The flow patterns through horizontal openings are highly unstable in comparison with vertical openings. Previous investigations through horizontal openings have not considered the effects of heat source strength, vent aspect ratio, wind speed, wind direction, heat source and vent locations.

The objective of present study is to investigate thermal plume behavior in ceiling vented enclosures and stack effects in vertical shaft. Turbulence is modeled with Reynolds Averaged Navier-Stokes equation (RANS) with buoyancy modified Lam Bremhorst low Reynolds number $k - \epsilon$ model within the frame work of Boussinesq approximation. The finite difference technique is used to solve the governing equations and solver is developed in Fortran 90. The non-linear convective terms are evaluated using optimal upwind compact schemes (OUCS-3). In case of ceiling vented square enclosure, Grashof number is varied from $Gr = 10^8$ to 10^{10} . The plume patterns are investigated for four different heat source and vent locations (0.25H, 0.5H, 0.625H & 0.75H). The bidirectional exchange across openings rises with increase in Grashof number. The present study identified significant change in plume characteristics by varying heat source and vent locations. The plume discharge rate from centrally located vent and heat source (0.5H) are higher than near wall locations (0.25H & 0.75H). The normal velocity and temperature profiles across horizontal vent decreases with increase in vent thickness. The buoyant flows in vertical shaft connected to rectangular compartment generate wall plume structure with multi-recirculating convective cell pattern. The height of vertical passage and rectangular compartment location had significant effect on thermal plume transport phenomena. This study identified that ceiling vent is preferred for effective removal of plume from rectangular compartment. The present numerical

results are validated and are in good agreement with experimental and numerical results available in literature.

For buoyant flows with high temperature difference, it is inappropriate to evaluate density variations with Boussinesq approximation. Hence, further investigations are performed with non-Boussinesq variable density approach suitable for low Mach number flows. The density changes are evaluated from equation of state. A pressure based solver is developed with Simplified Marker and Cell (SMAC) algorithm on collocated grid. The variable density code is tested to study buoyancy driven mixing through horizontal passage between two enclosures filled with hot and cold fluid. The Grashof number is varied from $Gr = 10^6$ to 5×10^7 and the critical Grashof number is identified as 10^7 . The Gay-Lussac number ($Ga = \beta\Delta T$) is varied from 0.04 to 0.2. The nonlinear exchanges across the horizontal passage are investigated by varying vent aspect ratio. The vent width is varied from $D=0.05H$ to $0.2H$. The flow stabilizes for vent width $D=0.05H$ and hence bidirectional exchange is reduced across the horizontal passage. Chaotic flow originates for critical vent widths $0.1H \leq D \leq 0.15H$, and nonlinear oscillations evolves till the system reaches quasi-steady state. Meanwhile, vent width $D=0.2H$ reduces flow perturbations and facilitates balanced flow across the vent. A new vortex structure is observed across horizontal passage between time intervals $\tau=20 - 40$ & $80 - 100$ and it evolves in cyclic pattern. The flow rate between two enclosures increases by reducing the horizontal passage thickness.

The variable density code is further extended by incorporating Lam Bremhorst low Reynolds number $k - \epsilon$ model to simulate turbulent combined convection flows in ceiling vented square enclosure with forced inlet port. The results are presented for Grashof number $Gr = 10^{11}$ & 10^{12} with corresponding Gay-Lussac number $Ga=0.2$ & 2 . The assisting and opposing effects of forced air stream on thermal plume behavior are analyzed by varying inlet velocity, inlet port size and location. The present model is valid when buoyancy effects are significant in comparison with forced convection effects. The dimensionless longitudinal velocity at inlet port is defined by parameter $\alpha = \frac{1}{\sqrt{Ri}}$; where $Ri = \frac{Gr}{Re^2}$ is the Richardson number. In assisting flow case, for $Gr = 10^{11}$ and α varied from 0.01 to 0.1, the average Nusselt number increases by 5.4% to 10.2% respectively. The average Nusselt number for $Gr = 10^{12}$ is 11 percent higher in comparison with $Gr = 10^{11}$. The inlet port height ($H_v = 0.2H$) enhances plume discharge rate and increases convective heat loss from cavity. The opposing flow weakens thermal buoyancy and minimizes convective heat

loss from cavity.

Three dimensional extension of the study is carried out with Fire dynamic simulator code (FDS). The FDS code simulates turbulent buoyant flows with Large Eddy Simulation(LES) model. The FDS code is used to study buoyant flows in tunnel with single and multiple roof openings. The tunnel is 100m long, 3m wide and 2.5m high. The plume characteristics are investigated by varying the roof opening size and heat source locations. For centrally located ceiling vent and heat source, the plume longitudinal velocity is decreased by 41.6%. For heat source located at 55m and 60m, upstream longitudinal velocity decreased by 25% and 45.8% and downstream velocity decreased by 10% and 4.1%. This study identified that single roof opening is insufficient to exhaust all gases when the longitudinal distance between vent and heat source increases. Meanwhile, multiple roof openings are effective in venting hot gases and reduce plume velocity. Further investigations are performed in two chamber enclosure connected through horizontal passage by considering the combined effects of wind and thermal buoyancy. In assisting flow case, with heat source located inside lower enclosure forced air supplied at a velocity of $U = 0.2$ to 0.4 m/s through lower enclosure doorway assists the plume growth rate, meanwhile higher velocities ($U \geq 0.5$ m/s) diffuses the heat and reduces compartment temperature. For heat source placed in upper enclosure, forced air supplied at a velocity of 0.4 m/s through top enclosure doorway reverses the buoyancy force and accelerates the plume to propagate into the lower enclosure. The FDS code is also used to study the interactions between water droplets and thermal plume in a two compartmental enclosure connected to vertical shaft. The sprinkler flow rates and operating pressures are varied from 30 to 60 l/min and 1 to 1.6 bar respectively. This study determined that water droplets opposes buoyancy force, reduces plume discharge through openings. Water discharge rate of 60 l/min reduces horizontal vent mass flow rate by 59.46%. This study also identified that sprinkler operating pressure of 1.6 bar leads to smoke logging. The numerical model employed has been validated with previous results available in literature.

Referred publications

Journal Publications

1. **R. Harish**, K.Venkatasubbaiah, “Numerical simulation of turbulent plume spread in ceiling vented enclosure”, *European Journal of Mechanics - B/Fluids*, vol.42, pp: 142-158, 2013.
2. **R. Harish**, K.Venkatasubbaiah, “Mathematical modeling and computation of fire induced turbulent flow in partial enclosures”, *Applied Mathematical Modelling*, vol.37, pp: 9732-9746, 2013.
3. **R. Harish**, K.Venkatasubbaiah, “Transport phenomena of turbulent fire spread through compartment connected to vertical shaft in tall building”, *Fire Safety Journal*, vol.61, pp: 160-174, 2013.
4. **R. Harish**, K.Venkatasubbaiah, “Effects of buoyancy induced roof ventilation systems for smoke removal in tunnel fires”, *Tunnelling and Underground Space Technology*, vol.42, pp: 195-205, 2014.
5. **R. Harish**, K.Venkatasubbaiah, “Numerical investigation of instability patterns and nonlinear buoyant exchange flow between enclosures by variable density approach”, *Computers & Fluids*, vol.96, pp: 276-287, 2014.
6. **R. Harish**, K.Venkatasubbaiah, “Large Eddy Simulation of thermal plume behavior in horizontally partitioned dual enclosure” (under review).
7. **R. Harish**, K.Venkatasubbaiah, “Numerical study of water spray interaction with fire plume in dual chambers connected to tall shaft” (under review).
8. **R. Harish**, K.Venkatasubbaiah, “Non-Boussinesq model for turbulent buoyant flows in enclosure with horizontal vent and forced inlet port” (under review).

Conferences

1. **R. Harish**, K.Venkatasubbaiah, “Numerical Simulation of fire spread in elevator shaft connected to adjacent lobby in tall building”, *13th International Conference on Fire Science and Engineering (Interflam2013)*, 24-26 June 2013, Royal Holloway College, University of London, UK.
2. **R. Harish**, K.Venkatasubbaiah, “Entrainment effects through horizontal and vertical vents on turbulent natural convection flows”, *22nd National and 11th International ISHMT-ASME Heat and Mass Transfer Conference*, 28-31 December 2013, IIT-Kharagpur, India.

Nomenclature

$A.R$	Aspect ratio
C_μ	Model constant
D	Horizontal Vent width
g	Gravitational force per unit mass
Ga	Gay-Lussac's number
G_k	Production of turbulence due to buoyancy
Gr	Grashof number
H	Height of the enclosure
H_v	Height of vertical passage
k	Turbulent Kinetic energy
K	Dimensionless Turbulent Kinetic energy
P	Dimensionless pressure
P_k	Production of turbulent kinetic energy due to shear
Pr	Prandtl number
Pr_t	Turbulent Prandtl number
Ra	Rayleigh number
Ri	Richardson number
T_s	Heat source temperature
T_∞	Initial fluid temperature
u^*, v^*	Predicted longitudinal and normal velocities
U, V	Dimensionless velocity components along x and y directions
V_c	Free convection velocity
W	Width of the enclosure
β	coefficient of volumetric thermal expansion
μ	Dynamic viscosity
ν_t	Turbulent dynamic viscosity
δ_{ij}	Kronecker delta
μ_t	Turbulent eddy viscosity
ρ	Fluid density
ϵ	Turbulent dissipation rate
τ	Dimensionless time
θ	Dimensionless temperature
ε	Dimensionless Turbulent dissipation rate

List of Figures

2.1	Schematic diagram of square enclosure with ceiling vent.	11
2.2	Temperature (a) and vertical velocity (b) profiles along the horizontal surface for different grid sizes.	19
2.3	Validation of present results with: LBM a-c; Experimental d & e.	21
2.4	Evolution of stream function contours for $Gr = 10^8$	22
2.5	Evolution of temperature contours for $Gr = 10^8$	23
2.6	Evolution of vorticity contours for $Gr = 10^8$	24
2.7	Evolution of kinetic energy contours for $Gr = 10^8$	25
2.8	Stream function contours at different Grashof numbers.	26
2.9	Temperature contours at different Grashof numbers.	27
2.10	Normal velocity profile across the vent for $Gr = 10^{10}$	28
2.11	Non-dimensional net mass flow rate variation with time through the vent.	28
2.12	Effect of heat source location on: temperature contours (a-c); vertical velocity contours (d-f)	29
2.13	Non-dimensional net mass flow rate with diifferent heat source locations for $Gr = 10^8$	30
2.14	(a) Normal velocity profile; (b) Non-dimensional net mass flow rate with different vent locations for $Gr = 10^8$	31
2.15	(a) Normal velocity profiles across two vents; (b) Non-dimensional net mass flow rate through two vents for $Gr = 10^8$	32
2.16	Schematic diagram of square enclosure with vent thickness	32
2.17	Stream function(a&b), temperature(c&d), kinetic energy(e&f) contours in a square enclosure for $Gr = 10^8$. Variation of normal velocity (g) and temperature (h) profiles along the top vent with different vent thickness.	33
2.18	Schematic diagram of square enclosure with vertical and horizontal openings.	34
2.19	Evolution of Stream function contours in square enclosure	35

2.20	Evolution of Stream function contours in rectangular enclosure	36
2.21	Effect of aspect ratio on net mass flow rate (a) horizontal vent (b) vertical vent.	36
3.1	Schematic diagram of rectangular compartment connected to vertical shaft	38
3.2	Non-dimensional temperature profile at the mid-height for $Gr = 10^{11}$:(a) compartment and (b) Vertical shaft; (c) Non-dimensional net mass flow rate variation through vertical passage.	40
3.3	Validation of present non-dimensional results with:(a&b) Numerical (Xaman et al.[100]); (c&d) Experimental (Betts and Bokhari [101])	41
3.4	Temperature contours (a,b) at slice plane $Z=0.1$ for $Gr = 10^{11}$;(c) Non-dimensional temperature variation along shaft vertical axis.	42
3.5	Evolution of stream function contours for $Gr = 10^{10}$	43
3.6	Evolution of temperature contours for $Gr = 10^{10}$	43
3.7	Comparison of longitudinal velocity profiles across vertical passage for different Gr	44
3.8	Comparison of net mass flow rate across vertical passage for different Gr	45
3.9	Evolution of stream function contours (a,c), temperature contours(b,d) with vertical passage of height $H_v = 0.05H$ for $Gr = 10^{10}$	46
3.10	Comparison of net mass flow rate for different vertical passage size	46
3.11	Stream function (a) and temperature contours (b) with ceiling vent in the compartment for $Gr = 10^{10}$	47
3.12	Non-dimensional normal velocity profile across the ceiling vent in rectangular compartment.	48
3.13	Non-dimensional net mass flow rate through vertical and horizontal vents in rectangular compartment.	48
3.14	Stream function(a,b) and temperature(c,d) contours for shifted rectangular compartment.	49
4.1	Schematic diagram of two square enclosures connected through horizontal vent.	51
4.2	Grid independence: Temperature profile at the mid-height of lower enclosure.	56
4.3	(a) Stream function and (b) temperature contours for $Ra = 10^7$	57
4.4	Evolution of stream function contours for $Gr = 10^7$ between time intervals $\tau = 2 - 70$	59

4.5	Evolution of stream function contours for $Gr = 10^7$ between time intervals $\tau = 80 - 200$	60
4.6	Evolution of density contours for $Gr = 10^7$	61
4.7	(a&b) Density profile at mid-height of lower and upper enclosure for $Gr = 10^7$	62
4.8	Evolution of stream function contours for $Gr = 5 \times 10^7$	62
4.9	Evolution of density contours for $Gr = 5 \times 10^7$	63
4.10	(a) Comparison of normal velocity profile for different Gr; (b) Comparison of net mass flow rate for different Gr.	64
4.11	(a-c) Comparison of stream function contours for different Gr; (d-f) Comparison of density contours for different Gr.	65
4.12	Stream function contours for different vent widths $Gr = 2.5 \times 10^7$	66
4.13	Temperature contours for different vent widths $Gr = 2.5 \times 10^7$	67
4.14	(a) Comparison of net mass flow rate for different vent widths; (b) Comparison of normal velocity profiles for different vent widths	67
4.15	Density variation along the vertical axis for different vent size $Gr = 2.5 \times 10^7$	68
4.16	Stream function contours for zero vent thickness; $Gr = 10^7$	69
4.17	Comparison of net mass flow rate for different vent thickness and Grashof number.	69
5.1	Schematic diagram of rectangular compartment connected to vertical shaft	71
5.2	Evolution of stream function contours for different inlet velocities.	75
5.3	Evolution of temperature contours for different inlet velocities.	76
5.4	Comparison of midheight (a) temperature profile, (b)density profile and (c) net mass flow rates for different inlet velocities.	77
5.5	Comparison of midheight temperature profiles with Boussinesq and Non-Boussinesq approach.	78
5.6	Effect of Gr & α on (a) Midheight longitudinal velocity profile; (b)Normal velocity profiles across horizontal vent; (c) Net mass flow rates and (d) Average Nusselt number.	79
5.7	Comparison of midheight (a) temperature profile, (b) net mass flow rates and (c) average Nusselt number for different H_v & α	80
5.8	Evolution of stream function (a,b) and temperature (c,d) contours for $V_L = 0.75H$; $\alpha = 0.1$	81
5.9	Comparison of midheight (a) temperature distribution (b)net mass flow rate (c) average Nusselt number for different inlet port location & α	82

6.1	Schematic diagram of tunnel with roof openings 3-D view and 2-D view (dimensions in m).	85
6.2	Temperature variation towards the tunnel upstream side measured from heat source.	87
6.3	Validation of present results with experimental results	88
6.4	(a&b) Evolution of isosurfaces of thermal plume inside tunnel without ceiling vent (c&d) Evolution of isosurfaces of thermal plume inside tunnel with ceiling vent.	90
6.5	Temperature distribution along the entire length of tunnel.	91
6.6	(a) Mass flow rate through tunnel portals without roof opening; (b) Mass flow rate through tunnel portals with roof opening.	91
6.7	Comparison of temperature distribution inside roof vented tunnel with different heat source location: (a&b) Temperature contours along xz plane at $y=1.5$ m ; (c&d) Normal velocity contours along xy plane at $z=2.25$ m and (e&f) Temperature contours along yz plane.	92
6.8	(a) Mass flow rate through roof opening; (b) Temperature variation with time monitored by thermocouple at 30.0 m from tunnel entrance; (c) Temperature distribution along the entire tunnel.	93
6.9	(a-d) Comparison of temperature distribution inside multiple roof vented tunnel with different heat source location;(e) Comparison of mass flow rate through three roof openings for heat source placed at 55.0 m; (f) Comparison of mass flow rate through three roof openings for heat source placed at 60.0 m	95
6.10	(a) Comparison of mass flow rate through central roof opening for two vent sizes; (b) Temperature variation with time monitored by thermocouple at 30.0 m from tunnel center; (c) Temperature distribution along the entire tunnel.	97
6.11	(a-c) Temperature distribution inside multiple roof vented tunnel with two heat sources; (d) Comparison of mass flow rate through three roof openings.	98
7.1	Schematic diagram of dual enclosure connected by a horizontal vent (All dimensions in m).	101
7.2	(a-c) Isosurface of thermal plume; (d-f) Evolution of temperature contours.	103
7.3	(a-d) Comparison of temperature contours for different ventilation velocities.	104

7.4	(a) Mass flow rate through horizontal opening; (b) Mass flow rate through top enclosure door-way.	106
7.5	(a-d) Comparison of temperature contours for different ventilation velocity; (e) Normal velocity contours; (f) Isosurface of thermal plume.	107
7.6	(a) Mass flow rate through horizontal opening; (b) Mass flow rate through bottom door way.	108
7.7	Comparison of results for two different heat source locations: (a,d) Isosurface of thermal plume; (b,e) Temperature contours; (c,f) Normal velocity contours.	109
7.8	(a) Horizontal vent center point temperature variation; (b) Horizontal vent center point normal velocity variation; (c) Lower enclosure door way center point temperature variation.	111
8.1	Schematic diagram of dual enclosure connected by a horizontal vent (All dimensions in m).	114
8.2	(a-f) Evolution of temperature contours.	116
8.3	(a) Isosurface of thermal plume; (b) Variation of net mass flow rate. .	117
8.4	(a-d) Comparison of temperature contours for different sprinkler discharge rates; (e) Isosurface of thermal plume.	118
8.5	Temperature distribution inside (a) lower compartment; (b) Upper compartment; (c) tall shaft.	119
8.6	Horizontal vent center point temperature variations.	120
8.7	(a) Mass flow rate through horizontal opening; (b) Mass flow rate through shaft doorway1.	121
8.8	(a-f) Comparison of temperature contours for different inlet velocities.	122
8.9	Temperature distribution inside (a) lower compartment; (b) tall shaft.	123

List of Tables

2.1	Average Nusselt number variation for different grids	19
2.2	Average Nusselt number variation over the heat source for different Grashof numbers	28
4.1	Average Nusselt number on the heated wall	57
6.1	Grid Independence with three mesh sizes.	87
6.2	Smoke layering length for heat release rate of 80 kW.	89
6.3	Smoke traveling time and maximum longitudinal velocity near the tunnel left and right openings	99
6.4	Smoke layering length.	99
7.1	Average mass flow rate and plume temperature for forced inlet velocities through lower enclosure doorway	105
7.2	Average mass flow rate and plume temperature for forced inlet velocities through upper enclosure doorway	108
7.3	Average mass flow rate and plume temperature for fire source located at 1.0m inside upper enclosure with forced flow through upper enclosure doorway	110
7.4	Average mass flow rate and plume temperature for fire source located at 3.0m inside upper enclosure with forced flow through upper enclosure doorway	110
8.1	Sprinkler operating conditions	115
8.2	Average fire plume temperature for different water discharge rates . .	121
8.3	Average fire plume temperature for sprinkler flow rate 60 l/min with different inlet velocities	124

Contents

Declaration	ii
Approval Sheet	iii
Acknowledgements	iv
Synopsis	vi
Referred publications	ix
Nomenclature	x
List of figures	xi
List of Tables	xvi
1 Introduction	1
1.1 Background	1
1.2 Buoyancy driven air flow in vented enclosure	2
1.2.1 Vertical openings	2
1.2.2 Horizontal openings	3
1.3 Vertical Shaft	4
1.4 Wind driven flows in buildings	5
1.5 Tunnel ventilation systems	6
1.6 Turbulence modeling	7
1.7 Non-Boussinesq approach	8
1.8 Motivation and Objectives of Present Work	9
1.9 Thesis Outline	10
2 Plume behavior in enclosure with horizontal vent	11
2.1 Problem definition	11
2.2 Mathematical Formulation	12
2.3 Boundary conditions	17
2.4 Numerical methods	18

2.5	Grid independence	19
2.6	Validation	20
2.7	Results and Discussion	21
2.7.1	Evolution of flow characteristics	22
2.7.2	Effect of Grashof number	25
2.7.3	Effect of heat source location	29
2.7.4	Effect of vent location	31
2.7.5	Effect of two vents	31
2.7.6	Effect of vent thickness	33
2.7.7	Entrainment effects through horizontal and vertical vents	34
2.8	Summary	37
3	Buoyant flows in vertical shaft	38
3.1	Problem definition	39
3.2	Grid Independence	39
3.3	Validation	39
3.4	Results and Discussion	42
3.4.1	Evolution of flow characteristics	42
3.4.2	Effect of Grashof number	44
3.4.3	Effect of vertical passage	45
3.4.4	Effect of ceiling vent in rectangular compartment	47
3.4.5	Effect of rectangular compartment location	49
3.5	Summary	49
4	Non-Boussinesq transition flows	51
4.1	Buoyant exchange flows between enclosures	51
4.1.1	Problem definition	51
4.1.2	Governing equations	52
4.1.3	Boundary conditions	55
4.1.4	Numerical Procedure	55
4.1.5	Grid Independence	56
4.1.6	Validation	57
4.1.7	Results and discussions	57
4.1.7.1	Evolution of flow characteristics for $Gr = 10^7$	58
4.1.7.2	Effect of Grashof number	63
4.1.7.3	Effect of vent width	66
4.1.7.4	Effect of vent thickness	68
4.2	Summary	70

5	Non-Boussinesq turbulent buoyant flows	71
5.1	Problem definition	71
5.2	Governing equations	72
5.3	Boundary conditions	73
5.4	Results and Discussion	74
5.4.1	Effect of inlet velocity	75
5.4.2	Effect of Grashof number	77
5.4.3	Effects of inlet port opening height (H_v)	78
5.4.4	Effects of inlet port location (V_L)	80
5.5	Summary	82
6	Tunnel ventilation	84
6.1	Problem definition	84
6.2	Governing equations	84
6.3	Grid Sensitivity	87
6.4	Validation	88
6.4.1	Results and discussion	89
6.4.1.1	Comparison of results with and without roof vent	89
6.4.1.2	Effect of heat source location	92
6.4.1.3	Effect of multiple roof openings	94
6.4.1.4	Effect of roof vent size	96
6.4.1.5	Effect of dual heat sources	96
6.4.1.6	Quantification of smoke traveling time and maximum longitudinal velocity	98
6.4.2	Summary	100
7	Wind effects on thermal plume behavior	101
7.1	Problem definition	102
7.2	Results and discussions	102
7.2.1	Effects of doorway flow with heat source placed in lower enclosure	102
7.2.2	Effects of forced air flow through lower enclosure doorway	104
7.2.3	Effects of forced air flow through upper enclosure doorway	105
7.2.4	Forced air flow through upper enclosure doorway with heat source placed in upper enclosure	108
7.2.5	Summary	111

8	Water spray interaction with thermal plume	113
8.1	Problem definition	113
8.2	Results and discussions	114
8.2.1	Fire transport phenomena without activating water spray system	115
8.2.2	Effects of water sprays on fire transport phenomena	115
8.2.3	Effect of forced air flow on thermal buoyancy and sprinkler drag force	123
8.3	Summary	124
9	Conclusions	126
	References	127

Chapter 1

Introduction

1.1 Background

The buoyancy driven flows through enclosure openings have extensive environmental and industrial applications. The thermal plume arising from the effects of buoyancy and discharge rate through openings are of great importance in cooling of electronic devices, solar collectors, building natural ventilation and enclosure fire dynamics. In buildings, openings such as doors and windows supplies fresh air, removes contaminated air, maintains indoor air quality and provides thermal comfort for occupants. Similarly, in tall atrium, stack effect is a major driving force for air exchanges between building interior and ambient. In the event of a fire accident in high rise multistoried buildings, significant number of occupants could be exposed to smoke, toxic gases and flame from the fire which could lead to catastrophic damage endangering human life and property. During fire accidents the smoke and hot gases spread rapidly due to buoyancy effects caused by temperature differences arising from fires and due to entrainment across vents and openings. The field modeling by Computational Fluid Dynamics (CFD) plays an important role in measuring the location of maximum temperature, pressure, velocity and smoke concentration thereby aiding fire safety measures such as location of fire and smoke detectors, smoke vent, physical barriers and fire escape routes. In fire ventilation, buoyancy and wind are two main driving forces by which smoke and hot gases are released and fresh air is brought into the interior space. The literature survey details are given below.

1.2 Buoyancy driven air flow in vented enclosure

In naturally ventilated enclosures with internal heat source, heat and mass exchange through openings are generated because of density difference caused by temperature difference.

1.2.1 Vertical openings

The flow patterns through large vertical openings such as doorways and windows were investigated extensively in literature. Brown and Solvason [1] studied natural convection flow through vertical rectangular opening in partition. They identified neutral pressure level close to middle of opening height, and found air flow profile develops stable velocity distribution across the opening. The hot air leaves through upper half of vertical passage, while, ambient air enters through lower half. Later, Allard and Utsumi [2] performed similar investigation and presented a general solution by which effects of density gradients and turbulence on gravitational flows were taken into account. They also found that large vertical opening can have more than one neutral pressure level. Prahl and Emmons [3] predicted the flow of fire gases through doorway of a burning room and proposed mathematical models to calculate exchange flow through vertical passages. Their model assumes the presence of two gas layers in enclosure; upper layer filled with hot gases and lower air layer made up of entrained ambient air. Rocket [4] utilized the two layer concept and his model regarded burning room as pump and window as throttle. Several theoretical models [5–9] were proposed to calculate infiltration rates through vertical passages.

Mercier and Jaluria [10] conducted experiments on fire induced flow of hot gas in enclosure with two vertical openings. They injected hot gases into the enclosure from lower opening and observed wall plume pattern inside the enclosure. Similar experiments [11, 12] were carried out to predict buoyancy induced ventilation rate in compartment with sidewall opening. Abib and Jaluria [13] did numerical simulation to evaluate the buoyant flow arising from heat source in vented compartment. They analyzed thermal plume behavior and calculated the bidirectional flow rates through opening by restricting the computational domain within the cavity. Chow and Zou [14] numerically studied airflow rates through doorway in fire scenarios and their proposed empirical correlations were in good agreement with experimental data. In literature, similar CFD simulations [15–18] were reported to predict the air movement through vertical openings.

1.2.2 Horizontal openings

The horizontal vents are openings in roofs, floors and the flow pattern is more complex and unstable across these openings. One of the earliest studies on natural convection flows through horizontal openings was carried out by Brown [19]. He considered air as the fluid medium and experiments were performed in a two compartmental enclosure connected by horizontal opening with square cross section. The two compartments were filled with hot and cold fluids; heavier fluid on top of lighter fluid and temperature difference between two compartments induces buoyancy driven exchange flows through horizontal passage. He derived correlations to calculate the mass exchange through horizontal square opening and identified that heat and mass transfer rises with increase in partition thickness. Later, Epstein [20] experimentally studied the bidirectional flows through horizontal circular opening with brine and fresh water as fluid medium. He varied the vent aspect ratio and proposed an empirical formula to calculate the mass flow rate. Tan and Jaluria [21–23] did experiments to study the mass flow rate through horizontal vent in an enclosure driven by pressure and density differences. They found that in the absence of pressure difference with heavier fluid lying on top of lighter fluid, bidirectional flow arises across the vent due to buoyancy effects [23]. They identified the critical pressure at which transition from bidirectional to unidirectional flow occurs across the vent. Similarly, different experimental studies [24–28] were carried out to investigate counter current exchange flow through horizontal opening.

The fire induced buoyant gas flow characteristics through horizontal vent were numerically analyzed [29, 30] and oscillatory flow behavior were observed across the opening. Mishra *et al.* [31] and Sleiti [32, 33] did numerical simulations to understand the buoyancy induced mixing through horizontal passage between two enclosures filled with heavier and lighter fluid. Sleiti [32] classified transport phenomena between enclosures based on four modes; diagonal exchange counter modes, counter flow exchange mode, standing wave mode and trapped-vortex mode. Recently, Venkatasubbaiah and Jaluria [34] analyzed the fire driven flow in square enclosure with single and multiple ceiling vents. They varied vent size and identified the critical Grashof number as 10^6 , above this flow becomes chaotic inside the enclosure. Chow and Gao [35, 36] investigated air flow patterns across horizontal vent and they identified that the ratio of buoyancy and inertia force is one of the key parameter affecting the bidirectional discharge across the opening.

All the above studies concluded that flow patterns through horizontal vent is

more complex and flow resistance is greater than in vertical opening. The transient behavior across the opening is due to the presence of denser fluid on top of lighter fluid. This particular flow behavior develops hydrodynamic instability such as Rayleigh Taylor instability across horizontal opening and needs further understanding. The bidirectional exchange rate depends on compartment geometry, heat source strength, heat source and vent location. However, most of the previous studies were carried out with fixed opening size and thickness.

1.3 Vertical Shaft

Modern high rise buildings consist of tall atria and elevator shafts where stack effect regulates the air movement inside building. Holford and Hunt [37] developed theoretical model to predict the thermal stratification in enclosure connected to an atrium. The theoretical model was compared with small scale salt bath experiments and the model was useful in calculating ventilation flow rates in naturally ventilated atrium. Ji and Cook [38] used CFD model to analyze the flow characteristics in multi-storey space connected to an atrium with internal heat source. The predicted temperature distribution, ventilation flow rates agreed well with analytical models and experiments. In case of fire accidents in tall building, stack effect needs to be controlled to prevent the rapid spread of smoke and hot gases to higher levels through vertical elevator shafts. Marshall [39, 40] experimentally studied the transport phenomena of hot gases in open shaft and stairwell, and developed mathematical model to calculate air entrainment. Zhang *et al.* [41] did numerical simulations to investigate the hot gas flow characteristics in tall shaft and found stack effect and turbulent mixing are the key driving forces for smoke movement. Similar investigations [42, 43] were reported to predict internal fire whirl due to smoke flow in vertical shaft, and it was observed that shaft side wall boundaries restricts plume horizontal momentum and generates swirling motion. A tall building consists of elevator shafts with multiple doorways connected to all floors. In summary, the earlier works were reported with single doorway opening in shaft. The smoke movement and entrainment effect in ceiling vented enclosure connected to shaft with multiple doorways has not been reported earlier.

1.4 Wind driven flows in buildings

The air flow patterns in naturally ventilated buildings are driven by combined forces of buoyancy and ambient wind. Hunt and Linden [44] analyzed the flow characteristics in ventilated compartment filled with buoyant fluid under the influence of external wind. He found buoyancy force plays a major role in forming thermal stratification inside the enclosure, and proposed analytical correlation that relates buoyancy force and wind. However during fire accidents, the wind effects on fire transport phenomena is unpredictable. The ambient wind flow through openings such as doors and windows; assists the fire spread by supplying additional oxygen meanwhile, cooler air reduces the intensity of heat from the fire and dilutes the concentration of toxic gases present in smoke.

Wind effects on smoke movement in buildings and its impact on the performance of building smoke control system were investigated by Poreh and Trebukov [45]. They identified the threshold wind speed, where the wind velocity dominates the buoyancy effects and smoke is primarily driven by wind generated pressure. The wind induced natural ventilation through refuge floor [46–48] located in tall buildings were analyzed using computational fluid dynamic model to predict the movement of smoke during fire accidents. They found that the wind speed, incidence angle and the number of enclosing external walls in the refuge area are the significant factors that affect the flow patterns and insufficient ventilation increases the risk of smoke logging.

The assisting or opposing behavior of wind on the thermal buoyancy force was studied analytically by Li and Delsante [49]. They calculated the natural ventilation flow rates through openings in building. Later, Chen *et al.*, [50] carried out investigations in high-rise buildings where the compartment fire behavior was affected by an opposing wind force. A similar investigation was performed by Andersen [51] to determine the opposing wind force on air flow rates in a room with two openings, and they identified that flow phenomena had multiple solutions due to instability and hysteresis effects. Similarly various effects of external ambient wind affecting the internal flow dynamics inside buildings were reported in other literature [52, 53].

Reduced scale experiments were carried by Lassus *et al.*, [54] inside a compartment, and he observed that fire growth and heat release rates were

significantly affected by ventilation conditions. Experimental studies were performed by Huang *et al.*, [55] in a reduced scale compartment with different wind velocities and fire source location. For higher wind velocities, the thermal plume becomes wider and is inclined towards downwind side, and thereby fire spreads to neighboring buildings. Although several investigations were reported considering the combined effects of buoyancy and wind, most of the previous research work focused on flow characteristics in a single cubical enclosure with vertical openings. The flow characteristics through horizontal vent under the influence of forced ventilated doorway are not reported in literature.

1.5 Tunnel ventilation systems

The tunnel fire is the major hazard which endangers human life, environment and property. In the event of fire accidents, fire spreads quickly and passengers are exposed to smoke and toxic gases. Limitations in the number of fire escape routes and difficulty for emergency services to access fire accident location increases the risks and vulnerability of accidents. To ensure safety measures in tunnel, ventilation systems are designed for supplying clean ambient air and to reduce the soot and toxic gases which endanger human life during emergency conditions. Tunnel ventilation systems are generally classified into mechanical and natural ventilation systems. Most of the tunnels are equipped with longitudinal mechanical ventilation systems that require installation of fans to induce airflows and ducts to distribute the airflow. Oka and Atkinson [56] experimentally studied the effect of forced longitudinal velocity in controlling tunnel upstream smoke movement by varying the size and location of fire source. Based on their experimental findings empirical correlations were established to relate the influence of critical velocity on heat release rates. Lee and Ryou [57] performed numerical simulations to predict the smoke movement and temperature distribution in ventilated tunnel by varying tunnel aspect ratio. Experimental investigations [58] were carried out in ventilated tunnel with fire source to study the effect of tunnel slope. The angle of tunnel slope was varied and inclination effects were analyzed with different fire size and ventilation velocities. Small scale [59] experimental and numerical simulations were performed in tunnel with two fire sources under forced ventilation conditions. All the above studies focused on critical ventilation velocities in tunnel to prevent back layering of smoke under forced ventilation conditions.

Full-scale experiments were conducted by Wang *et al.*, [60, 61] to study the smoke removal efficiency in naturally ventilated tunnel with roof openings. Their study highlighted that most smoke flow out of the tunnel through roof openings. Recent studies [62–64] in naturally ventilated tunnels with vertical ventilation shafts concluded that ventilation shafts are more efficient as chimneys for smoke exhaust and increases natural ventilation pressure. Recent study [65] on tunnel ventilation was based on mixed mode ventilation system. They studied the influence of forced longitudinal ventilation on natural roof ventilation system. They identified the critical longitudinal velocity suitable for better smoke removal. Similar investigations [66, 67] were carried out to determine the effects of longitudinal ventilations on the ceiling mounted smoke extraction systems.

Forced longitudinal ventilations are ideal for tunnels with unidirectional traffic flow. For tunnels with bidirectional travel, buoyancy induced ceiling ventilation systems are more suitable. This does not require installation of mechanical fans, ducts and reduces the installation and operating cost. The studies on the effects of heat source locations in roof vented tunnel with multiple vents are limited.

1.6 Turbulence modeling

The plume transport phenomena involves complex processes and buoyancy induced turbulent mixing is important since it is one of the key process for the growth and spread of thermal plume. Turbulent natural convection flow was studied by Markatos and Pericleous [68] in a square cavity with differentially heated side walls using standard $k - \varepsilon$ turbulence model. They found that the model is suitable for predicting natural convection flows. Cook and Lomas [69] analyzed buoyancy driven flows in enclosure using standard $k - \varepsilon$ and RNG $k - \varepsilon$ models. They found RNG $k - \varepsilon$ model gave better results. Stavrakakis and Markatos [70] numerically studied the air flow in one and two room enclosures containing a fire source. The standard $k - \varepsilon$ and RNG $k - \varepsilon$ models were used to simulate the buoyancy induced flows. The capability of the two turbulence models were compared with the experimental results and it was concluded that both turbulence model can be used for fire simulations. Extensive numerical investigations were performed by Kenjeres *et al.* [71–74] on turbulent natural and mixed convection problems using transient Reynolds averaged Navier-Stokes (TRANS) with different turbulence model and their results showed good agreement with LES, DNS and experimental results.

Turbulent natural convection flow in differentially heated cavity with radiation effects were studied using $k - \varepsilon$ turbulence model, [75, 76] and the simulation results were in good agreement with experimental data. Similarly, Kuznetsov and Sheremet [77] analyzed buoyancy driven flows in square cavity with finite wall thickness using $k - \varepsilon$ model, and found that the model was able to capture the turbulent flow characteristic accurately.

Abib and Jaluria [78] numerically analyzed the turbulent penetrative and recirculating flow in vented compartment fire with low Reynolds number model of Lam Bremhorst. Similarly Davidson [79] and Akhilesh *et al.* [80] carried out numerical analysis on buoyancy induced turbulent flows using Lam Bremhorst model and found that this model has higher capability of predicting turbulent quantities reasonably well in regions near and away from the walls. The capability of Large Eddy simulations (LES) model in predicting the air flow characteristics in buildings were numerically analyzed [81–83] and their investigation revealed that the numerical results were close to experimental predictions. The capability and accuracy of different turbulence models for the buoyancy induced turbulent flows were reported [84–86]. Several approaches have been proposed with better and optimized turbulence models [87–89]; however, there is no universal turbulence model that is suitable for all applications of computational fluid dynamics.

1.7 Non-Boussinesq approach

Most of the classical problems on buoyancy induced flow phenomena were modeled with Boussinesq approximation. The approximation is valid when product of thermal expansion coefficient and temperature difference is insignificant. However, for applications with larger temperature difference such as fire ventilation it is inappropriate to evaluate density variations by Boussinesq approximation. Vierendeels *et al.*, [90] numerically studied thermally driven flows in square cavity in non-Boussinesq regime by solving compressible Navier-Stokes equation. The convective term was evaluated by explicit third order discretization scheme and stiffness was treated by preconditioning technique. A similar numerical study was carried out by compressible approach using finite volume method [91] to incorporate larger density variations. In variable density formulations, Gay-Lussac number (Ga) [92, 93] quantifies density variations of working fluid. The Boussinesq approximation is valid when Gay-Lussacs number is negligible, close to zero. The effects of Ga on

the flow characteristics were investigated [93] for fixed Rayleigh and Prandtl numbers. They identified that velocity fields were significantly affected by increasing Gay-Lussacs number. Kumar and Eswaran [94] studied natural convection flows in 3-D differentially heated cavity considering radiation effects using non-Boussinesq variable density approach. Recent numerical study on high thermobuoyant flows [95] in square cavity with bottom heat source has compared the heat transfer characteristics between incompressible Boussinesq and compressible flows. Similar numerical investigations were carried out to predict the conjugate natural convection flows in vertical annulus [96] and capability of Boussinesq and non-Boussinesq models were discussed. The above investigations on natural convection flows were discussed in closed cavities which are heated from the left and bottom boundaries. In literature, numerical works on buoyancy induced exchange flows in partial open enclosures modeled by non-Boussinesq approach are limited.

1.8 Motivation and Objectives of Present Work

The buoyancy induced turbulent flows in partial enclosures have extensive environmental and industrial applications. In literature studies on the thermal plume and flow characteristics in enclosures with vertical and horizontal openings are limited. The flow patterns through horizontal openings are complex and more unstable than vertical openings. Most of the previous investigations have focused on fixed vent aspect ratio. Previous studies have not considered the effects of compartment geometry, heat source strength, vent aspect ratio, wind direction, wind speed, vertical barriers, multiple vents, heat source and vent locations. This has been the motivation for present investigation.

The aim of present study is to investigate buoyancy induced turbulent flows through horizontal vents in enclosures with different configurations. The aim is achieved through following objectives.

- To develop RANS based buoyancy induced turbulent flow solver with high accuracy compact finite difference schemes within the frame work of Boussinesq approximation.
- To study the thermal plume behavior in ceiling vented square and rectangular enclosures.

- To study the effect of vertical and horizontal openings in rectangular compartment connected to vertical shaft.
- To perform parametric analysis by varying Grashof number, vent size, heat source and vent locations.
- To develop non-Boussinesq variable density solver to study the buoyancy-induced laminar and turbulent flows.
- To study buoyant flows in tunnels with multiple ceiling vents using FDS code based on LES.
- To investigate the wind effects and drag force of water particles on plume behavior in dual enclosures.

1.9 Thesis Outline

The thesis is organized in the following way.

- Chapter 2 describes the modeling of turbulent buoyant flows and results are presented for the case of ceiling vented square enclosure with internal heat source.
- Chapter 3 presents the results of buoyancy induced flows in rectangular compartment connected to vertical shaft.
- Chapter 4 provides the modeling of non-Boussinesq transition flows and includes the results of buoyancy driven mixing between two enclosures filled with hot and cold fluid.
- Chapter 5 presents the formulation of non-Boussinesq turbulent flows and results are presented for ceiling vented square enclosure with forced inlet port.
- Chapter 6 provides the Large Eddy Simulation results of buoyant flows in tunnel with roof openings.
- Chapter 7 describes the influence of wind speed and wind direction on plume behavior in dual enclosures.
- Chapter 8 presents the interactions between water sprays and thermal plume in dual enclosure connected to vertical shaft.
- Chapter 9 summarizes the conclusions and opportunities for future research.

Chapter 2

Plume behavior in enclosure with horizontal vent

The thermal plume behavior in ceiling vented enclosure with internal heat source is numerically investigated in this chapter. The horizontal or ceiling vents are openings in ceilings, floors or smoke vent at roof top. The bidirectional discharge rate through horizontal openings are highly unstable in comparison with vertical openings such as doorways and windows.

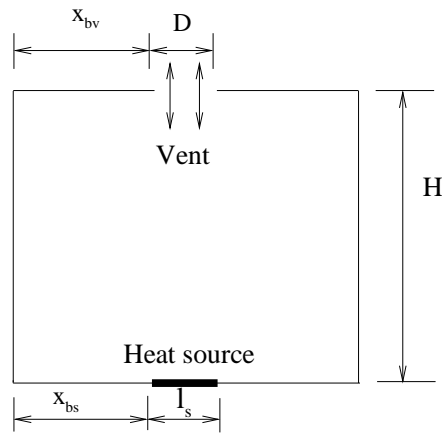


Figure 2.1: Schematic diagram of square enclosure with ceiling vent.

2.1 Problem definition

The schematic diagram of square enclosure with ceiling vent is shown in Fig. 2.1. There is a finite-size heat source at constant temperature T_s located at the bottom wall of enclosure and ceiling vent of width D above to the ambient media at temperature T_∞ .

2.2 Mathematical Formulation

In buoyant flows, turbulence is generated from hot gases rising into the ambient fluid and hence, it is necessary to understand the fundamentals of turbulence. The three primary turbulence modeling approaches in CFD are Direct Numerical Simulation (DNS), Large Eddy Simulation (LES) and Reynolds-Averaged Navier-Stokes (RANS). DNS and LES are computationally expensive for practical engineering applications. As a result, majority of turbulent flows are simulated with RANS approach. The RANS equations are obtained from Navier-Stokes equations as follows:

Continuity equation

$$\frac{\partial u_i}{\partial x_i} = 0 \quad (2.1)$$

Momentum equation

$$\frac{\partial u_i}{\partial t} + u_j \frac{\partial u_i}{\partial x_j} = -\frac{1}{\rho} \frac{\partial p}{\partial x_i} + \frac{\partial}{\partial x_j} \left(\nu \frac{\partial u_i}{\partial x_j} \right) \quad (2.2)$$

Energy equation

$$\frac{\partial T}{\partial t} + u_i \frac{\partial T}{\partial x_i} = \frac{\partial}{\partial x_i} \left(\alpha_e \frac{\partial T}{\partial x_i} \right) \quad (2.3)$$

The RANS equations are obtained by time averaging of Navier-Stokes equations by replacing flow variables by sum of their mean and fluctuating parts.

$$\begin{aligned} u_i &= \bar{u}_i + u_i' \\ T &= \bar{T} + T' \end{aligned} \quad (2.4)$$

The averaging of Navier-Stokes equation introduces unknown Reynolds stress tensor (τ_{ij}) that needs to be modeled. As a result, RANS equations are not closed since number of unknowns are greater than number of equations. Most of the approaches employ Boussinesq eddy-viscosity concept to model Reynolds stress tensor. The eddy-viscosity concept assumes that Reynolds stress is directly proportional to mean rate of strain and is given below.

$$-\overline{u_i' u_j'} = \nu_t \left(\frac{\partial \bar{u}_i}{\partial x_j} + \frac{\partial \bar{u}_j}{\partial x_i} \right) - \frac{2}{3} k \delta_{ij} \quad (2.5)$$

The symbol ν_t represents turbulent eddy viscosity which is not a fluid property but depends strongly on the state of turbulence. δ_{ij} represents kronecker delta, k is the kinetic energy of fluctuating motions.

$$k = \frac{1}{2} \left(\overline{u'^2} + \overline{v'^2} + \overline{w'^2} \right) \quad (2.6)$$

Similarly, time averaging of energy equation introduces turbulent heat flux which needs to be modeled.

$$-\overline{u'_i T'} = \frac{\nu_t}{\sigma_t} \left(\frac{\partial \overline{T}_i}{\partial x_i} \right) \quad (2.7)$$

where σ_t represents turbulent Prandtl number.

The turbulent eddy viscosity is determined by different turbulent models and are generally classified as follows:

- Algebraic or Zero-Equation Models
- One-Equation Models
- Two-Equation Models

In algebraic model, turbulent eddy viscosity is determined in terms of local mean velocity and an example of this approach is the mixing layer model that relates mixing length scale to turbulent viscosity.

$$\nu_t = l^2 \left| \frac{\partial u_i}{\partial y_j} \right| \quad (2.8)$$

The one-equation model solves the turbulent kinetic energy equation. The turbulent length scale is then algebraically prescribed in this model. The turbulent viscosity is related to kinetic energy and length scale using the below relation.

$$\nu_t = \sqrt{k} l \quad (2.9)$$

The two-equation model is commonly used for modeling turbulence in RANS based calculations. In this model, two transport equations are solved for turbulent kinetic energy (k) and turbulent dissipation rate (ϵ). Some of the commonly used two-equation models are Standard $k - \epsilon$ model, $k - \omega$ model, Realizable $k - \epsilon$ model and Re-Normalized Group method (RNG) model. The Lam Bremhorst low Reynolds number $k - \epsilon$ model is one of the most widely two-equation model for buoyant flows with entrainment. This model uses damping wall functions in transport equations which allow smooth change of flow variables from laminar sublayer near the wall to fully developed turbulent flows away from the wall.

The present study is modeled as two-dimensional, unsteady incompressible turbulent buoyant flow in a long partial square enclosure. The governing equations for turbulent natural convection flows is described mathematically by the Reynolds averaged Navier-Stokes equations (RANS), including the time averaged energy equation for the mean temperature field that drives the flow by buoyancy force. The buoyancy term is modeled by Boussinesq approximation that treats density as a constant value in all equations, except for the buoyancy term in the momentum equation. Turbulence is modeled with a low Reynolds number $k - \epsilon$ model of Lam Bremhorst including the contribution of buoyancy force in the turbulent kinetic energy generation and dissipation. The governing equations are as follows.

Continuity equation

$$\frac{\partial u}{\partial x} + \frac{\partial v}{\partial y} = 0 \quad (2.10)$$

x-momentum equation

$$\begin{aligned} \frac{\partial u}{\partial t} + u \frac{\partial u}{\partial x} + v \frac{\partial u}{\partial y} = -\frac{1}{\rho} \frac{\partial p}{\partial x} + \nu \left[\frac{\partial^2 u}{\partial x^2} + \frac{\partial^2 u}{\partial y^2} \right] + 2 \frac{\partial}{\partial x} \left[\nu_t \frac{\partial u}{\partial x} \right] \\ + \frac{\partial}{\partial y} \left[\nu_t \frac{\partial u}{\partial y} \right] + \frac{\partial}{\partial y} \left[\nu_t \frac{\partial v}{\partial x} \right] \end{aligned} \quad (2.11)$$

y-momentum equation

$$\begin{aligned} \frac{\partial v}{\partial t} + u \frac{\partial v}{\partial x} + v \frac{\partial v}{\partial y} = -\frac{1}{\rho} \frac{\partial p}{\partial y} + \nu \left[\frac{\partial^2 v}{\partial x^2} + \frac{\partial^2 v}{\partial y^2} \right] + \frac{\partial}{\partial x} \left[\nu_t \frac{\partial u}{\partial y} \right] \\ + \frac{\partial}{\partial x} \left[\nu_t \frac{\partial v}{\partial x} \right] + 2 \frac{\partial}{\partial y} \left[\nu_t \frac{\partial v}{\partial y} \right] + g\beta(T - T_\infty) \end{aligned} \quad (2.12)$$

Where g is the acceleration due to gravity; β is the coefficient of volumetric thermal expansion; ρ is the density of the fluid; α_e is the thermal diffusivity. The turbulent

eddy viscosity (ν_t) is evaluated from the relation $\nu_t = \frac{C_\mu k^2}{\epsilon}$. C_μ is a model constant and its value is 0.09.

Energy equation

$$\frac{\partial T}{\partial t} + u \frac{\partial T}{\partial x} + v \frac{\partial T}{\partial y} = \frac{\partial}{\partial x} \left[\left(\alpha + \frac{\nu_t}{\sigma_t} \right) \frac{\partial T}{\partial x} \right] + \frac{\partial}{\partial y} \left[\left(\alpha_e + \frac{\nu_t}{\sigma_t} \right) \frac{\partial T}{\partial y} \right] \quad (2.13)$$

The value of σ_t is taken as 0.9.

Kinetic energy equation

$$\frac{\partial k}{\partial t} + u \frac{\partial k}{\partial x} + v \frac{\partial k}{\partial y} = \frac{\partial}{\partial x} \left[\left(\nu + \frac{\nu_t}{\sigma_k} \right) \frac{\partial k}{\partial x} \right] + \frac{\partial}{\partial y} \left[\left(\nu + \frac{\nu_t}{\sigma_k} \right) \frac{\partial k}{\partial y} \right] + G_k - \epsilon + P_k \quad (2.14)$$

The term P_k is the production of turbulent kinetic energy due to shear and is given below

$$P_k = \nu_t \left[2 \left(\frac{\partial u}{\partial x} \right)^2 + 2 \left(\frac{\partial v}{\partial y} \right)^2 + \left(\frac{\partial u}{\partial y} + \frac{\partial v}{\partial x} \right)^2 \right] \quad (2.15)$$

The term G_k is the production of turbulence due to buoyancy effects and are as follows

$$G_k = - \frac{g\beta\nu_t}{Pr_t} \frac{\partial T}{\partial y} \quad (2.16)$$

Dissipation equation

$$\begin{aligned} \frac{\partial \epsilon}{\partial t} + u \frac{\partial \epsilon}{\partial x} + v \frac{\partial \epsilon}{\partial y} = & \frac{\partial}{\partial x} \left[\left(\nu + \frac{\nu_t}{\sigma_\epsilon} \right) \frac{\partial \epsilon}{\partial x} \right] + \frac{\partial}{\partial y} \left[\left(\nu + \frac{\nu_t}{\sigma_\epsilon} \right) \frac{\partial \epsilon}{\partial y} \right] - C_{2\epsilon} f_2 \frac{\epsilon^2}{k} \\ & + C_{1\epsilon} f_1 \left[\nu_t \left\{ 2 \left(\frac{\partial u}{\partial x} \right)^2 + 2 \left(\frac{\partial v}{\partial y} \right)^2 + \left(\frac{\partial u}{\partial y} + \frac{\partial v}{\partial x} \right)^2 \right\} - C_{3\epsilon} \left\{ \frac{g\beta\nu_t}{Pr_t} \frac{\partial T}{\partial y} \right\} \right] \frac{\epsilon}{k} \end{aligned} \quad (2.17)$$

The RANS equations are obtained in the stream function (ψ) and vorticity (ω) formulation approach. Advantages of this formulation are added accuracy due to exact satisfaction of mass conservation and reduction in the number of unknowns to two as compared to three unknowns for primitive variable formulations. Pressure is eliminated by taking the curl of the momentum equation to give the vorticity transport equation (VTE). The turbulent kinetic energy (k) and dissipation (ϵ) equations are obtained using the low Reynolds number $k - \epsilon$ turbulence model of Lam Bremhorst. The following non-dimensional variables are used to obtain the dimensionless governing equations. The free convection velocity ($V_c = \sqrt{g\beta\Delta TH}$) is considered as the reference velocity scale. The height (H) of the enclosure is considered as the reference length scale.

$$X = \frac{x}{H}; Y = \frac{y}{H}; U = \frac{u}{V_c}; V = \frac{v}{V_c}; \tau = \frac{tV_c}{H}; \theta = \frac{T-T_\infty}{T_s-T_\infty}; V_c = (g\beta\Delta TH)^{\frac{1}{2}};$$

$$\Omega = \omega \frac{(H)^{\frac{1}{2}}}{(g\beta\Delta T)^{\frac{1}{2}}}; \Psi = \frac{\psi}{(g\beta\Delta TH^3)^{\frac{1}{2}}}; K = \frac{k}{(g\beta\Delta TH)}; \varepsilon = \frac{\epsilon}{((g\beta\Delta T)^3 H)^{\frac{1}{2}}}$$

The dimensionless governing equations are as follows.

Non-dimensional Stream function equation

$$\frac{\partial^2 \Psi}{\partial X^2} + \frac{\partial^2 \Psi}{\partial Y^2} = -\Omega \quad (2.18)$$

Non-dimensional Vorticity transport equation

$$\begin{aligned} \frac{\partial \Omega}{\partial \tau} + U \frac{\partial \Omega}{\partial X} + V \frac{\partial \Omega}{\partial Y} = & \frac{\partial}{\partial X} \left[\left(\frac{1}{(Gr)^{\frac{1}{2}}} + \frac{1}{Re_t} \right) \frac{\partial \Omega}{\partial X} \right] + \frac{\partial \theta}{\partial X} + \frac{\partial}{\partial Y} \left[\left(\frac{1}{(Gr)^{\frac{1}{2}}} + \frac{1}{Re_t} \right) \frac{\partial \Omega}{\partial Y} \right] \\ & + 2 \frac{\partial U}{\partial Y} \frac{\partial^2}{\partial X^2} \left[\frac{1}{Re_t} \right] - 2 \frac{\partial V}{\partial X} \frac{\partial^2}{\partial Y^2} \left[\frac{1}{Re_t} \right] + 2 \left[\frac{\partial V}{\partial Y} - \frac{\partial U}{\partial X} \right] \frac{\partial^2}{\partial X \partial Y} \left[\frac{1}{Re_t} \right] \end{aligned} \quad (2.19)$$

Non-dimensional Energy equation

$$\frac{\partial \theta}{\partial \tau} + U \frac{\partial \theta}{\partial X} + V \frac{\partial \theta}{\partial Y} = \frac{\partial}{\partial X} \left[\left(\frac{1}{(Pr(Gr)^{\frac{1}{2}}} + \frac{1}{Pr_t Re_t} \right) \frac{\partial \theta}{\partial X} \right] + \frac{\partial}{\partial Y} \left[\left(\frac{1}{(Pr(Gr)^{\frac{1}{2}}} + \frac{1}{Pr_t Re_t} \right) \frac{\partial \theta}{\partial Y} \right] \quad (2.20)$$

Non-dimensional Kinetic energy equation

$$\begin{aligned} \frac{\partial K}{\partial \tau} + U \frac{\partial K}{\partial X} + V \frac{\partial K}{\partial Y} = & \frac{\partial}{\partial X} \left[\left(\frac{1}{(Gr)^{\frac{1}{2}}} + \frac{1}{\sigma_k Re_t} \right) \frac{\partial K}{\partial X} \right] + \frac{\partial}{\partial Y} \left[\left(\frac{1}{(Gr)^{\frac{1}{2}}} + \frac{1}{\sigma_k Re_t} \right) \frac{\partial K}{\partial Y} \right] \\ & - \frac{1}{Re_t Pr_t} \frac{\partial \theta}{\partial Y} - \varepsilon + \frac{1}{Re_t} \left[2 \left(\frac{\partial U}{\partial X} \right)^2 + 2 \left(\frac{\partial V}{\partial Y} \right)^2 + \left(\frac{\partial U}{\partial Y} + \frac{\partial V}{\partial X} \right)^2 \right] \end{aligned} \quad (2.21)$$

Non-dimensional Dissipation equation

$$\begin{aligned} \frac{\partial \varepsilon}{\partial \tau} + U \frac{\partial \varepsilon}{\partial X} + V \frac{\partial \varepsilon}{\partial Y} = & \frac{\partial}{\partial X} \left[\left(\frac{1}{(Gr)^{\frac{1}{2}}} + \frac{1}{\sigma_\varepsilon Re_t} \right) \frac{\partial \varepsilon}{\partial X} \right] + \frac{\partial}{\partial Y} \left[\left(\frac{1}{(Gr)^{\frac{1}{2}}} + \frac{1}{\sigma_\varepsilon Re_t} \right) \frac{\partial \varepsilon}{\partial Y} \right] - C_{2\varepsilon} f_2 \frac{\varepsilon^2}{k} \\ & C_{1\varepsilon} f_1 \left[\frac{1}{Re_t} \left\{ 2 \left(\frac{\partial U}{\partial X} \right)^2 + 2 \left(\frac{\partial V}{\partial Y} \right)^2 + \left(\frac{\partial U}{\partial Y} + \frac{\partial V}{\partial X} \right)^2 \right\} - C_{3\varepsilon} \frac{1}{Re_t Pr_t} \frac{\partial \theta}{\partial Y} \right] \frac{\varepsilon}{K} \end{aligned} \quad (2.22)$$

For low Reynolds number $k - \epsilon$ turbulence model, constants used are $C_\mu = 0.09$; $C_{1\varepsilon} = 1.44$; $C_{2\varepsilon} = 1.92$; $C_{3\varepsilon} = 0.7$; $Pr_t = 0.9$; $\sigma_k = 1.0$; $\sigma_\varepsilon = 1.3$. The damping wall

functions f_1 , f_2 and f_μ are as follows.

$$f_1 = 1 + \left(\frac{0.14}{f_\mu}\right)^3 \quad (2.23)$$

$$f_2 = [1 - 0.27 \exp(-R_t^2)] [1 - \exp(-R_n)] \quad (2.24)$$

$$f_\mu = \exp \left[-\frac{3.4}{1 + \left(\frac{R_t}{50}\right)^2} \right] \quad (2.25)$$

Where $Gr = \frac{g\beta\Delta TH^3}{\nu^2}$ is the Grashof number; $Pr = \frac{\nu}{\alpha}$ is the Prandtl number; $Re_t = \frac{\varepsilon}{C_\mu K^2}$; $R_t = Gr^{1/2} \left(\frac{K^2}{\varepsilon}\right)$; $R_n = Gr^{1/2} K^{1/2} n$; n is the normal distance from the nearest wall. Rayleigh number is the product of Gr and Pr and is represented as follows

$$Ra = \frac{g\beta\Delta TH^3}{\nu\alpha}$$

The expressions for the velocity components in terms of stream function are as follows.

$$U = \frac{\partial\psi}{\partial Y}; \quad V = -\frac{\partial\psi}{\partial X} \quad (2.26)$$

2.3 Boundary conditions

It is easy to describe the boundary conditions at the solid walls. The problem is, however, the treatment of the boundaries that are not bounded by solid walls and that involve entrainment flows at the openings. Mass, momentum and energy exchange may take place at the opening as a result of viscous effects and turbulent mixing. The boundary condition at the opening is to account the interactions between cold and hot fluids due to temperature difference. Hence flow modeling in enclosure with ceiling vent is complex due to bidirectional flow at the vent. In the present study computational domain is restricted within the cavity. No-slip boundary condition is applied on the solid walls for the velocity field. At the bottom wall, the temperature of the source is specified and the remaining walls are taken as adiabatic. At the vent, horizontal velocity is set to zero and vertical velocity is obtained from mass balance $\frac{\partial v}{\partial y} = 0$. The temperature of the fluid leaving the vent satisfies the upwind condition $\frac{\partial T}{\partial y} = 0$. The turbulent kinetic energy and normal gradient of dissipation is set to zero at the walls. At the vent, the normal gradients of kinetic energy and dissipation are set to zero.

The appropriate initial and boundary conditions in dimensionless form are as follows:

$$\text{at } \tau = 0 : \quad \psi = \text{constant}; \quad \Omega = \theta = 0 \quad (2.27)$$

for $\tau > 0$:

$$\begin{aligned} X = 0; X = 1.0; 0 < Y < 1.0 : \psi = \text{constant}; \Omega = -\frac{\partial^2 \psi}{\partial X^2}; \frac{\partial \theta}{\partial X} = 0; \\ K = 0; \frac{\partial \varepsilon}{\partial X} = 0 \end{aligned} \quad (2.28)$$

$$\begin{aligned} Y = 0; 0 < X < 1.0 : \psi = \text{constant}; \Omega = -\frac{\partial^2 \psi}{\partial Y^2}; K = 0; \frac{\partial \varepsilon}{\partial Y} = 0 \\ Y = 0; 0 < X < X_{bs} : \frac{\partial \theta}{\partial Y} = 0 \\ X_{bs} < X < X_{bs} + l_s : \theta = 1.0 \\ X_{bs} + l_s < X < 1.0 : \frac{\partial \theta}{\partial Y} = 0 \end{aligned} \quad (2.29)$$

$$\begin{aligned} Y = 1.0; 0 < X < X_{bv} : \psi = \text{constant}; \Omega = -\frac{\partial^2 \psi}{\partial Y^2}; \frac{\partial \theta}{\partial Y} = 0 \\ K = 0; \frac{\partial \varepsilon}{\partial Y} = 0 \\ X_{bv} < X < X_{bv} + D : \frac{\partial \psi}{\partial Y} = \frac{\partial \Omega}{\partial Y} = \frac{\partial \theta}{\partial Y} = \frac{\partial K}{\partial Y} = \frac{\partial \varepsilon}{\partial Y} = 0 \\ X_{bv} + D < X < 1.0 : \psi = \text{constant}; \Omega = -\frac{\partial^2 \psi}{\partial Y^2}; \frac{\partial \theta}{\partial Y} = 0 \\ K = 0; \frac{\partial \varepsilon}{\partial Y} = 0 \end{aligned} \quad (2.30)$$

where X_{bs} is the distance upto the source; l_s is the source width; X_{bv} is the distance upto the vent; D is the vent width.

2.4 Numerical methods

The governing equations are discretized using finite difference schemes and the solver is developed in Fortran 90. The stream function equation (SFE) is discretized using a second order central difference scheme (CD_2). An iteration method of Bi-conjugate gradient is used to solve the stream function equation. The vorticity transport equation (VTE), energy equation (EE), Kinetic energy and dissipation equations are solved by discretizing the diffusion terms using CD_2 . The details are are given below.

The second-order derivatives in the governing equations are evaluated by using central finite difference scheme.

$$\left(\frac{\partial^2 \phi}{\partial x^2} \right) = \frac{\phi_{i+1,j} - 2\phi_{i,j} + \phi_{i-1,j}}{(\Delta x)^2} \quad (2.31)$$

In finite difference technique, compact schemes are used to evaluate the non-linear

convective terms to get solutions with better spacial accuracy. The Optimal Upwind Compact Schemes (OUCS-3) used in the present study has higher spectral accuracy and are computationally inexpensive when compared to spectral methods. In OUCS-3 scheme, derivatives at the internal grid points are expressed by an implicit equation. The details of OUCS-3 scheme are given below:

$$p_{j-1}u'_{j-1} + u'_j + p_{j+1}u'_{j+1} = \frac{1}{h} \sum_{k=-2}^2 q_k u_{j+k} \quad (2.32)$$

where $p_{j\pm 1} = D \pm \frac{\eta}{60}$; $q_{\pm 2} = \pm \frac{F}{4} + \frac{\eta}{300}$; $q_{\pm 1} = \pm \frac{E}{2} + \frac{\eta}{30}$; $q_0 = -\frac{11\eta}{150}$ with $D=0.3793894912$; $E=1.57557379$; $F=0.183205192$ and $\eta = -2$.

Further details about compact schemes are given in Sengupta et al. [97]. All simulations are performed with double precision to reduce the round-off error. The convergence criterion is chosen as $\leq 10^{-6}$ to solve the stream function equation. Time integration is performed by the four stage Runge-Kutta (RK4) scheme. A small time step of $\Delta\tau = 10^{-4}$ is chosen to avoid the numerical instability.

2.5 Grid independence

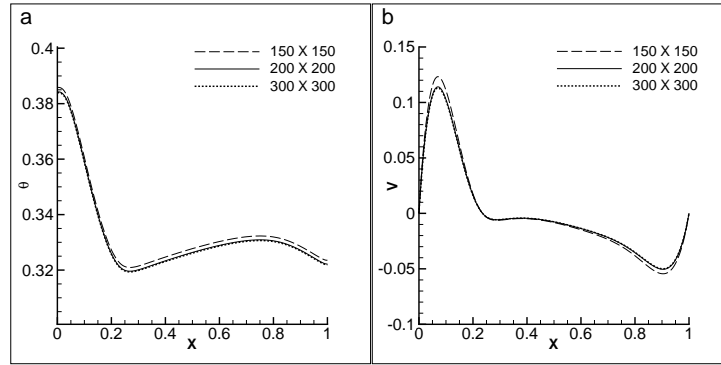


Figure 2.2: Temperature (a) and vertical velocity (b) profiles along the horizontal surface for different grid sizes.

Table 2.1: Average Nusselt number variation for different grids

Grid size	Average Nusselt number
150 × 150	87.621
200 × 200	87.238
300 × 300	87.235

Numerical simulations are obtained with uniform mesh of different grid sizes:

150 × 150, 200 × 200, 300 × 300 and shown in Fig. 2.2 for Grashof number $Gr = 10^{10}$ with a vent width $D = 0.2H$. In Fig. 2.2 (a & b), the temperature and vertical velocity distributions are plotted along the horizontal wall at the center of the enclosure and profiles are shown with different grid sizes. The heat transfer rate from the heat source to the surrounding fluid is calculated in the form of non-dimensional number called Nusselt number. The local dimensionless normal temperature gradient on the heated surface is numerically integrated by trapezoidal rule to obtain the average Nusselt number. The average Nusselt number variations with different grid sizes are presented in Table 2.1. It is observed that with a grid size of 200x200 and 300x300 there is no considerable change in the average Nusselt number value. Hence a grid size of 200x200 is used in the present study.

2.6 Validation

The mathematical model and numerical method are validated with previous results in literature. Dixit and Babu [98] numerically analyzed the buoyancy driven flow in a square cavity that has a differentially heated vertical walls and adiabatic upper and bottom walls by lattice Boltzmann method (LBM) for Rayleigh number $Ra = 10^7$. The stream function and temperature contours shown in Fig. 2.3 (a & b) are matching well with the numerical results of Dixit and Babu [98]. Fig. 2.3 (c) depicts the temperature profile along the horizontal wall at the center of the enclosure and shows quantitative comparison between the present results and LBM results. The slight variations visible between the two results are due to difference in numerical method (discretization schemes and solution technique).

Turbulent natural convection flow in a square cavity was studied experimentally by Tian and Karayiannis [99]. The top and bottom walls are made of mild steel sheet with wooden insulation and considered as adiabatic boundaries. The vertical walls are maintained at constant temperatures of $50^{\circ}C$ and $10^{\circ}C$ with a corresponding Rayleigh number of $Ra = 1.58 \times 10^9$. The temperature and velocity profiles along the horizontal wall at the center of the square enclosure are shown in Fig. 2.3 (d & e) for $Ra = 1.58 \times 10^9$. A quantitative comparison is shown between the results obtained using second order central difference scheme (CD_2) and compact scheme (OUCS-3). Experimental data's are shown in discrete symbols and present results are shown in solid lines. The temperature and velocity profiles agreed well with the experimental results of Tian and Karayiannis [99] and the present

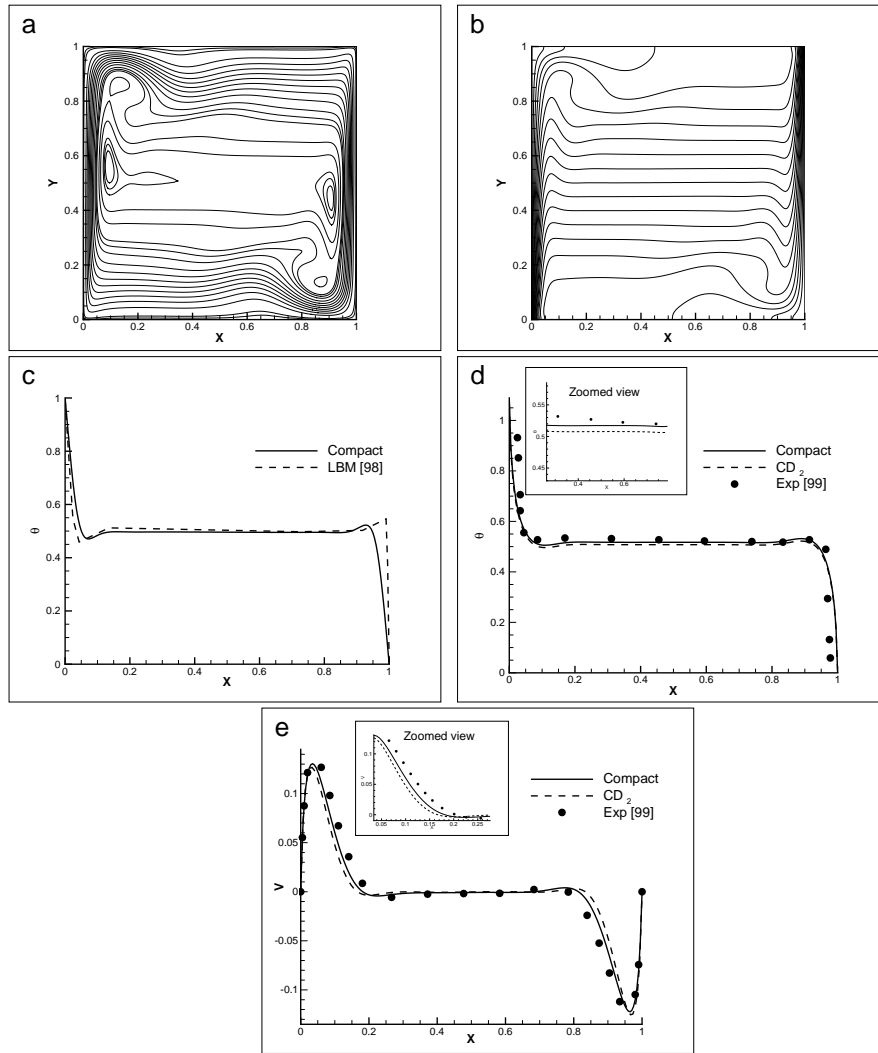


Figure 2.3: Validation of present results with: LBM a-c; Experimental d & e.

results with compact schemes are accurate than CD_2 and are closer to experimental data. From Fig. 2.3, it is noticed that present mathematical model and numerical methods are in good agreement with the earlier results of [98, 99] for turbulent natural convection flows.

2.7 Results and Discussion

The buoyancy driven turbulent flow in a square enclosure with ceiling or horizontal vent is studied numerically and reported for different Grashof numbers. Here, the value of Prandtl number Pr of air is taken as 0.72 for all the cases. The effects of heat source location, vent location and multiple vents on the flow field characteristics are

presented.

2.7.1 Evolution of flow characteristics

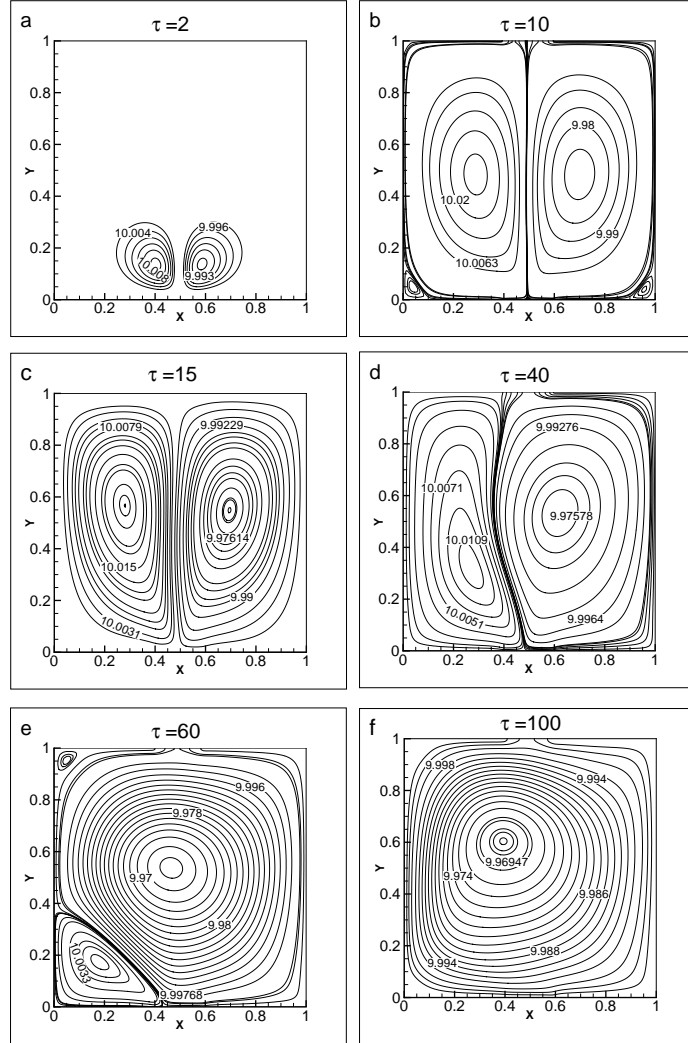


Figure 2.4: Evolution of stream function contours for $Gr = 10^8$.

The evolution of stream function, temperature, vorticity and kinetic energy contours are shown in Fig. 2.4-2.7 for Grashof number $Gr = 10^8$. The heat source of size $0.2H$ is located at the center of the bottom wall. A vent of width $D=0.2H$ is located at the center of ceiling. The stream function contours move upwards from the heat source with increase in time. A density difference arises between the inner (hot) and outer (cold) fluids at the vent. Hence flow is bidirectional across the vent. From Fig. 2.4, a region of recirculation is formed in the cavity due to the interactions between the warmer fluid raising from the heat source and the cold fluid entering through vent. The temperature contours at different time intervals are

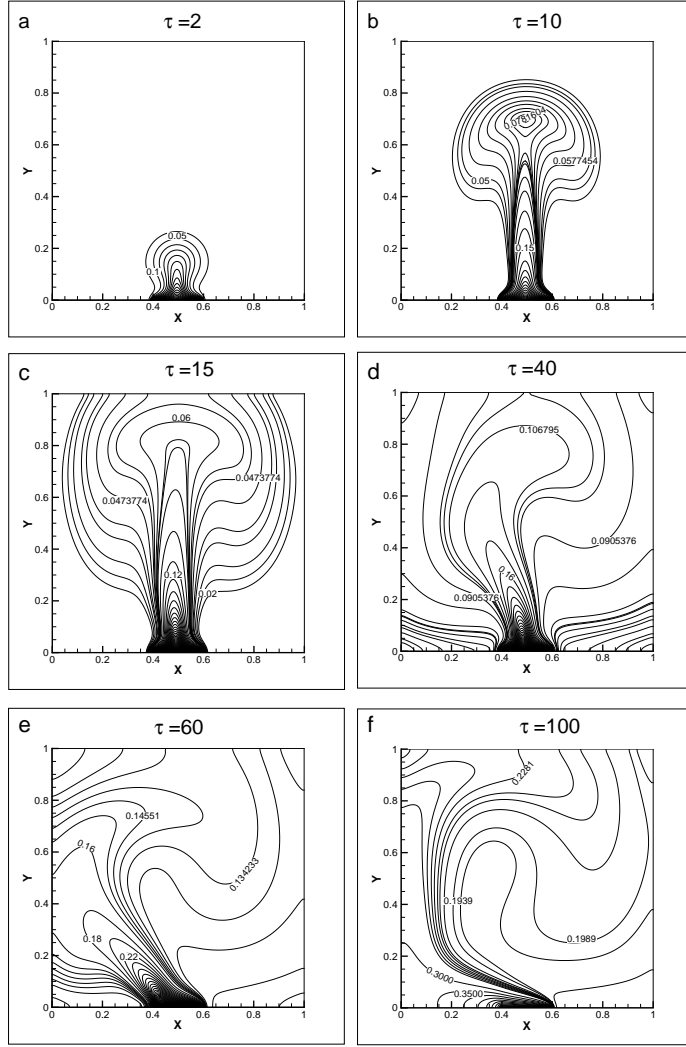


Figure 2.5: Evolution of temperature contours for $Gr = 10^8$.

shown in Fig. 2.5. The thermal plume moves upwards from the heat source and the strength of the plume increases with time. The thermal plume reaches the ceiling at $\tau = 15$. The hot air travel against the ventilated air current whereas the fresh air enters and travels towards the heat source, leading to an excessive flow rotation and eventually an effective mixing of plume and fresh air is visualized inside the enclosure at time $\tau = 40$. This creates more turbulence leading to well-mixed environment inside the enclosure. The entrained air tilts the thermal plume. At the same time the plume acts as a thermal blockage for the ventilation air flow, this creates an additional acceleration of the air stream as it approaches the heat source. Hence the inclination and attachment of the thermal plume towards the left wall are seen at later time intervals $\tau = 60, 100$. The evolution of vorticity patterns at different time intervals are shown in Fig. 2.6. It is noticed that recirculation or

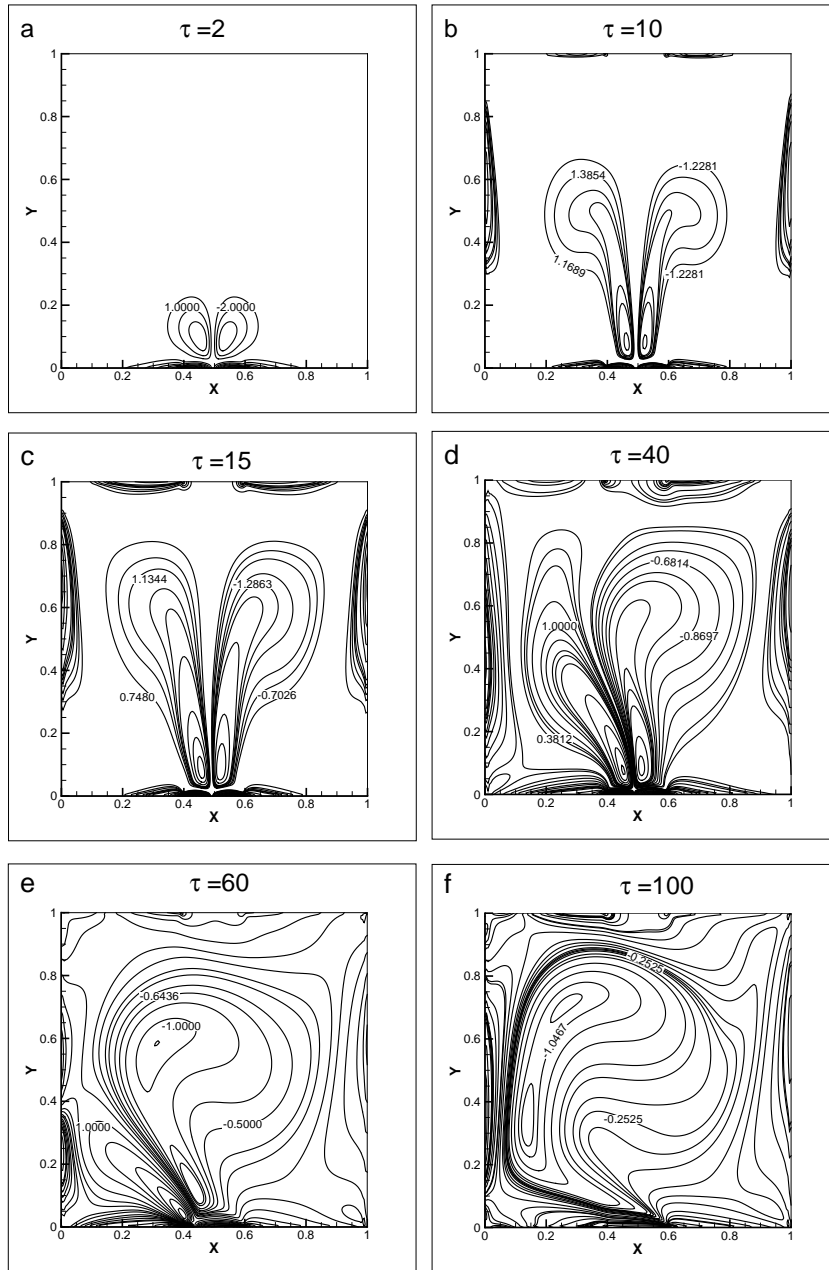


Figure 2.6: Evolution of vorticity contours for $Gr = 10^8$.

effective mixing of hot air and cold air increases with increase in time. The turbulent quantities such as kinetic energy contours at different times are shown in Fig. 2.7. As the flow evolves with time, the kinetic energy is attributed to the fluctuation of the upward rising turbulent thermal plume. The interaction between the hot air and counter cold air at the vent generates swirl flow motion near the ceiling opening at $\tau = 15$ and at later time ($\tau = 15, 60, 100$) more circulations are visualized near the left wall due to tilting of the wall plume.

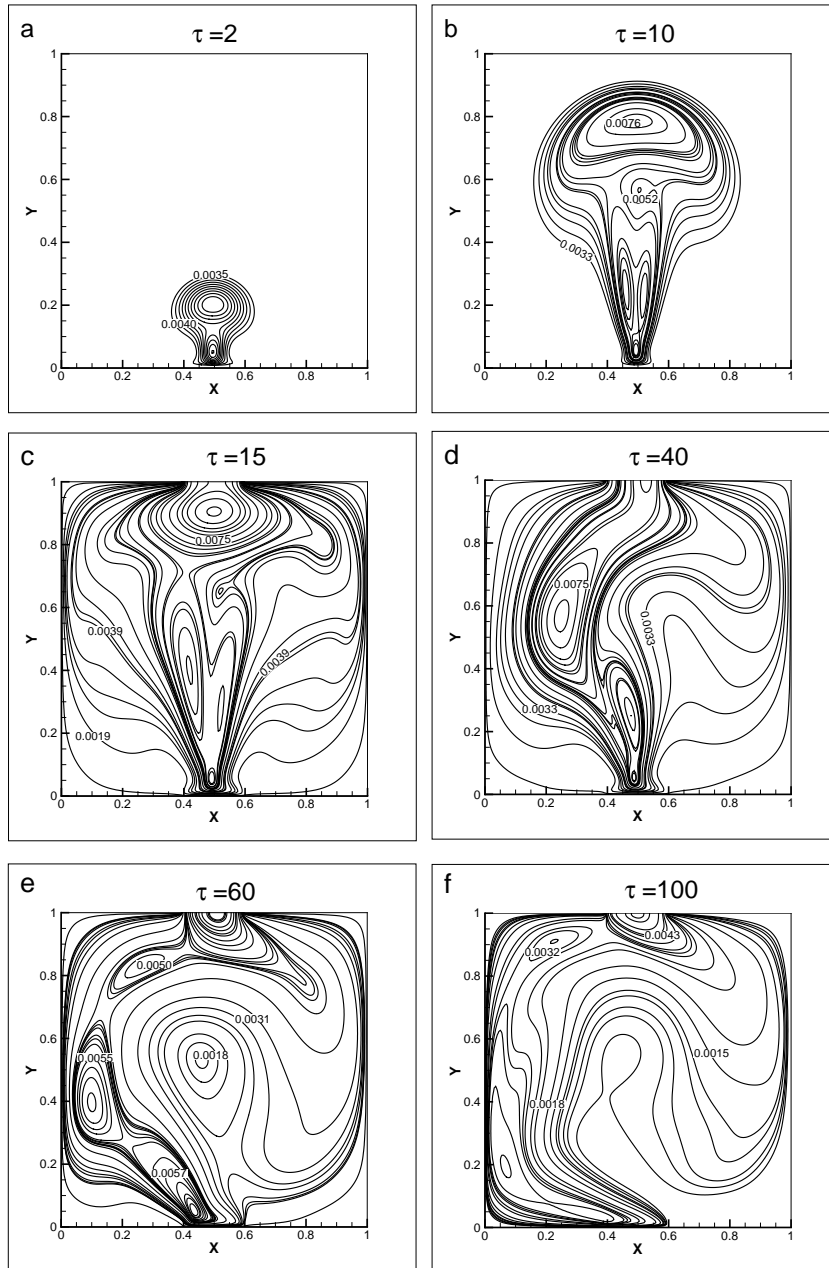


Figure 2.7: Evolution of kinetic energy contours for $Gr = 10^8$.

2.7.2 Effect of Grashof number

The stream function and temperature contours are shown in Figs. 2.8 and 2.9 for Grashof numbers varying from 10^8 to 10^{10} . As the Grashof number increases from 10^8 to 10^{10} , the flow characteristics are highly transient, unstable and complex in the enclosure. In Fig. 2.8(e), two convective cells are formed along with primary circulation in comparison with Fig. 2.8(a&c). In Fig. 2.8(b,d,f), the amount of ambient fluid entering into the enclosure is significant with increase in Grashof

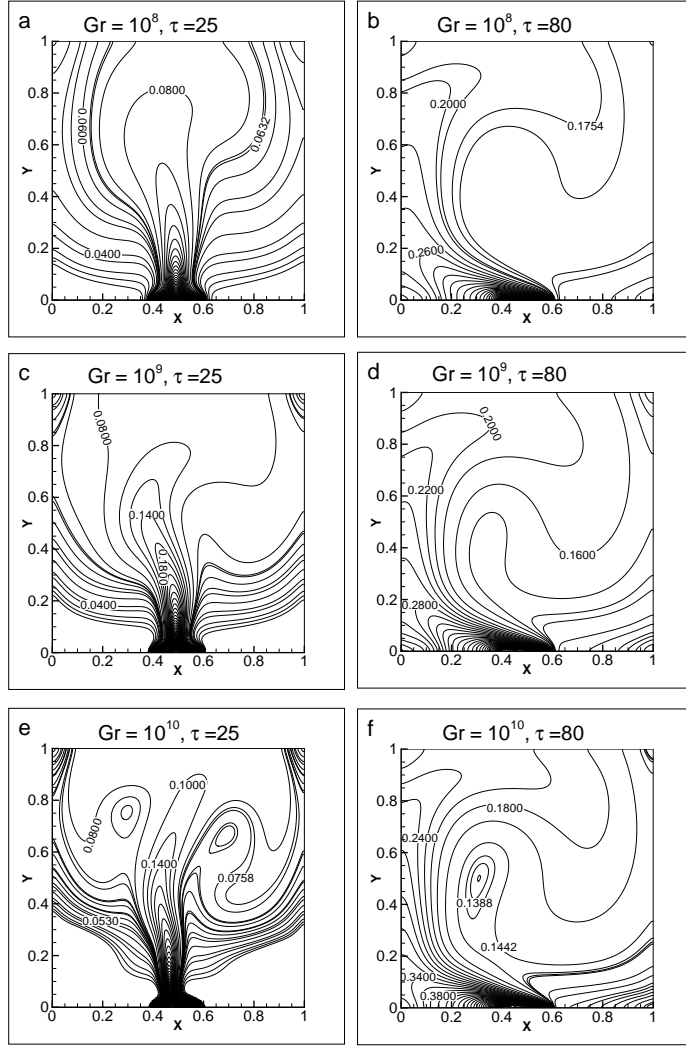


Figure 2.9: Temperature contours at different Grashof numbers.

The normal velocity along the vent is numerically integrated by trapezoidal rule to obtain the net mass flow rate. Fig. 2.11 shows the variation of net mass flow rate with different Grashof number. The net mass flow rate indicates negative sign for particular instance of time when the inflow of ambient fluid is more than the outflow of hot fluid, similarly the positive value represents the vice versa. In an incompressible flow, balance between the inflow and outflow mass flow rate is zero. However, the magnitude of net mass flow rate is very low and the non-zero magnitudes are due to transient buoyancy induced flow instability across the vent. In Fig. 2.11, at time $\tau \geq 150$ quasi-steady state is reached where the inflow and outflow rates are equal. It is observed that the net outflow of hot fluid and inflow of cold air increases with increase in Grashof number. The variation of average Nusselt number on the heat source for different Grashof numbers are presented in Table.2.2.

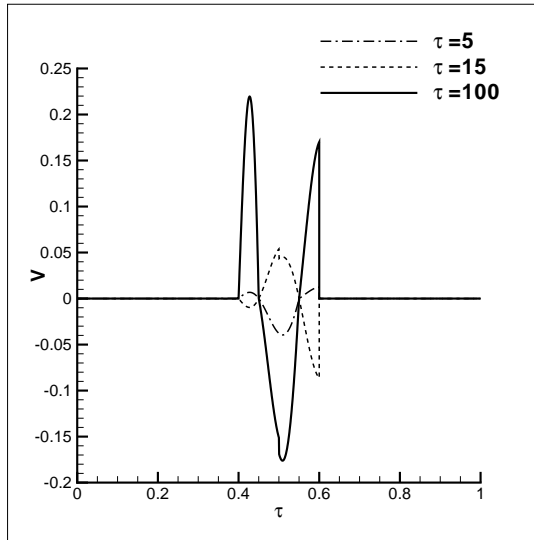


Figure 2.10: Normal velocity profile across the vent for $Gr = 10^{10}$.

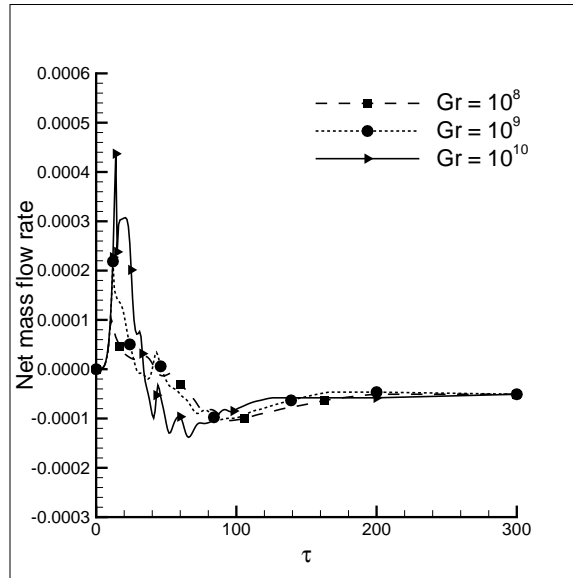


Figure 2.11: Non-dimensional net mass flow rate variation with time through the vent.

The intensity of heat source increases with rise in Grashof number hence the average Nusselt number increases.

Table 2.2: Average Nusselt number variation over the heat source for different Grashof numbers

Grashof Number	Average Nusselt number
10^8	18.631
10^9	39.147
10^{10}	87.238

2.7.3 Effect of heat source location

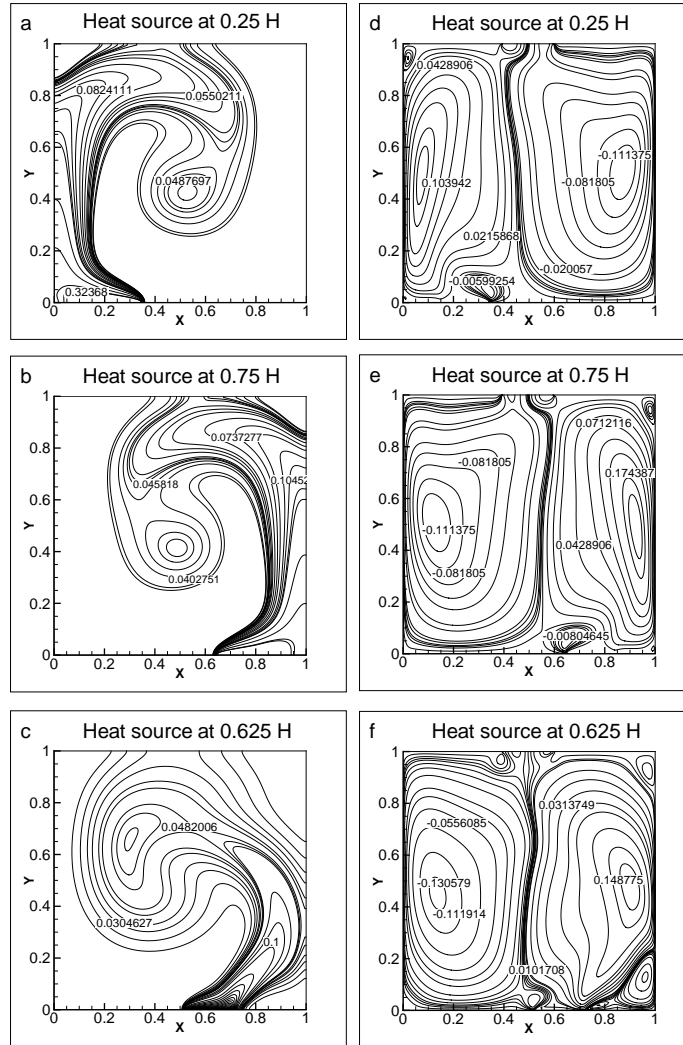


Figure 2.12: Effect of heat source location on: temperature contours (a-c); vertical velocity contours (d-f)

To know the effect of heat source location, results are shown in Fig. 2.12 for different heat source locations. The size of heat source is $0.2H$ and Grashof number is $Gr = 10^8$. The vent is located at the center of the ceiling with a vent width $D = 0.2H$. The heat source is placed at three different locations at $0.25H$, $0.625H$ and $0.75H$ from the left wall. The temperature contours are shown in Fig. 2.12 (a, b & c) and normal velocity contours are shown in Fig. 2.12 (d, e & f). When the heat source is located near the left/right wall and at an intermediate location of $0.625H$, a wall plume is formed which is not axisymmetric and appeared as semi-conical as shown in Fig. 2.12 (a, b & c). The movement of the buoyant plume from a centrally located heat source enhances air to be entrained symmetrically from both sides of

the plume. When the heat source is placed near the left wall, the plume movement is more near the left wall and movement of entrained air is towards the right wall as shown in Fig. 2.12 (d). The opposite trend is observed in Fig. 2.12 (e) when the heat source is placed near the right wall. When the heat source is placed at an intermediate location $0.625H$, the initial plume movement is towards the right wall and as time progresses the plume propagates towards the left wall of enclosure. The vertical velocity contours for intermediate location $0.625H$ indicates that entrainment of ambient air into enclosure is reduced when compared to $0.25H$ and $0.75H$. For a centrally located heat source, the air entrained laterally into the plume gets heated up quickly and assist the plume to spread at a higher rate when compared to near wall heat source.

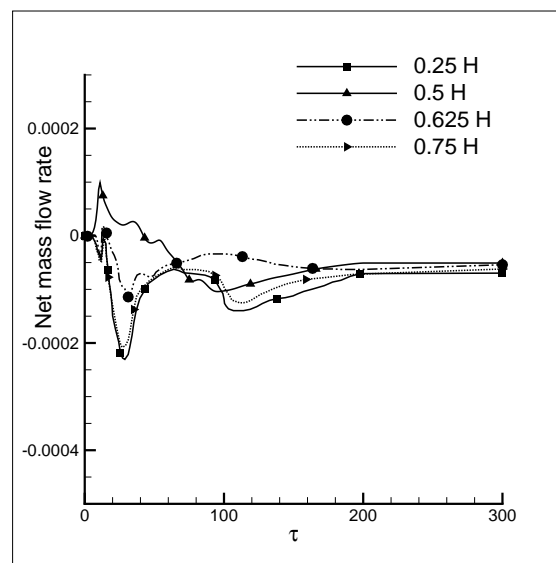


Figure 2.13: Non-dimensional net mass flow rate with diiferent heat source locations for $Gr = 10^8$.

The variation of net mass flow rate through the vent with time for different heat source locations are shown in Fig. 2.13. It is noticed that till $\tau \leq 70$, the magnitude of hot fluid leaving the enclosure is higher for centrally located heat source compared to heat source located near the left, right wall and intermediate location. Moreover for heat sources located away from center location ($0.5H$), the entrainment of ambient air is significant. At time $\tau \geq 70$, outflow of hot fluid through the vent from heat source located at intermediate location $0.625H$ is higher. As the flow progresses, at $\tau \geq 150$ quasi-steady state condition is reached and hence the deviations in the net mass flow rate observed initially due to difference in heat source location decreases. From Fig. 2.13, it can be concluded that the initial movement of thermal plume across the vent from a centrally located heat source is significant when compared to cases with near

wall heat source.

2.7.4 Effect of vent location

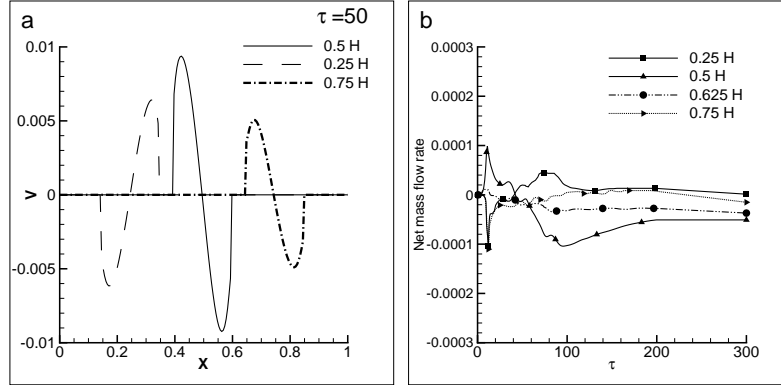


Figure 2.14: (a) Normal velocity profile; (b) Non-dimensional net mass flow rate with different vent locations for $Gr = 10^8$.

A heat source of size $0.2H$ is located at the center of the bottom wall. The ceiling vent is placed at three different locations at $0.25H$, $0.625H$ and $0.75H$ from the left wall. The normal velocity profile along the vent is shown in Fig. 2.14 (a) for different ceiling vent locations. It is noticed that normal velocity is high when the ceiling vent is located at the center compared to the case when vent is located near the left and right wall. The net mass flow rate variation with time for different ceiling vent locations are shown in Fig. 2.14 (b). Significant amount of hot fluid leaves through the vent located at $0.5H$ till time $\tau \leq 45$, and as time progresses ambient air infiltrates into the enclosure. The entrainment is significant through vents located at $0.25H$ and $0.75H$ till time $\tau \leq 45$, and at later till time $\tau \leq 100$, the amount of hot fluid leaving through vent located at $0.25H$ is significant when compared to $0.75H$. Quasi-steady state condition is reached at $\tau \geq 150$ and hence the deviations in the net mass flow rate observed initially between vent location $0.25H$ and $0.75H$ decreases. Hence, it is clearly evident that the entrained air flow rate is dependent on the heat source and ceiling vent locations.

2.7.5 Effect of two vents

The normal velocity and net mass flow rate are shown in Fig. 2.15 (a&b) with two ceiling vents for Grashof number $Gr = 10^8$. The heat source is located at the center of the bottom wall with a size of $0.2H$. Two vents of equal width $0.1H$ are located at $0.25H$ and $0.75H$ from left side wall. The normal velocity profile along the two vents at different times are shown in Fig. 2.15 (a) for $Gr = 10^8$. The flow rates through

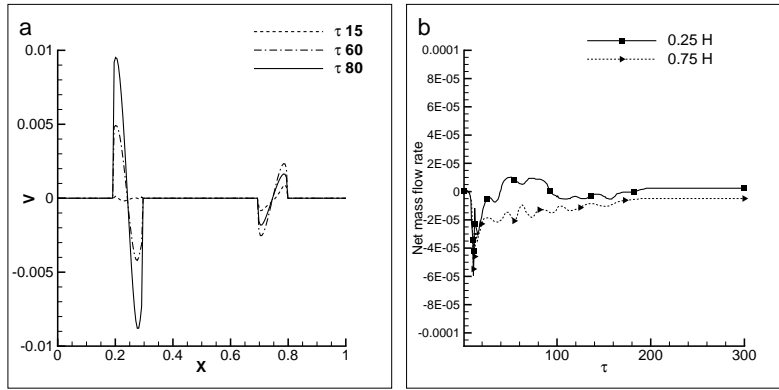


Figure 2.15: (a) Normal velocity profiles across two vents; (b) Non-dimensional net mass flow rate through two vents for $Gr = 10^8$.

two vents are equal at initial time but as time progress, the flow rate is significantly higher through upstream vent when compared to downstream vent. Figure 2.15 (b) represents the comparison of net mass flow rate variation with time through the two ceiling vents and it is observed that till time $\tau \leq 15$ net flow rates through the two vents are equal. As time progresses till $\tau \leq 100$ an increase in flow magnitudes are visualized through the first vent since more quantity of hot fluid leaves through it when compared to the second vent. However, a quasi-steady state condition is reached at $\tau \geq 100$ where the inflow and outflow rates through the two vents are balanced with equal proportion of hot fluid leaving and ambient fluid entering through the two vents. Hence the difference in the net mass flow rate between the two vents decreases after approaching quasi-steady state condition.

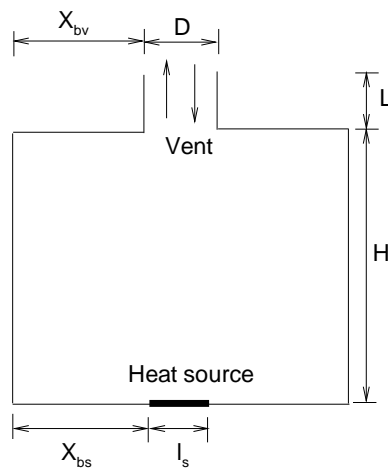


Figure 2.16: Schematic diagram of square enclosure with vent thickness

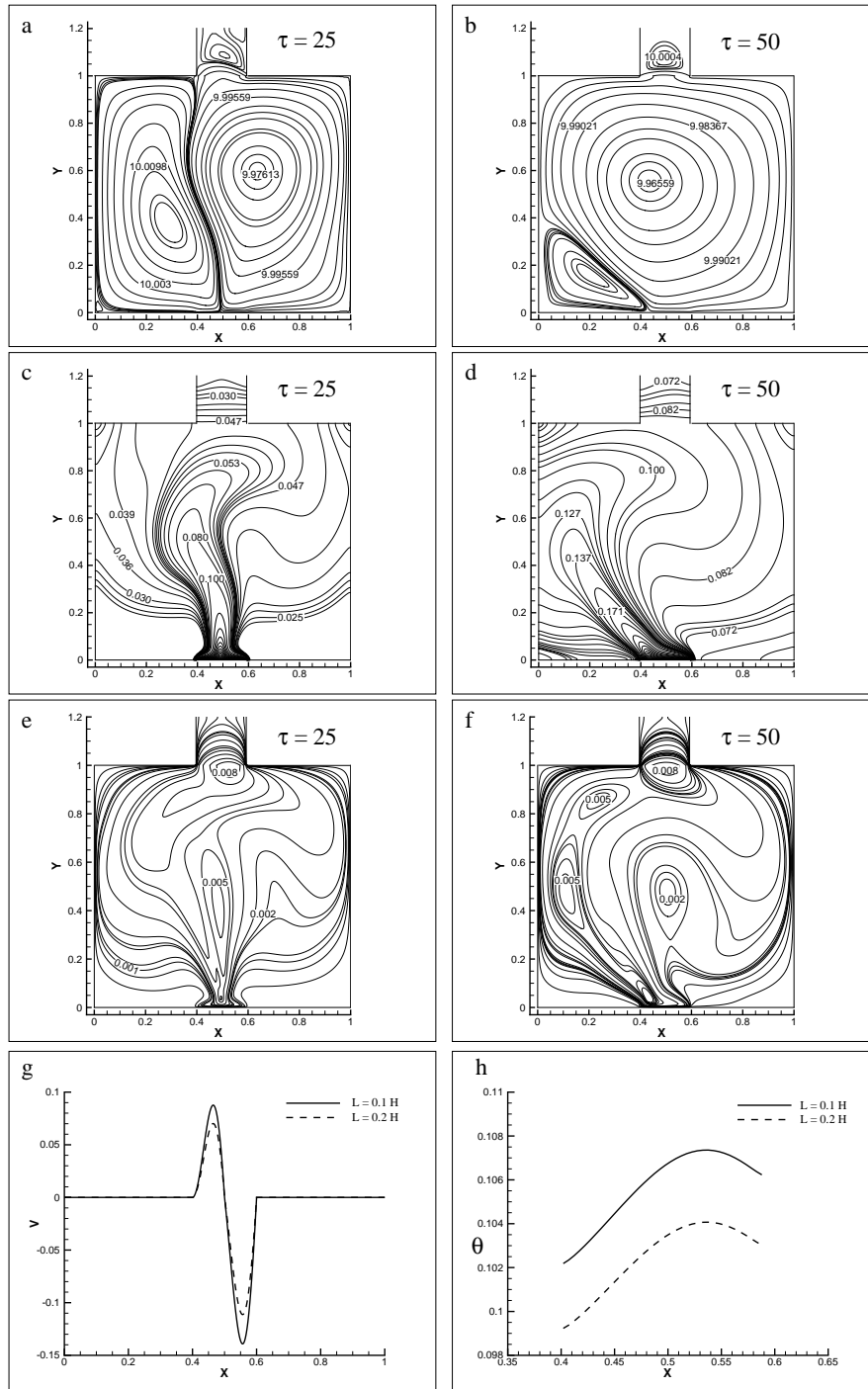


Figure 2.17: Stream function(a&b), temperature(c&d), kinetic energy(e&f) contours in a square enclosure for $Gr = 10^8$. Variation of normal velocity (g) and temperature (h) profiles along the top vent with different vent thickness.

2.7.6 Effect of vent thickness

Fig.2.16 represents the schematic diagram of square enclosure with vent thickness (L). Fig. 2.17 shows the effect of ceiling vent aspect ratio in a square enclosure with

stream function, temperature and turbulent kinetic energy contours for $Gr = 10^8$. The centrally located heat source and vent are of size $l_s = 0.2H$, $D = 0.2H$ with vent thickness $L = 0.2H$. From Fig. 2.17(a & b) as time progresses, stream function contours move upwards and a region of recirculation is formed across the vent due to interactions between hot and cold fluids. In Fig. 2.17(c & d), entrained air tilts the thermal plume towards the left wall. As the flow evolves with time, turbulent kinetic energy is attributed to fluctuation of upward rising turbulent thermal plume. In Fig. 2.17(e), at $\tau = 25$ the kinetic energy contours depicts the interaction between hot air and cold air at the vent generating swirl flow motion near the ceiling opening. As flow evolves more circulations are visualized near the left wall due to tilting of thermal plume. The normal velocity and temperature profile along the vent top for different vent thicknesses are shown in Fig. 2.17(g & h). The normal velocity and temperature decreases with increase in vent thickness. This is due to the decrease in volume flow rate across horizontal vent.

2.7.7 Entrainment effects through horizontal and vertical vents

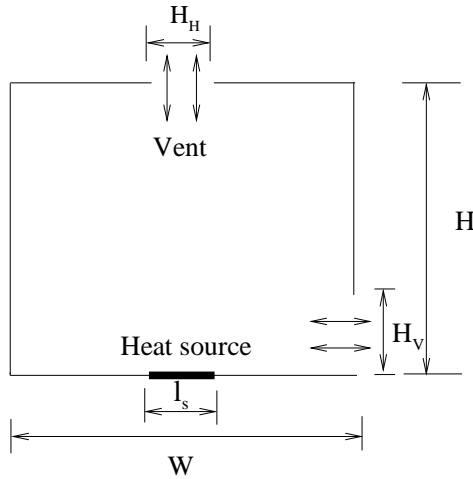


Figure 2.18: Schematic diagram of square enclosure with vertical and horizontal openings.

Further investigations are performed to understand buoyancy induced flow in partial enclosure with combinations of horizontal and vertical vents. The schematic diagram is shown in Fig.2.18. The enclosure top wall has a horizontal vent of size $H_H = 0.15W$ which is opened to the ambient environment. Similarly the right wall lower portion has a vertical vent of size $H_V = 0.3W$. The plume behavior in square and rectangular enclosures are investigated in the present study for height (H) to width (W) aspect ratios $A.R = 1, 2$.

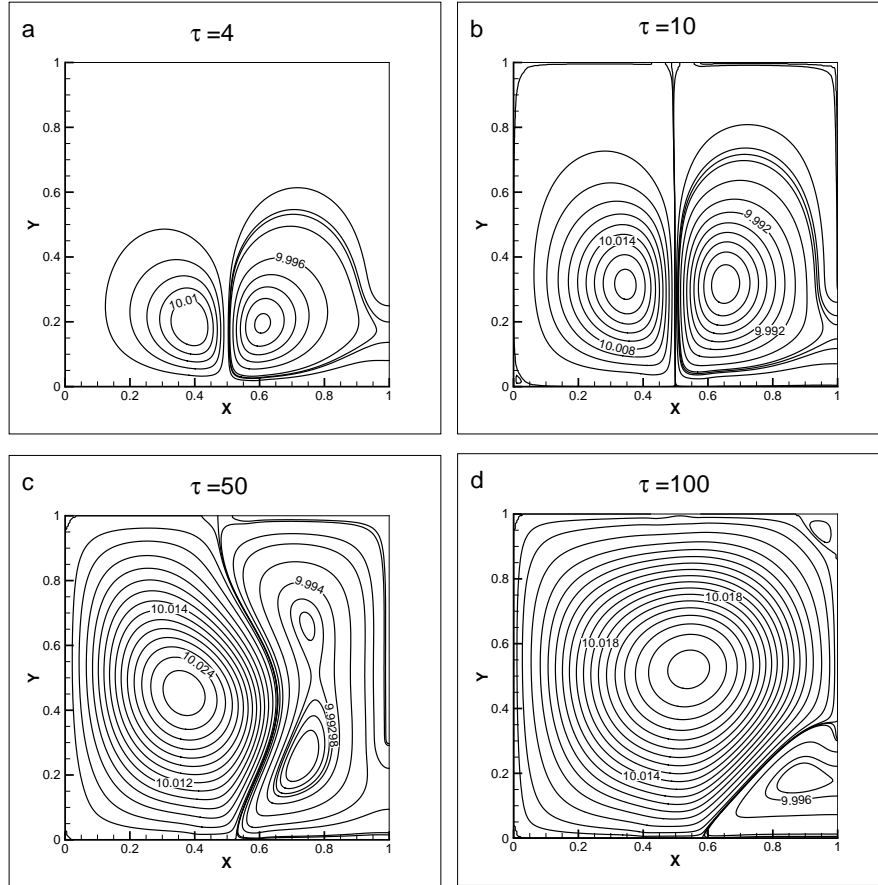


Figure 2.19: Evolution of Stream function contours in square enclosure

The illustrations shown in Fig.2.19 (a-d) represents the evolution of stream function contours in square enclosure for Grashof number $Gr = 10^9$. At the initial time interval $\tau = 4$ entrained air flows into the enclosure through the vertical vent. Density difference arises at the vent due to the temperature difference between the inner hot fluid and outer ambient fluid. The lighter hot fluid leaves the enclosure through the vent meanwhile the cold ambient fluid enters into the cavity. As the flow progresses at $\tau = 10$ cold air creeps into the enclosure through the horizontal and vertical vents. The flow is bidirectional across the openings. Two recirculation regions are formed inside the cavity and recirculation cells represents the movement of hot and cold fluid. At $\tau \geq 50$ the movement of hot fluid is significant towards the right half of the enclosure. The hot fluid mixes with the entrained air and forms larger convective cell inside the enclosure at $\tau = 100$.

The illustrations in Fig.2.20(a-d) represents the evolution patterns of stream function contours in rectangular enclosure for $Gr = 10^9$. The stream function contours represents the well mixing of fluids and patterns of multi-recirculating

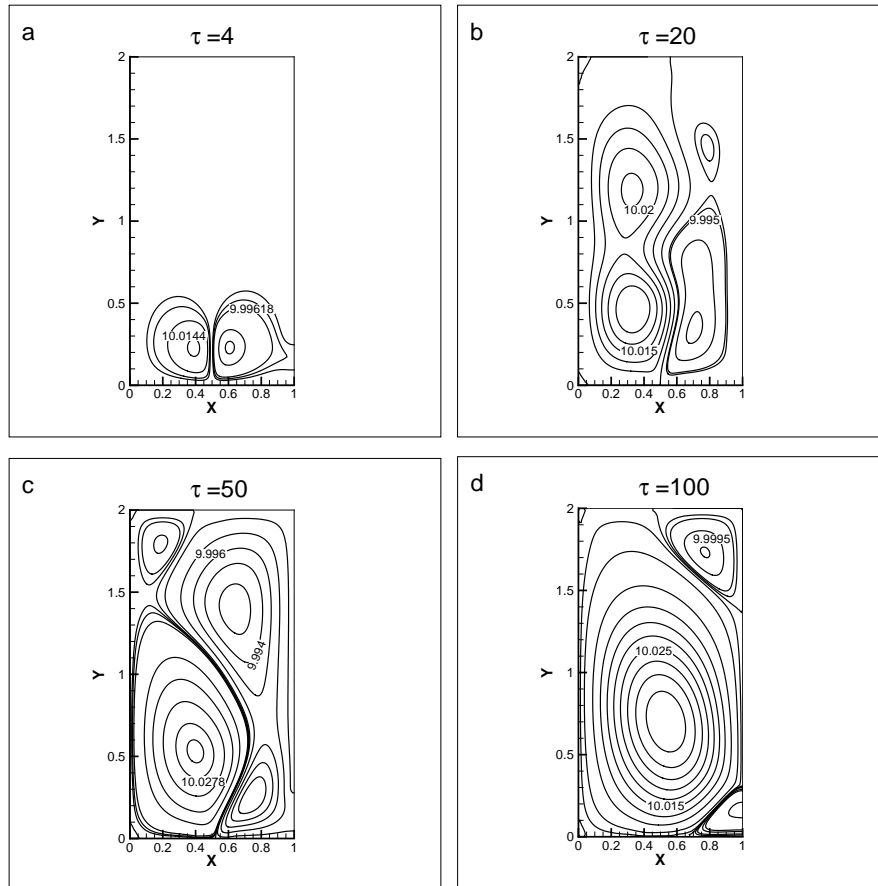


Figure 2.20: Evolution of Stream function contours in rectangular enclosure

convective cells are seen at $\tau = 20$ & 50 . As flow progresses, the convective cells merge and a larger convective cell is visualized at time $\tau = 100$.

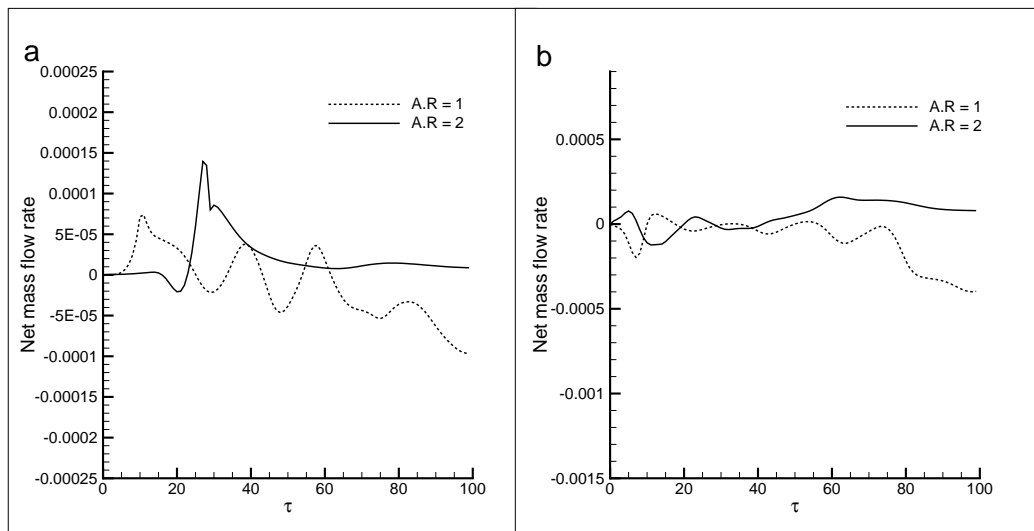


Figure 2.21: Effect of aspect ratio on net mass flow rate (a) horizontal vent (b) vertical vent.

The effect of aspect ratios on the mass flow rate are investigated by comparing vent mass flow rates between square (A.R=1) and rectangular cavity (A.R=2) and are shown in Fig.2.21 for $Gr = 10^9$. Fig.2.21(a&b) represents the net mass flow rate through horizontal vent and vertical vents. It is visualized from Fig.2.21(a) that for higher aspect ratio the plume reaches the ceiling at $\tau \geq 25$. It is evident from Fig.2.21 that with increase in aspect ratio there is a significant decrease in the ambient entrainment rates through the openings.

2.8 Summary

The buoyancy-induced turbulent flow generated by a heat source in a square enclosure with single and multiple ceiling vents are investigated and presented in this chapter. The fluid flow characteristics in the enclosure are reported for various parameters such as Grashof number, location of heat source and location of ceiling vent. The flow is found to be oscillating and bidirectional across the vent due to buoyancy effects. As the Grashof number increases from 10^8 to 10^{10} , the flow becomes highly transient, unstable and chaotic in the enclosure. The intensity of turbulence increases with increase in Grashof number, increasing the entrained ambient air flow rate through the vent. The thermal plume spreading rate from centrally located heat source is higher when compared to heat source placed near the wall. The entrainment of ambient air is significant when the heat source is placed away from the center location. The amount of entrainment depends on the heat source and vent locations. Hence ceiling vent location is most important parameter for growth and spreading of plume. The initial flow rate is higher through vent located at the upstream side of heat source compared to vent located at downstream side of heat source till quasi-steady state condition. The discharge rate through ceiling vent increases with reduction in vent thickness. Present results would be useful for understanding the growth and spread of thermal plume inside ceiling vented enclosure.

Chapter 3

Buoyant flows in vertical shaft

In tall buildings, there are internal flow passages such as open elevator shafts, stairwells which are integral part of modern buildings. During fire accidents, elevator shafts which are vertical channels facilitate the fire transport phenomena due to stack effects and are connected to upper floors through vertical openings such as doorways. This poses a threat to human life at remote locations from the fire. Fire safety measures such as vertical barriers and smoke vents reduces the impact of fire accidents by controlling the fire spreading rate.

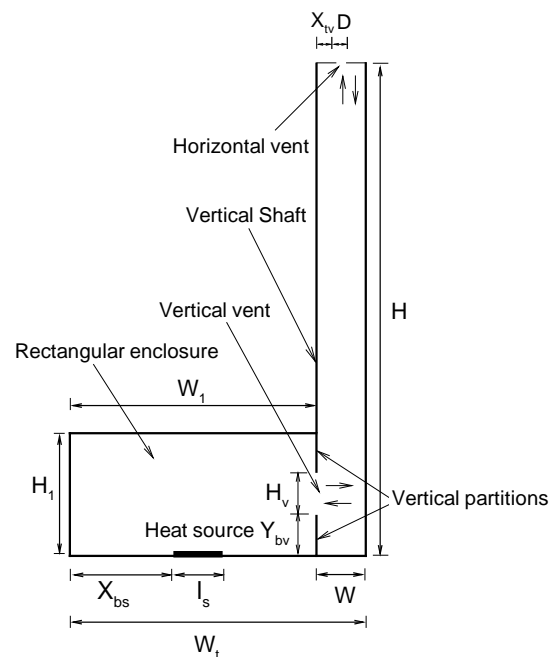


Figure 3.1: Schematic diagram of rectangular compartment connected to vertical shaft

3.1 Problem definition

In this chapter, computational study is performed on the buoyancy induced turbulent flow characteristics in a vertical shaft connected to an adjacent rectangular compartment which are the integral part of high-rise buildings. The schematic diagram is shown in Fig 3.1. There is a finite-size heat source at constant temperature T_s located at the bottom wall of rectangular enclosure and vertical partition connecting vertical shaft. The shaft has a horizontal vent of width D above to the ambient media at temperature T_∞ . Here, the value of Prandtl number Pr of air is taken as 0.72 for all the cases. The dimensions of the compartment are $0.5H \times 0.25H$ and the heat source size of $l_s = 0.1H$ is located centrally. The vertical shaft has height (H) to width (W) aspect ratio of 10 with centrally located horizontal vent of width $D = 0.05H$.

3.2 Grid Independence

Figure 3.2 (a & b) shows the temperature profile along the horizontal wall at the center of the rectangular compartment and at the center of the vertical shaft with different grid sizes of 100×200 , 150×400 and 200×500 for $Gr = 10^{11}$. Simulations were performed to determine the net mass flow rate variation with time for rectangular compartment with two vertical passages located in its left and right walls each of height $H_v = 0.1H$ with three different grid sizes. Figure 3.2(c) shows the net mass flow rate variation along the vertical passage connecting compartment and shaft with three different grid sizes and the results are grid independent with grid size of 150×400 . From Figure 3.2, it is noticed that the solution is grid independent with grid size of 150×400 . Hence all simulations are reported with this grid size.

3.3 Validation

The accuracy of the present numerical model are validated with experimental and numerical results available in the literature. Xaman et al. [100] numerically analyzed the turbulent natural convection flow in a tall cavity that has a differentially heated vertical walls and adiabatic upper and bottom walls by finite difference method for Rayleigh number $Ra = 10^{12}$. They have chosen the aspect ratio of height to width as 20. The stream function and temperature contours shown in Figure 3.3 (a&b) are

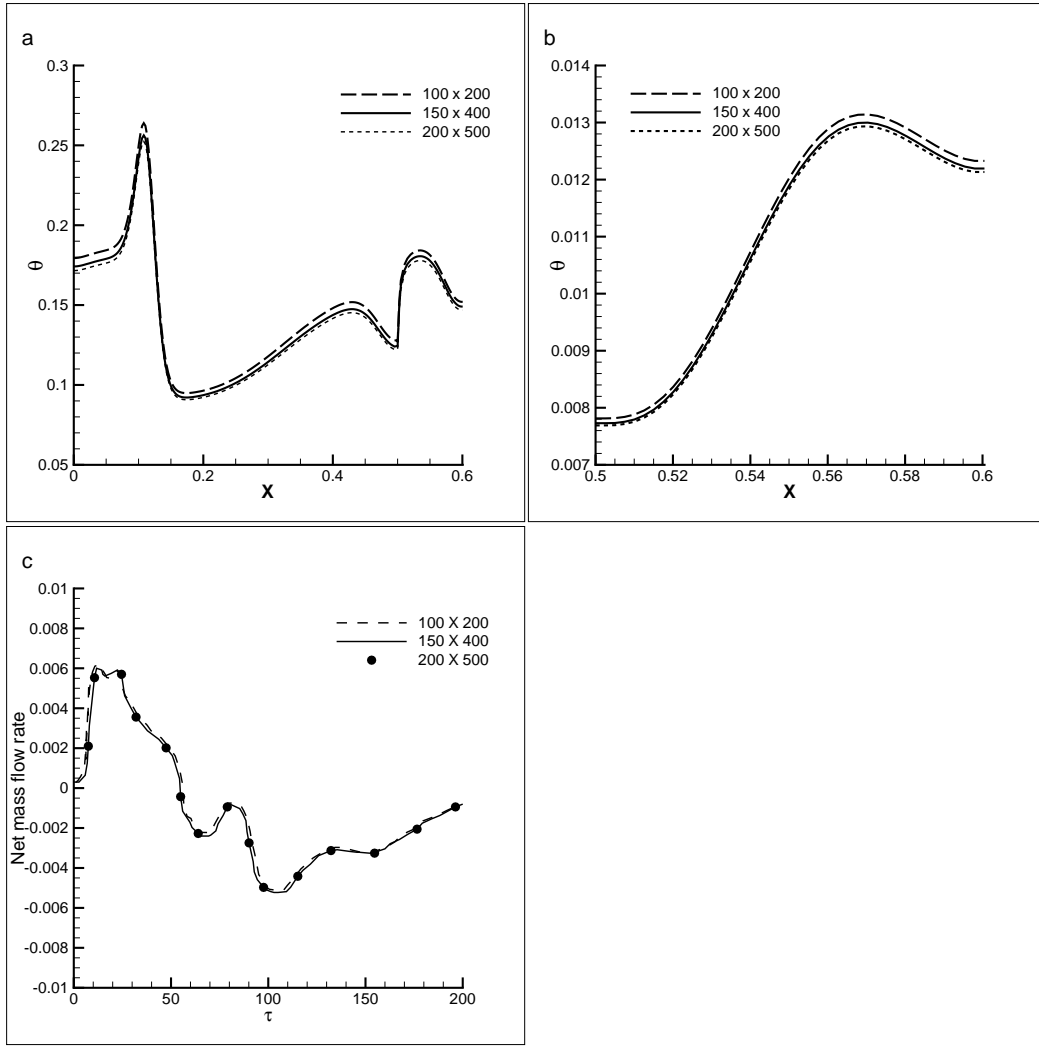


Figure 3.2: Non-dimensional temperature profile at the mid-height for $Gr = 10^{11}$:(a) compartment and (b) Vertical shaft; (c) Non-dimensional net mass flow rate variation through vertical passage.

matching well with the numerical results [100]. The experimental study on the turbulent natural convection flow in a tall cavity that has a differentially heated vertical walls and adiabatic upper and bottom walls for $Ra = 0.86 \times 10^6$ are reported in [101]. The hot and cold plates are of polished aluminum backed by temperature controlled water jackets and the water passes upwards along channels behind each plate with independent flow control of each channel to ensure equality of temperature across the plates. The vertical plates are maintained at constant temperatures of 19.6°C and 39.9°C with corresponding Rayleigh number $Ra = 0.86 \times 10^6$. The vertical velocity and temperature profiles along the horizontal wall at the center of the tall cavity are shown in Figure 3.3 (c&d). The temperature and velocity profiles agreed well with the experimental results of Betts and Bokhari [101]. From Figure 3.3, it is noticed that present mathematical model and numerical

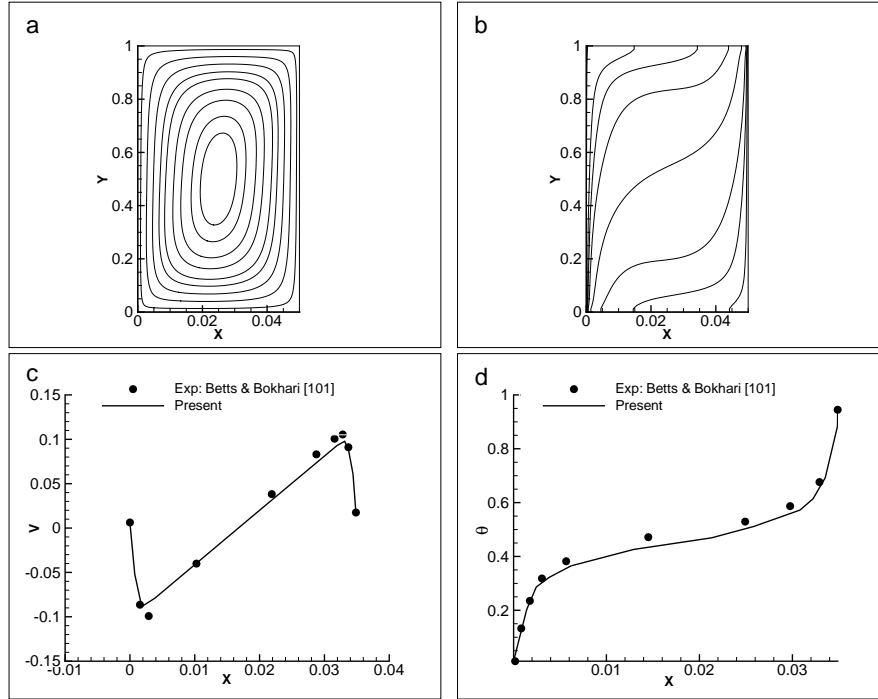


Figure 3.3: Validation of present non-dimensional results with:(a&b) Numerical (Xaman et al.[100]); (c&d) Experimental (Betts and Bokhari [101])

methods are in good agreement with the earlier results[100, 101] for turbulent natural convection flow in a tall cavity.

The accuracy of the present two-dimensional (2D) model is compared with three-dimensional (3D) model where the vertical passage is not present across the entire width of compartment. The 3D simulations are performed by Large Eddy Simulation (LES) using Fire Dynamic Simulator (FDS) code developed by National Institute of Standards and Technology (NIST). A total number of 3,44,000 cells are used in 3D simulation. The rectangular compartment is 0.475 m wide, 0.25 m high, and 0.2 m deep. The vertical passage is 0.025 m wide, 0.225 m high, 0.18 m deep and the compartment is connected to the shaft through the passage. The adjacent tall shaft is 0.1 m wide, 1.0 m high, and 0.2 m deep. The width and depth of centrally positioned heat source is 0.1 m with $Gr = 10^{11}$. Figure 3.4 (a&b) indicates the temperature contours at time 5 and 200 seconds along the xy plane at $z=0.1$ m. From Figure 3.4 (a&b), the plume rises from the heat source and propagates deep into the shaft through the vertical passage. Similar transport phenomena of thermal plume are observed with present simulations. Figure 3.4 (c) represents the non-dimensional temperature variation along the vertical center line of the shaft. It is visualized that temperature is higher at the lower portion of shaft and

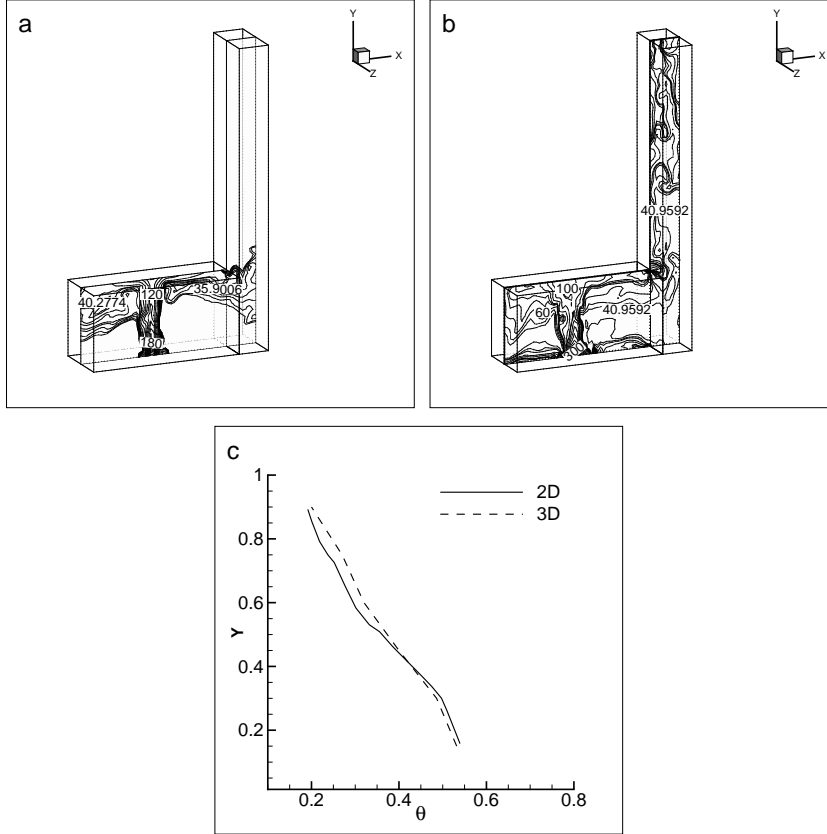


Figure 3.4: Temperature contours (a,b) at slice plane $Z=0.1$ for $Gr = 10^{11}$; (c) Non-dimensional temperature variation along shaft vertical axis.

temperature decreases with increase in altitude along the vertical center line of shaft. Since the ratio of cross-sectional area between the compartment, vertical passage and shaft are different from 2D to 3D flows slight deviations are visualized in the temperature profiles.

3.4 Results and Discussion

3.4.1 Evolution of flow characteristics

Figures. 3.5 and 3.6 represents the stream function and temperature contours for compartment connected to shaft without vertical partition. The Grashof number is $Gr = 10^{10}$. The stream function contours moves upwards from the heat source towards the ceiling of rectangular compartment. The compartment is filled with hot fluid at time $\tau = 10$ and plume enters into the shaft through vertical passage. A density difference arises between the hot and the ambient fluids present in the two enclosures, and this further accelerate the mixing of fluids through the vertical passage. Hence

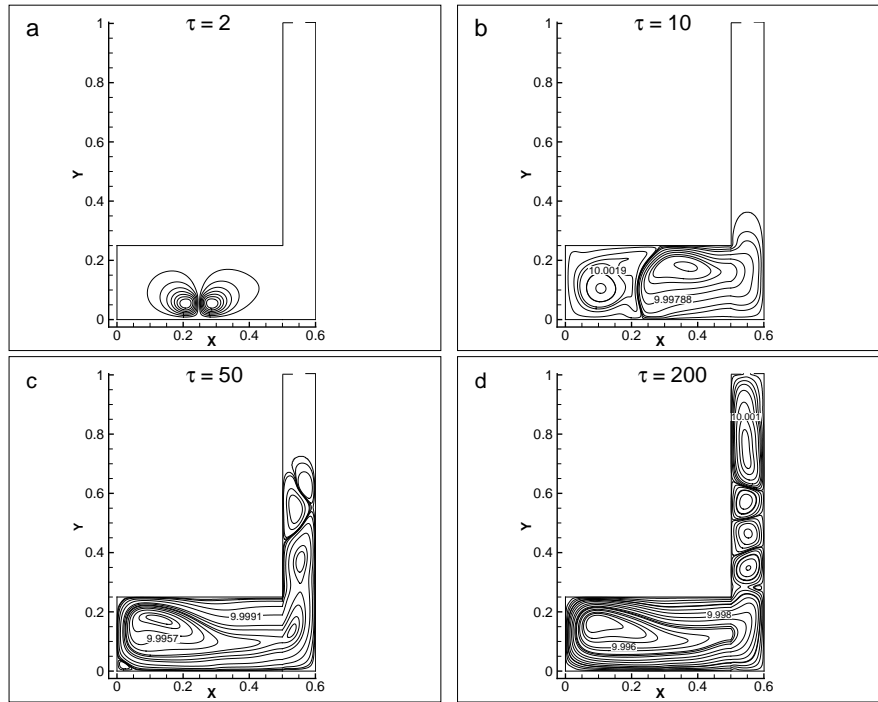


Figure 3.5: Evolution of stream function contours for $Gr = 10^{10}$

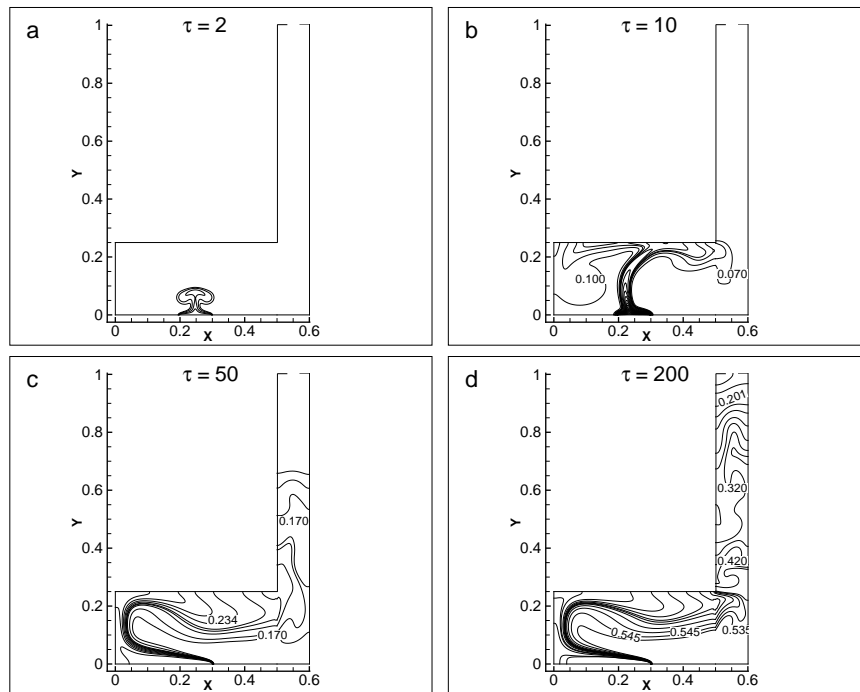


Figure 3.6: Evolution of temperature contours for $Gr = 10^{10}$

the flow is bidirectional at the opening passage between the compartment and the shaft. As the time progresses above $\tau \geq 10$, the hot fluid spreads inside the shaft and leaves through the exhaust or horizontal vent. The confined solid wall boundaries

trap the heat and restrict the horizontal movement of air and hence generate more air circulations inside the shaft. The stream function contours indicate a pattern of complex flow structure with multi-recirculating convective cells driven by buoyancy force throughout the core region of the shaft as shown in Fig. 3.5(d). At the shaft outlet, the cold air is entrained into the shaft due to buoyancy and this further accelerates the swirl flow motion near the exhaust. The flow pattern with effective mixing and excessive flow rotations indicates that transport phenomena is complex in vertical shaft.

The temperature contours at different time intervals are shown in Fig. 3.6 (a-d). The thermal plume moves upwards from the heat source and the strength of the plume increases with increase in time. The thermal plume reaches the ceiling of compartment at $\tau = 10$ and propagates into the vertical shaft. Meanwhile, cold fluid from the shaft penetrates through the vertical passage into the compartment due to density difference. The infiltrated cold air tilts the plume towards the left wall of compartment. Hence inclination and attachment of the thermal plume towards the left wall of the compartment is visualized at time $\tau \geq 50$. As the plume migrates further inside the shaft, the shape of the plume is transformed as a wall plume with elongation of flame height and reduction in radius of flame.

3.4.2 Effect of Grashof number

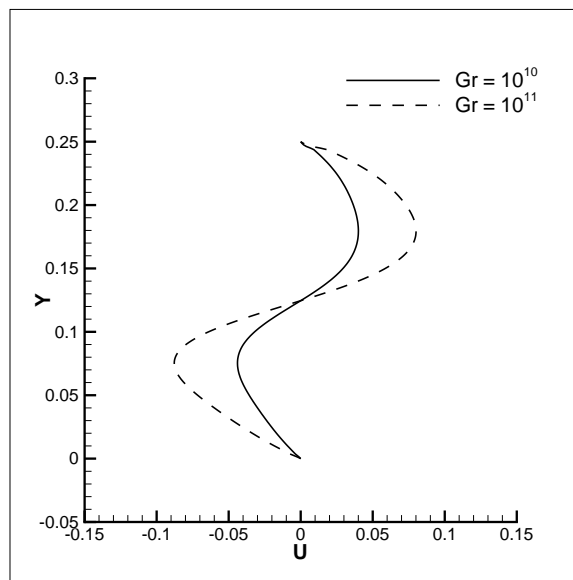


Figure 3.7: Comparison of longitudinal velocity profiles across vertical passage for different Gr

Figure 3.7 and 3.8 represents the longitudinal velocity profiles and net mass flow

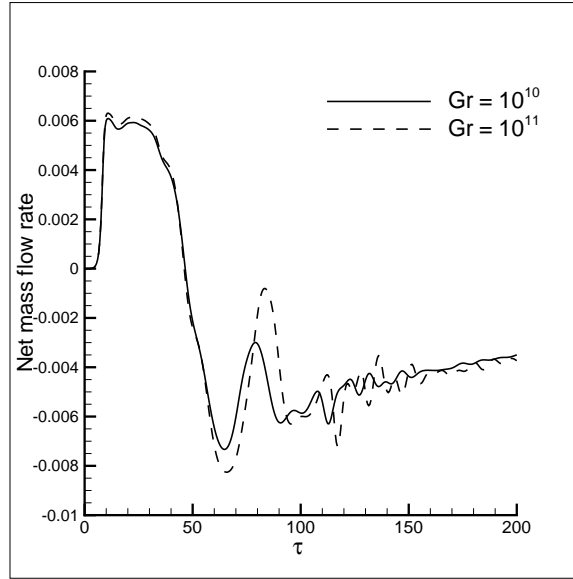


Figure 3.8: Comparison of net mass flow rate across vertical passage for different Gr

rate through the vertical passage for two different Grashof numbers. In Fig.3.7, the positive values represents the plume velocity and negative values indicates the entrainment from vertical shaft. The buoyant gas accumulates near the rectangular compartment ceiling and enters into the shaft through upper half of vertical passage; meanwhile, ambient air penetrates through lower half of the passage. The bidirectional exchange of hot and cold fluid rises by increasing Grashof number. The negative values in net mass flow rate indicates the back-flow from vertical shaft into the compartment.

3.4.3 Effect of vertical passage

To know the effect of vertical passage between the compartment and vertical shaft, results of stream function and temperature contours are shown in Fig. 3.9 with the vertical vent height $H_v = 0.05H$ for Grashof number $Gr = 10^{10}$. From Fig. 3.9(a&c), the vertical barrier restricts the free movement of fluid near the right boundary of compartment and reduction in vertical passage decreases the amount of thermal plume penetrating into the vertical shaft. Moreover less amount of infiltrated air enters the compartment significantly reduces the mixing of hot and cold fluid inside the compartment. Hence in Fig.3.9 (d), significant tilting of the thermal plume is not visualized even at later time intervals $\tau = 100$. The intensity of thermal plume inside the compartment is higher and significant decrease in temperature is visualized through the central core of the shaft. Figure 3.10 represents the net mass flow rate with different sizes of vertical passage. The reduction in vertical passage

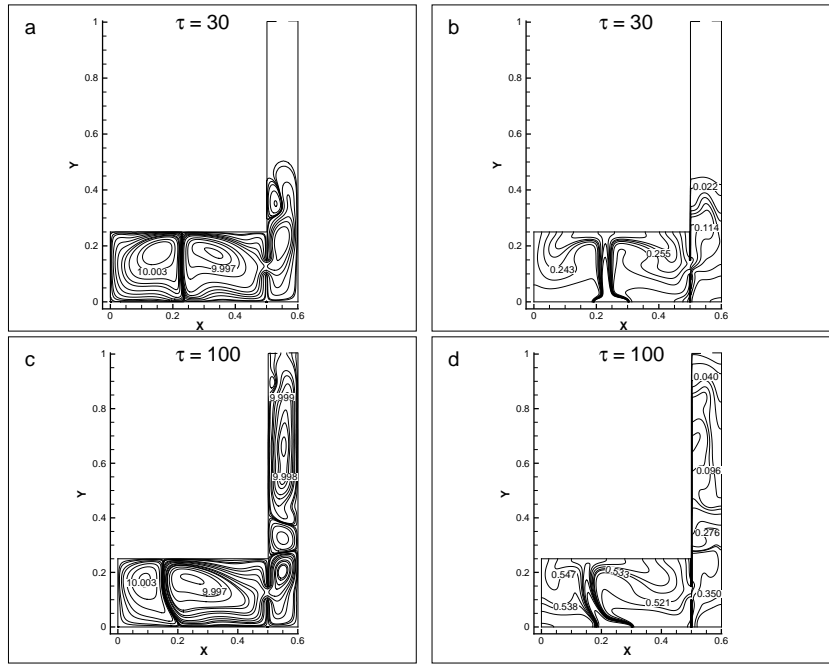


Figure 3.9: Evolution of stream function contours (a,c), temperature contours(b,d) with vertical passage of height $H_v = 0.05H$ for $Gr = 10^{10}$.

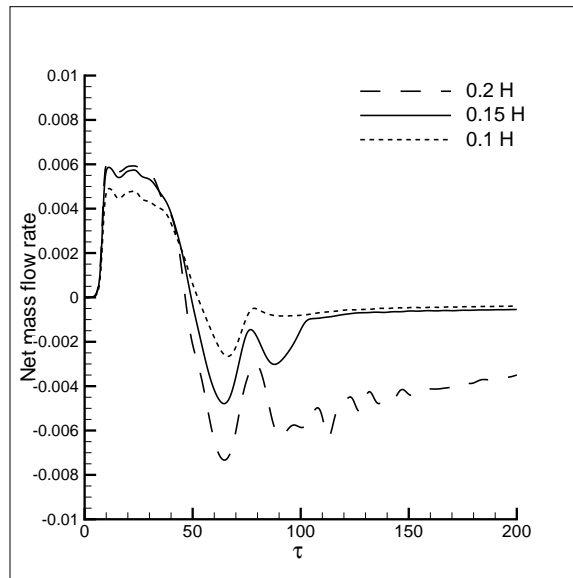


Figure 3.10: Comparison of net mass flow rate for different vertical passage size

decreases the amount of thermal plume penetrating into the vertical shaft. Moreover, less amount of infiltrated air enters the compartment and significantly reduces the mixing of hot and cold fluid inside the compartment.

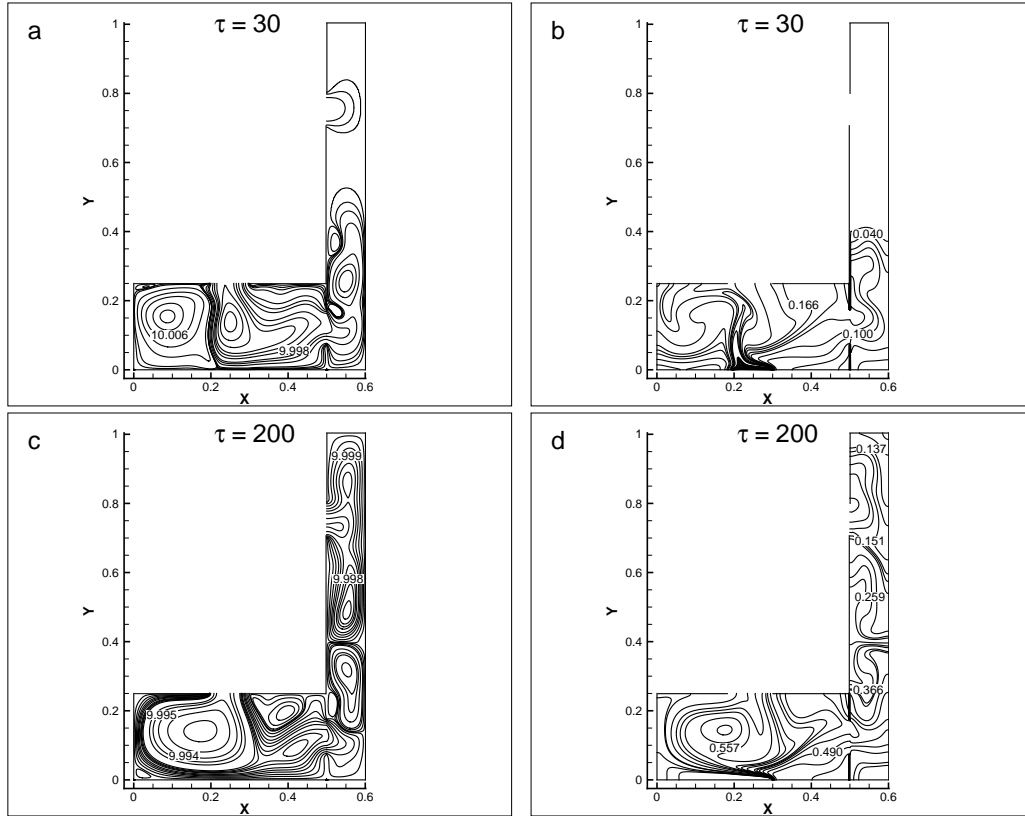


Figure 3.11: Stream function (a) and temperature contours (b) with ceiling vent in the compartment for $Gr = 10^{10}$.

3.4.4 Effect of ceiling vent in rectangular compartment

To know the effect of ceiling vent in rectangular compartment, stream function and temperature contours are plotted in Fig. 3.11 for Grashof number $Gr = 10^{10}$. The horizontal vent of width $D = 0.1H$ is positioned at the ceiling center of rectangular compartment and vertical vent of height $H_v = 0.1H$ connects the vertical shaft. The top left boundary of vertical shaft includes an exit port of height $H_v = 0.1H$ similar to the previous case. In Fig.3.11 (a), the stream function contours inside the compartment indicates significant entrainment of ambient fluid through the ceiling vent. As flow evolves, thermal plume spreads inside the compartment and significant amount of plume escapes through ceiling vent and the less quantity of hot fluid propagates into the vertical shaft and is shown in Fig.3.11 (b&d). Meanwhile along the axis of the plume, ambient fluid entrains through the ceiling vent and travels towards the heat source, leading to an excessive flow rotation and eventually an effective mixing of plume and fresh air is visualized inside the rectangular enclosure in Fig.3.11(c). The flow pattern in the shaft shows reduction in the intensity of thermal plume with fewer recirculating convective cells.

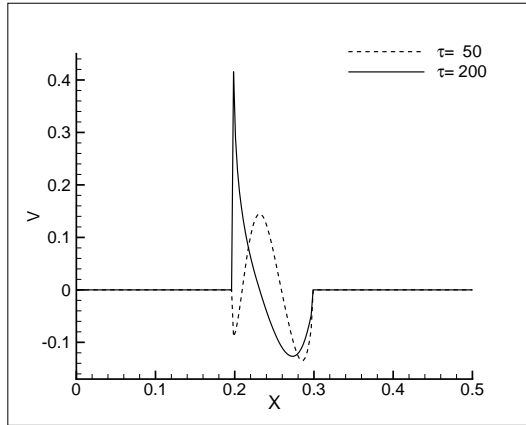


Figure 3.12: Non-dimensional normal velocity profile across the ceiling vent in rectangular compartment.

Figure 3.12 depicts the bidirectional normal velocity along the ceiling vent at different time intervals. The positive sign in the normal velocity indicates that plume leaves the compartment and negative sign indicates the inflow of ambient air.

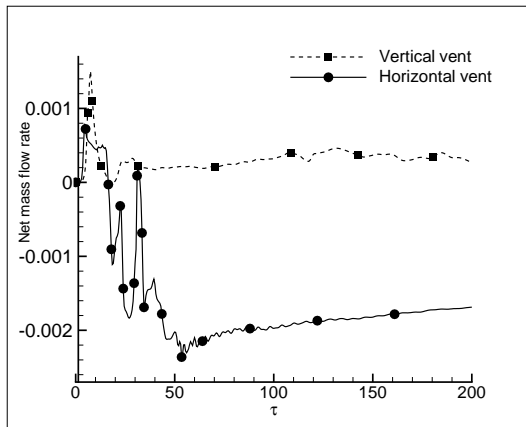


Figure 3.13: Non-dimensional net mass flow rate through vertical and horizontal vents in rectangular compartment.

To compare infiltration through openings in rectangular compartment, simulations are performed by replacing ceiling vent in previous case with vertical vent of height $H_v = 0.1H$ on the compartment left boundary. The evolution of net mass flow rate through left vertical vent and ceiling vent of compartment are compared in Fig. 3.13 for $Gr = 10^{10}$. The positive magnitudes in the plots indicates the infiltration through the vertical vent and plume outflow through the ceiling vent. Whereas the negative magnitudes represent the infiltration through ceiling vent and plume outflow through vertical vent. The infiltration rate through ceiling vent is very high when compared to vertical vent of the compartment.

3.4.5 Effect of rectangular compartment location

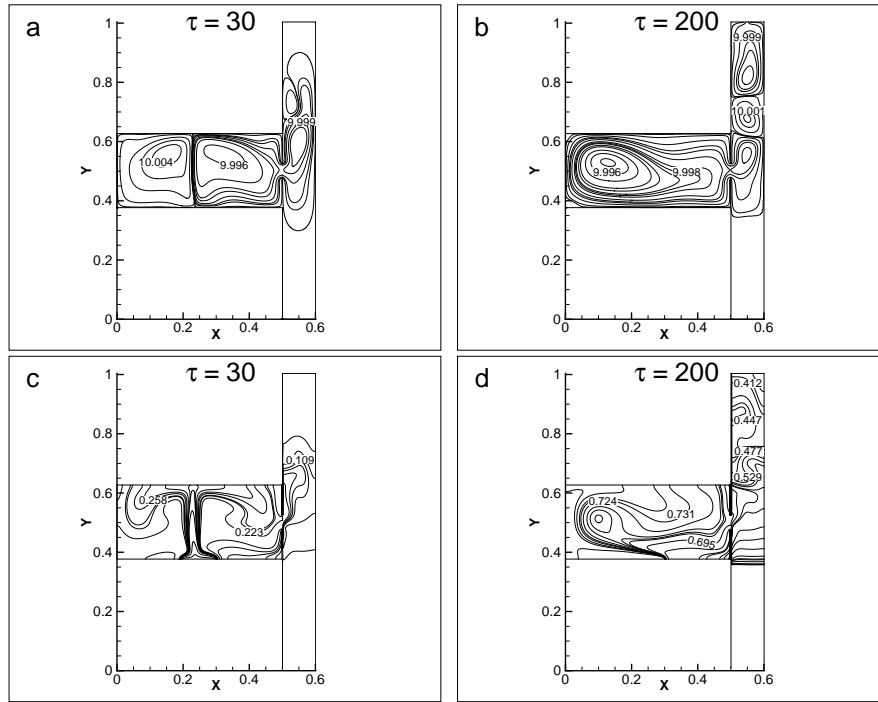


Figure 3.14: Stream function(a,b) and temperature(c,d) contours for shifted rectangular compartment.

To understand the plume behavior from upper floors, the rectangular compartment is placed at the mid-height of shaft and connected through vertical passage. The results are shown in Fig. 3.14 for $Gr = 10^{10}$. The height of the vertical passage is $0.05H$ and horizontal vent of size $0.05H$ is provided at the exit of shaft. The stream function contours are shown in Fig. 3.14 (a&b) and temperature contours are shown in (c&d). The plume enters the shaft and movement is significant towards the top portion of shaft. The buoyancy force drives thermal plume towards the shaft top exit. Moreover from Fig. 3.14 (d) it is visualized that temperature at the bottom portion of the shaft is at ambient temperature. The intensity of temperature contours at the upper half of the shaft is higher since the plume travel distance is reduced by shifting the compartment hence less recirculation cells are seen inside the shaft.

3.5 Summary

The turbulent buoyant flow characteristics in tall vertical shaft connected to adjacent rectangular compartment is numerically investigated. The flow patterns in

vertical shaft represents multi-recirculating convective cells with effective turbulent mixing due to buoyancy. The height of the vertical passage between the compartment and shaft has significant effect on growth and spread of plume. The infiltration rate through horizontal vent inside the compartment is higher than the vertical vent. The ceiling vent is preferred for effective removal of plume from the compartment. The plume transport phenomena is significantly changed by varying compartment location.

Chapter 4

Non-Boussinesq transition flows

4.1 Buoyant exchange flows between enclosures

In this chapter, buoyancy induced mixing between two square enclosures filled with hot and cold fluids and connected through central horizontal passage is numerically investigated. The lower and upper enclosures are filled with hot (T_h) and cold fluids (T_c) with heavier fluid lying on top of lighter fluid and buoyant exchange flows are modeled by non-Boussinesq approach.

4.1.1 Problem definition

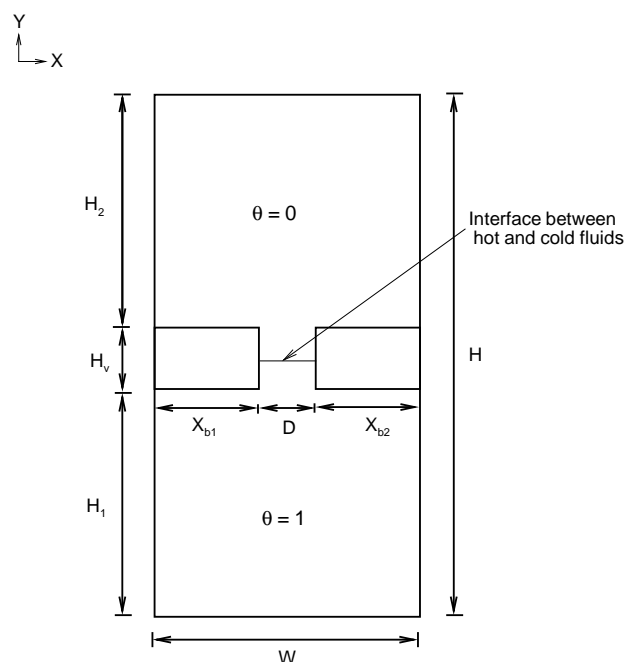


Figure 4.1: Schematic diagram of two square enclosures connected through horizontal vent.

The schematic diagram of two square enclosure is shown in Fig 4.1. A horizontal opening facilitates the buoyancy driven mixing process between the two enclosures. The width (W) of the enclosure is 0.45H. The height of lower and upper enclosure is $H_1=H_2=0.45H$. The vent height is $H_v= 0.1H$. The total height (H) of the enclosure is 1.0H. The height to width aspect ratio of lower (H_1/W) and upper enclosure (H_2/W) is 1.0. The value of H/W ratio is 2.22. The width of the horizontal passage is represented as D. A non-Boussinesq variable density approach is implemented to evaluate the density variations.

4.1.2 Governing equations

Most often flow problems involving change of temperature are modeled using Boussinesq approximation. However, for applications with large temperature difference Boussinesq approximation fails and results may not reflect the real phenomena. Hence, a pressure based algorithm with variable density approach is proposed to solve flow problems with larger temperature variation. The natural convection flow is modeled as unsteady, two-dimensional, laminar compressible flow problem suitable for low Mach number flows. The thermo physical properties of fluid are constant, except the change in density which are evaluated from ideal gas law. The governing equations for conservation of mass, momentum and energy are as follows:

Continuity equation

The continuity equation expressing the conservation of mass is

$$\frac{\partial \rho}{\partial t} + \frac{\partial(\rho u)}{\partial x} + \frac{\partial(\rho v)}{\partial y} = 0 \quad (4.1)$$

x-momentum equation

$$\frac{\partial(\rho u)}{\partial t} + \frac{\partial(\rho u u)}{\partial x} + \frac{\partial(\rho u v)}{\partial y} = -\frac{\partial(p - p_\infty)}{\partial x} + \frac{\partial}{\partial x} \left(2\mu \frac{\partial u}{\partial x} - \frac{2}{3}\mu \left[\frac{\partial u}{\partial x} + \frac{\partial v}{\partial y} \right] \right) + \frac{\partial}{\partial y} \left(\mu \left[\frac{\partial u}{\partial y} + \frac{\partial v}{\partial x} \right] \right) \quad (4.2)$$

y-momentum equation

$$\frac{\partial(\rho v)}{\partial t} + \frac{\partial(\rho u v)}{\partial x} + \frac{\partial(\rho v v)}{\partial y} = -\frac{\partial(p - p_\infty)}{\partial y} + \frac{\partial}{\partial x} \left(\mu \left[\frac{\partial u}{\partial y} + \frac{\partial v}{\partial x} \right] \right) + \frac{\partial}{\partial y} \left(2\mu \frac{\partial v}{\partial y} - \frac{2}{3}\mu \left[\frac{\partial u}{\partial x} + \frac{\partial v}{\partial y} \right] \right) - (\rho - \rho_\infty)g \quad (4.3)$$

where ρ is the density of the fluid; μ is the dynamic viscosity; g is the acceleration due to gravity.

Energy equation

$$\frac{\partial(\rho T)}{\partial t} + \frac{\partial(\rho u T)}{\partial x} + \frac{\partial(\rho v T)}{\partial y} = \frac{k}{C_p} \left[\frac{\partial^2 T}{\partial x^2} + \frac{\partial^2 T}{\partial y^2} \right] \quad (4.4)$$

where k is the thermal conductivity. The pressure work and viscous dissipation terms in energy equation are ignored for low Mach number flows.

The equation of state relates density with pressure and temperature and are as follows:

$$p = \rho R T \quad (4.5)$$

The pressure Poisson equation for variable density approach are derived as follows:

The continuity equation is modified and is given below:

$$\frac{\partial u}{\partial x} + \frac{\partial v}{\partial y} = -\frac{1}{\rho} \left(\frac{\partial \rho}{\partial t} + u \frac{\partial \rho}{\partial x} + v \frac{\partial \rho}{\partial y} \right) \quad (4.6)$$

The time discretized momentum equations are given as follows:

$$u^{n+1} = u^* - \frac{\Delta t}{\rho} \frac{\partial p}{\partial x} \quad (4.7)$$

$$v^{n+1} = v^* - \frac{\Delta t}{\rho} \frac{\partial p}{\partial y} \quad (4.8)$$

$$u^* = u^n + \Delta t \left[\frac{1}{\rho} \frac{\partial}{\partial x} \left(2\mu \frac{\partial u}{\partial x} - \frac{2}{3}\mu \left[\frac{\partial u}{\partial x} + \frac{\partial v}{\partial y} \right] \right) + \frac{1}{\rho} \frac{\partial}{\partial y} \left(\mu \left[\frac{\partial u}{\partial y} + \frac{\partial v}{\partial x} \right] \right) - u \frac{\partial u}{\partial x} - v \frac{\partial u}{\partial y} \right] \quad (4.9)$$

$$v^* = v^n + \Delta t \left[\frac{1}{\rho} \frac{\partial}{\partial x} \left(\mu \left[\frac{\partial u}{\partial y} + \frac{\partial v}{\partial x} \right] \right) + \frac{1}{\rho} \frac{\partial}{\partial y} \left(2\mu \frac{\partial v}{\partial y} - \frac{2}{3}\mu \left[\frac{\partial u}{\partial x} + \frac{\partial v}{\partial y} \right] \right) - \frac{(\rho - \rho_\infty)g}{\rho} - u \frac{\partial v}{\partial x} - v \frac{\partial v}{\partial y} \right] \quad (4.10)$$

where u^* & v^* are the predicted velocity fields. The pressure Poisson equation given

below is obtained by substituting equation (4.7&4.8) into L.H.S of eqn(4.6).

$$\nabla^2 p = \frac{\rho}{\Delta t} \left[\frac{\partial u^*}{\partial x} + \frac{\partial v^*}{\partial y} + \frac{1}{\rho} \left(\frac{\partial \rho}{\partial t} + u \frac{\partial \rho}{\partial x} + v \frac{\partial \rho}{\partial y} \right) \right] \quad (4.11)$$

where ρ, u, v are the density and velocity fields at time t^n .

The following non-dimensional variables are used to obtain the dimensionless governing equations:

The free convection velocity ($V_c = \sqrt{g\beta\Delta TH}$) is considered as the reference velocity scale. The height (H) of the enclosure is considered as the reference length scale.

$$X = \frac{x}{H}; Y = \frac{y}{H}; U = \frac{u}{V_c}; V = \frac{v}{V_c}; \tau = \frac{tV_c}{H}; \theta = \frac{T-T_c}{T_h-T_c}; V_c = (g\beta\Delta TH)^{\frac{1}{2}};$$

$$P = \frac{p-p_\infty}{\rho_\infty V_c^2}; \varrho = \frac{\rho}{\rho_\infty};$$

The dimensionless governing equations are as follows:

Non-dimensional continuity equation

$$\frac{\partial \varrho}{\partial \tau} + \frac{\partial(\varrho U)}{\partial X} + \frac{\partial(\varrho V)}{\partial Y} = 0 \quad (4.12)$$

Non-dimensional X-momentum equation

$$\frac{\partial(\varrho U)}{\partial \tau} + \frac{\partial(\varrho U U)}{\partial X} + \frac{\partial(\varrho U V)}{\partial Y} = -\frac{\partial P}{\partial X} + \frac{\partial}{\partial X} \left(\frac{2}{(Gr)^{\frac{1}{2}}} \frac{\partial U}{\partial X} - \frac{2}{3(Gr)^{\frac{1}{2}}} \left[\frac{\partial U}{\partial X} + \frac{\partial V}{\partial Y} \right] \right)$$

$$+ \frac{\partial}{\partial Y} \left(\frac{1}{(Gr)^{\frac{1}{2}}} \left[\frac{\partial U}{\partial Y} + \frac{\partial V}{\partial X} \right] \right) \quad (4.13)$$

Non-dimensional Y-momentum equation

$$\frac{\partial(\varrho V)}{\partial \tau} + \frac{\partial(\varrho U V)}{\partial X} + \frac{\partial(\varrho V V)}{\partial Y} = -\frac{\partial P}{\partial Y} + \frac{\partial}{\partial X} \left(\frac{1}{(Gr)^{\frac{1}{2}}} \left[\frac{\partial U}{\partial Y} + \frac{\partial V}{\partial X} \right] \right) +$$

$$\frac{\partial}{\partial Y} \left(\frac{2}{(Gr)^{\frac{1}{2}}} \frac{\partial V}{\partial Y} - \frac{2}{3(Gr)^{\frac{1}{2}}} \left[\frac{\partial U}{\partial X} + \frac{\partial V}{\partial Y} \right] \right) - \frac{(\varrho - 1)}{Ga} \quad (4.14)$$

Non-dimensional Energy equation

$$\frac{\partial(\varrho \theta)}{\partial \tau} + \frac{\partial(\varrho U \theta)}{\partial X} + \frac{\partial(\varrho v \theta)}{\partial Y} = \frac{1}{Pr(Gr)^{\frac{1}{2}}} \left[\frac{\partial^2 \theta}{\partial X^2} + \frac{\partial^2 \theta}{\partial Y^2} \right] \quad (4.15)$$

Where $Gr = \frac{g\beta\Delta TH^3}{\nu^2}$ is the Grashof number; $Pr = \frac{\nu}{\alpha}$ is the Prandtl number; $Ga = \beta\Delta T$ is the Gay-Lussac's number.

4.1.3 Boundary conditions

The solid walls are treated with adiabatic boundary conditions and no-slip boundary conditions are specified for velocity fields. At initial time $\tau = 0$, the lower enclosure and lower half of the horizontal passage are filled with hot fluid ($\theta = 1$), meanwhile the horizontal passage upper half and upper enclosure are filled with cold fluid ($\theta = 0$).

$$at \tau = 0 : U = V = 0 \quad (4.16)$$

$$Y = 0; Y = 1.0; 0 < X < 0.45 : U = V = \frac{\partial\theta}{\partial Y} = \frac{\partial P}{\partial Y} = 0 \quad (4.17)$$

$$X = 0; X = 0.45; 0 < Y < 1.0 : U = V = \frac{\partial\theta}{\partial X} = \frac{\partial P}{\partial X} = 0 \quad (4.18)$$

$$Y = \frac{H_1}{H}; 0 < X < \frac{X_{b1}}{H}; \frac{X_{b1}}{H} + \frac{D}{H} < X < \frac{X_{b2}}{H} : U = V = \frac{\partial\theta}{\partial Y} = \frac{\partial P}{\partial Y} = 0 \quad (4.19)$$

$$Y = \frac{H_1}{H} + \frac{H_v}{H}; 0 < X < \frac{X_{b1}}{H}; \frac{X_{b1}}{H} + \frac{D}{H} < X < \frac{X_{b2}}{H} : U = V = \frac{\partial\theta}{\partial Y} = \frac{\partial P}{\partial Y} = 0 \quad (4.20)$$

$$X = \frac{X_{b1}}{H}; \frac{H_1}{H} < Y < \frac{H_v}{H}; U = V = \frac{\partial\theta}{\partial X} = \frac{\partial P}{\partial X} = 0 \quad (4.21)$$

$$X = \frac{X_{b1}}{H} + \frac{D}{H}; \frac{H_1}{H} < Y < \frac{H_v}{H}; U = V = \frac{\partial\theta}{\partial X} = \frac{\partial P}{\partial X} = 0 \quad (4.22)$$

4.1.4 Numerical Procedure

The governing equations are discretized using finite difference technique and the solver is developed in Fortran 90. The Simplified Marker and Cell (SMAC) algorithm is used to solve the governing equations on collocated grid and the algorithm is given below

- Set initial conditions for U,V,P and θ .
- Predictor step: Calculate the predicted velocity fields U^* and V^* by dropping pressure term from momentum equations.
- Solve pressure Poisson equation along with equation of state.
- Corrector step: Calculate the updated values of velocity fields U^{n+1} and V^{n+1} .
- Solve the temperature equation.
- Calculate density from equation of state.

- Check for convergence.

Rhie-Chow momentum interpolation technique is used to avoid pressure velocity decoupling on non staggered grid. The diffusion terms are discretized using second order central finite difference schemes and the non-linear convective terms are evaluated using high accuracy compact schemes. A Bi-conjugate gradient algorithm is used to solve the pressure Poisson equation and the convergence criteria is set to $\leq 10^{-6}$. A small time step of $\Delta\tau = 10^{-4}$ is used to avoid numerical instability. To reduce the round off errors, all simulations are performed with double precision accuracy. Time integration is performed by four stages Runge-Kutta (RK-4) method.

4.1.5 Grid Independence

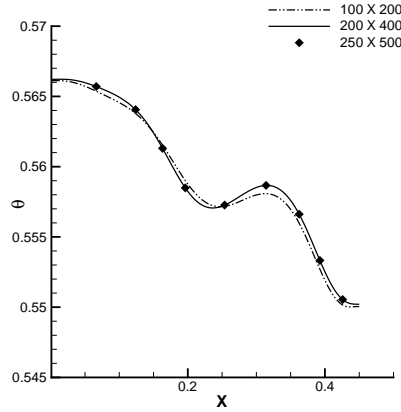


Figure 4.2: Grid independence: Temperature profile at the mid-height of lower enclosure.

The grid sensitivity tests are performed with three different mesh sizes to ensure that numerical solutions are independent with the chosen grid system. Figure 4.2 illustrates the variation of temperature profile along the horizontal wall at the center of lower enclosure for three different mesh sizes 100×200 , 200×400 , 250×500 and Grashof number is 5×10^7 . It is observed that the deviations in temperature profiles computed with grid size of 200×400 and 250×500 are insignificant and numerical solution is grid independent with a mesh size of 200×400 . Hence all simulations are performed with grid size of 200×400 .

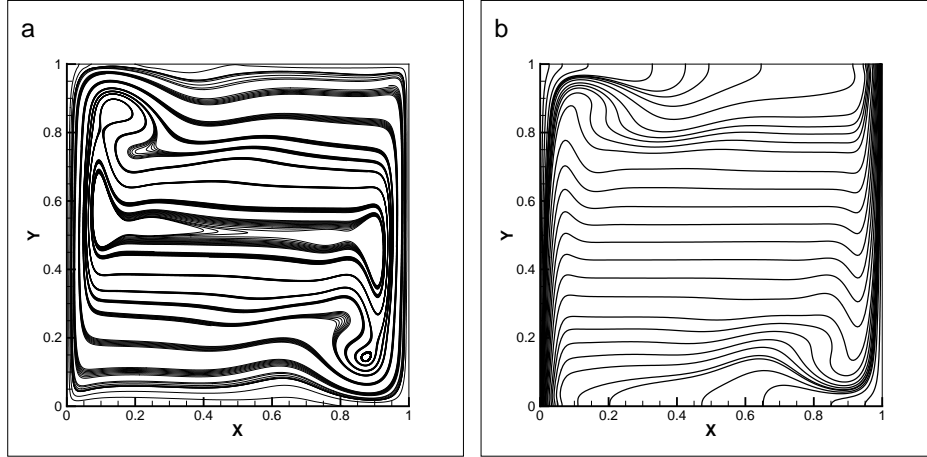


Figure 4.3: (a) Stream function and (b) temperature contours for $Ra = 10^7$

4.1.6 Validation

The mathematical model and accuracy of numerical method has been validated with the numerical results in literature [102, 103]. The buoyancy driven flow in differentially heated square cavity was analyzed and results were obtained under non-Boussinesq approximation for $Ra = 10^7$ by finite element [103] formulation. The Rayleigh number is the product of Grashof number and Prandtl number. The Prandtl number for air is taken as 0.72. The stream function and temperature contours shown in Fig. 4.3 for $Ra = 10^7$ are validated with the existing numerical results [103]. The present results shown in Fig. 4.3 are simulated by finite difference method, while benchmark results were simulated by finite element method. The deviations between the two results are due to difference in numerical methods (discretization schemes and solution technique).

Table 4.1 summarizes the quantitative comparison of average Nusselt number variations with the numerical results of [102, 103] for two different Rayleigh numbers $Ra = 10^6, 10^7$. It is noticed that the present numerical method with compact schemes are closer to the computed numerical results in literature.

Table 4.1: Average Nusselt number on the heated wall

Rayleigh Number	Present	Vierendeels et al. [102]	Becker and Braack [103]
10^6	8.714	8.6866	8.8597
10^7	16.305	16.241	16.2412

4.1.7 Results and discussions

The results are presented by varying different Grashof numbers and the critical Grashof number above which flow instabilities develop across the vent are

determined. The effects of vent aspect ratio on flow characteristics are studied by varying vent width and thickness.

4.1.7.1 Evolution of flow characteristics for $Gr = 10^7$

To understand the flow behavior with time, evolution of stream function and density contours are shown in Fig. 4.4-4.6 for $Gr = 10^7$. The vent aspect ratio is 1 ($D=0.1H, H_v = 0.1H$). The illustrations shown in Fig. 4.4 & 4.5 depicts the evolution of stream function patterns. During initial time $\tau = 0$ both fluids are at rest, as flow progresses at time $\tau = 2$ two convective cells are formed on either side of the vent. A density difference arises between the lighter and heavier fluids across the vent. The buoyancy force drives hot fluid from lower enclosure to propagate into upper enclosure. Meanwhile cold fluid penetrates into lower enclosure and vortex pattern is observed across the vent at time $\tau = 20$. The mixing process between fluids leads to the formation of vortex pattern. The vortex across horizontal passage is visualized between time intervals $\tau = 20 - 40$, until bidirectional exchange destroys the vortex structure at time $\tau = 50$. In upper enclosure, convective cell symmetry pattern is broken at time $\tau \geq 50$. Significant quantity of hot fluid propagates into upper enclosure between time intervals $\tau = 50 - 70$. In Fig. 4.5, vortex structure reappears at time $\tau = 80$, creates flow resistance across the vent and is sustained for longer duration till $\tau = 100$. Meanwhile, thermal gradients weaken inside the upper enclosure, two convective cells merges to form unicellular pattern. The subsequent destruction of vortex across the vent occurs at time $\tau = 110$. The cyclic formation of vortex structure across the horizontal passage stops at time $\tau > 100$. Flow resistance develops across the passage between time intervals $\tau = 150 - 200$. The buoyancy force assists the strong thermal gradients inside lower enclosure to prolong for longer duration. Hence merging of convective cells does not happen in lower enclosure with hot fluid.

Figure 4.6 represents the evolution of density contours. Two mushroom shaped plumes are formed on either side of horizontal vent at time $\tau = 5$, and it reaches the upper and lower enclosure horizontal boundaries at time $\tau = 20$. The temperature difference between fluids accelerates the mixing process and plume gains momentum to spread inside the enclosures. As plume migrates further inside the enclosure, plume width increases due to entrainment of surrounding fluid. The flow through horizontal passage is bidirectional. The hot fluid leaves through left half of the vent and cold fluid enters through right half. Since cold fluid leaves from right portion of

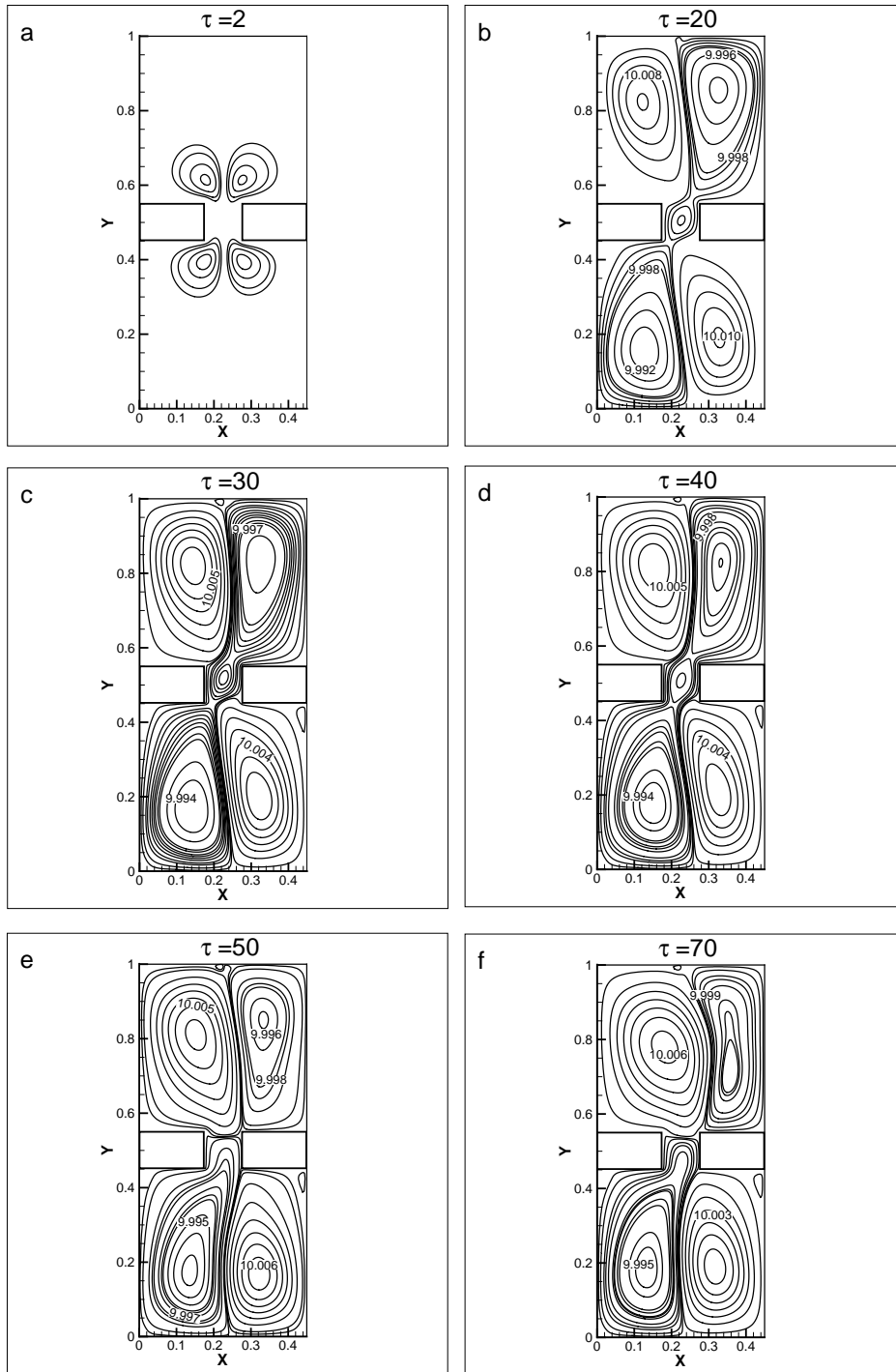


Figure 4.4: Evolution of stream function contours for $Gr = 10^7$ between time intervals $\tau = 2 - 70$.

upper enclosure, propagating hot fluid penetrates further towards right half and loses its momentum by impinging on right wall. Hence the thermal plume tilts towards side wall at time $\tau = 100$. As time evolves there is significant rise in buoyancy driven exchange between the enclosures.

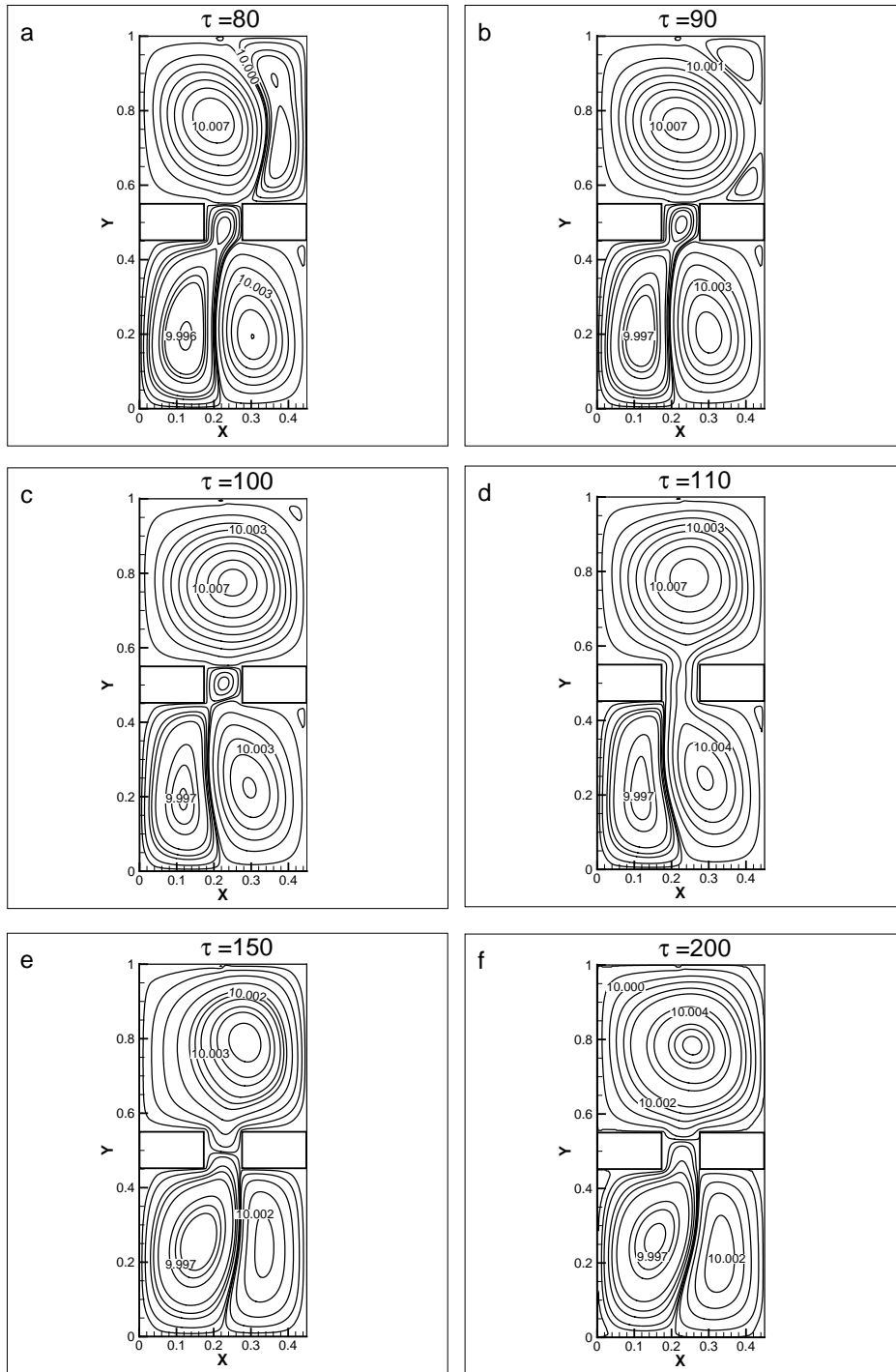


Figure 4.5: Evolution of stream function contours for $Gr = 10^7$ between time intervals $\tau = 80 - 200$.

Figures 4.7(a&b) indicates variation of density profiles along horizontal wall at the center of lower and upper enclosure for different time intervals. It is evident that as time progresses, flow rates through vent increases. The heavier fluid from upper

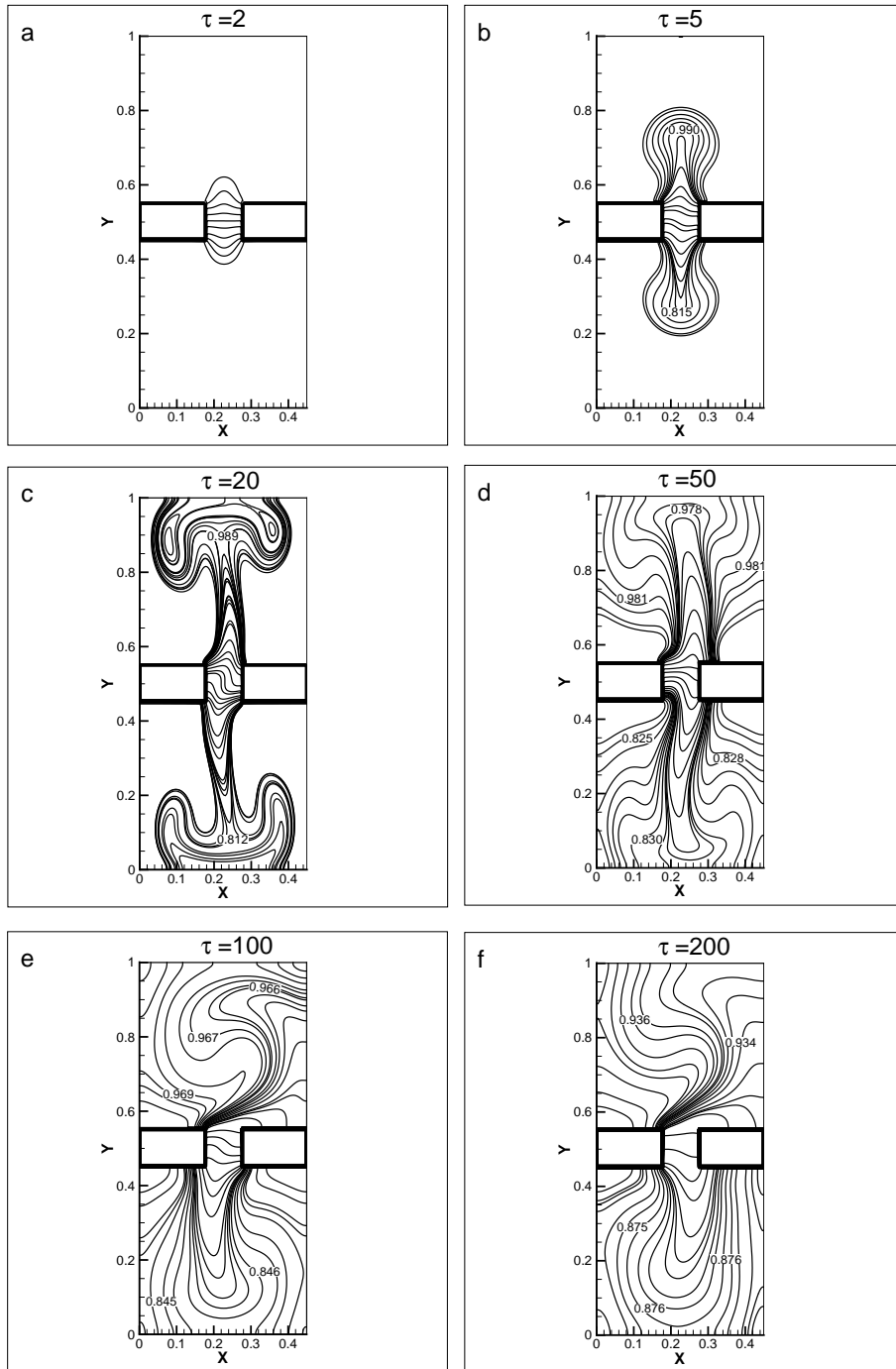


Figure 4.6: Evolution of density contours for $Gr = 10^7$.

enclosure enters into lower enclosure meanwhile lighter fluid propagates into upper enclosure. Hence as time advances, there is step increase and decrease of density magnitudes in the lower and upper enclosures.

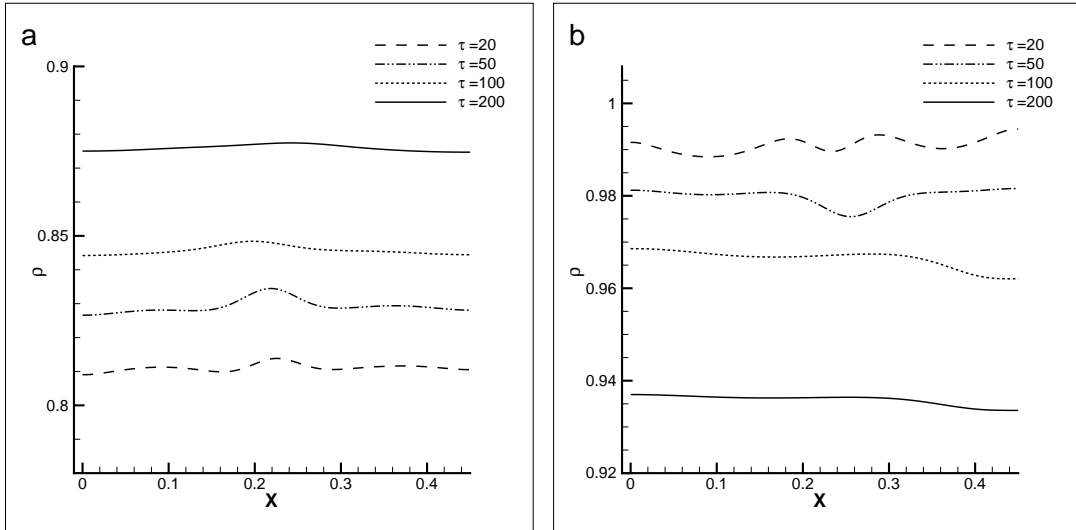


Figure 4.7: (a&b) Density profile at mid-height of lower and upper enclosure for $Gr = 10^7$.

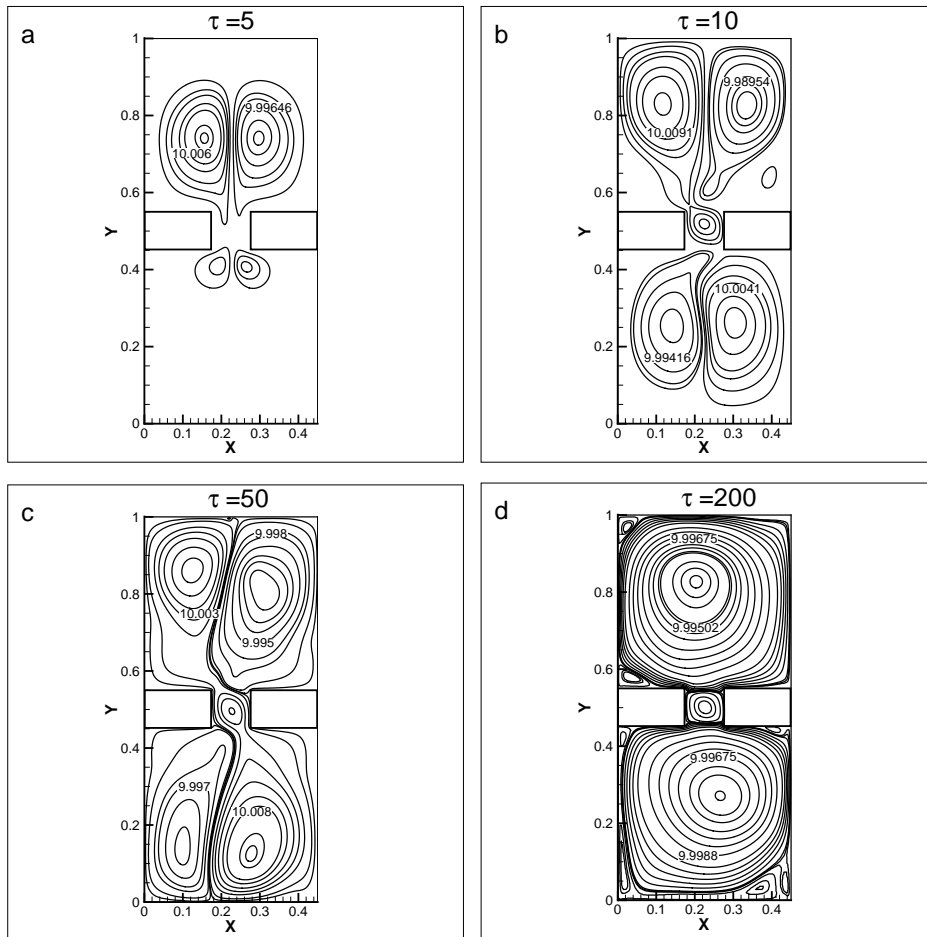


Figure 4.8: Evolution of stream function contours for $Gr = 5 \times 10^7$.

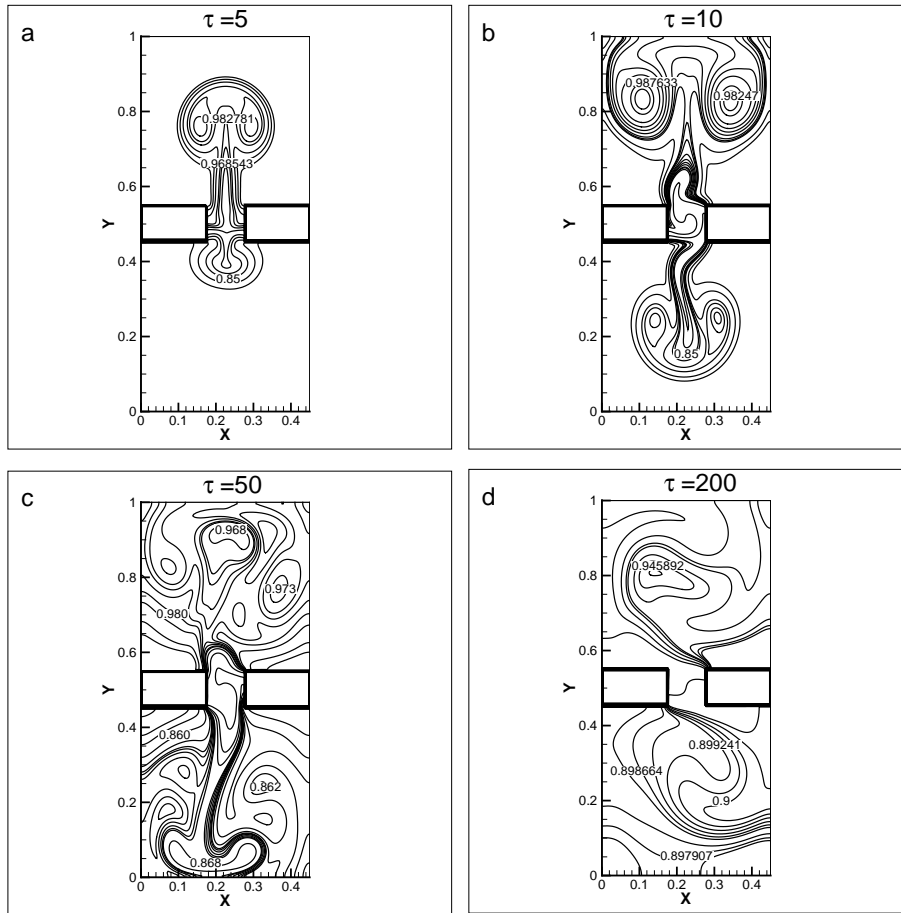


Figure 4.9: Evolution of density contours for $Gr = 5 \times 10^7$.

4.1.7.2 Effect of Grashof number

The illustrations shown in Fig. 4.8&4.9 represents the stream function and density contours for $Gr = 5 \times 10^7$. From stream function contours in Figure 4.8, at initial time $\tau = 5$, size of two convective cells developed inside upper enclosure are larger than lower enclosure. As Grashof number increases buoyancy force dominates viscous force and bulk amount of hot fluid propagates into upper enclosure. The higher Grashof number develops flow instabilities and symmetry in stream function pattern disappears during early evolution stage. There is substantial rise in bidirectional exchange between enclosures which are evident from the intense recirculation patterns at time $\tau = 10$ &50. As flow evolves, convective cells expands thereby interactions between hot and cold fluids increases. The single unified convective cell developed inside upper and lower enclosures at time $\tau = 200$ indicates that at higher Grashof number mixing rates through ceiling vent increases.

The density contours in Fig. 4.9 indicates that at time $\tau = 5$, buoyancy force

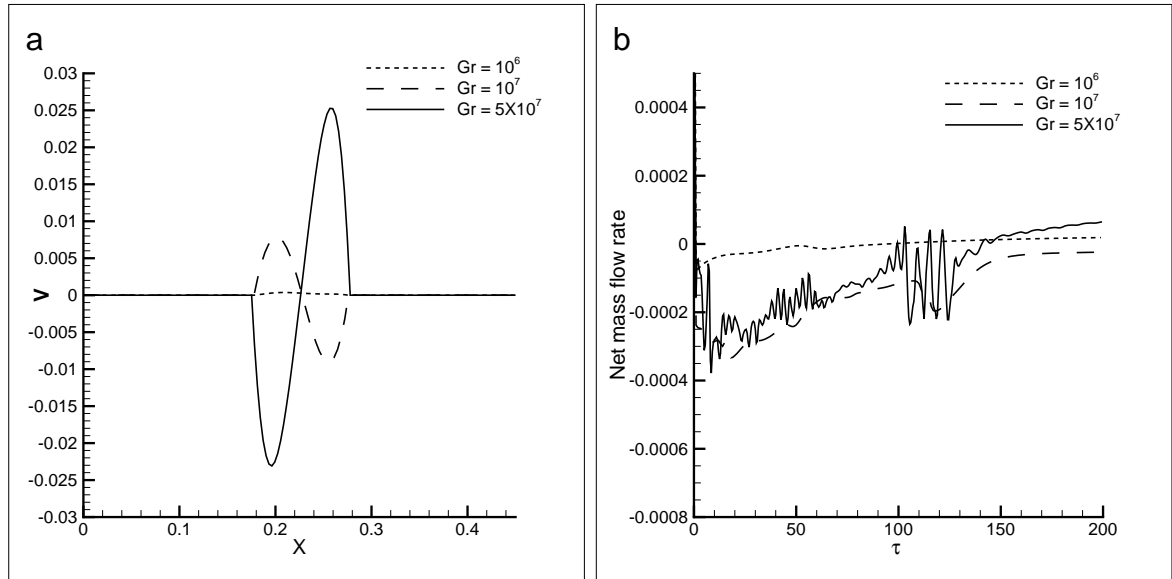


Figure 4.10: (a) Comparison of normal velocity profile for different Gr; (b) Comparison of net mass flow rate for different Gr.

accelerates the plume developed from lighter fluid towards upper compartment, while growth of entrainment plume is delayed. The plume reaches enclosure ceiling at early time $\tau \leq 10$ and two asymmetric plumes are seen propagating in opposite directions. The plume momentum from hot fluid is higher than denser plume. With increase in thermal buoyancy and instabilities, flow characteristics are highly unstable and complex at time $\tau = 50$. The volume flow rates through vent increases and mixing of fluids leads to the formation of recirculation patterns inside the enclosures. As flow progresses, well mixed environment is visualized in enclosures, the plume acceleration reduces and inclines towards the sidewalls.

A comparison of normal velocity profile and net mass flow rate through horizontal vent are shown in Fig. 4.10(a&b) for different Grashof numbers. In Fig. 4.10(a) normal velocity profiles across the vent are plotted at $\tau = 200$. For $Gr = 10^6$, velocity magnitudes are very small when compared with higher Gr. For $Gr = 10^7$, hot and cold fluids are transferred through left and right portion of horizontal vent, while opposite trend is observed for $Gr = 5 \times 10^7$. For $Gr = 10^6$, net mass flow rate through vent is close to zero since equal amount of hot and cold fluids are exchanged through vent. However when Gr is increased to 5×10^7 , flow becomes unstable and oscillations are developed due to instabilities. The negative magnitudes implies imbalance between hot and cold fluid volume flow rates. However at later time $\tau \geq 150$, oscillations are damped out and system attains equilibrium by attaining quasi-steady state. The critical Grashof number is

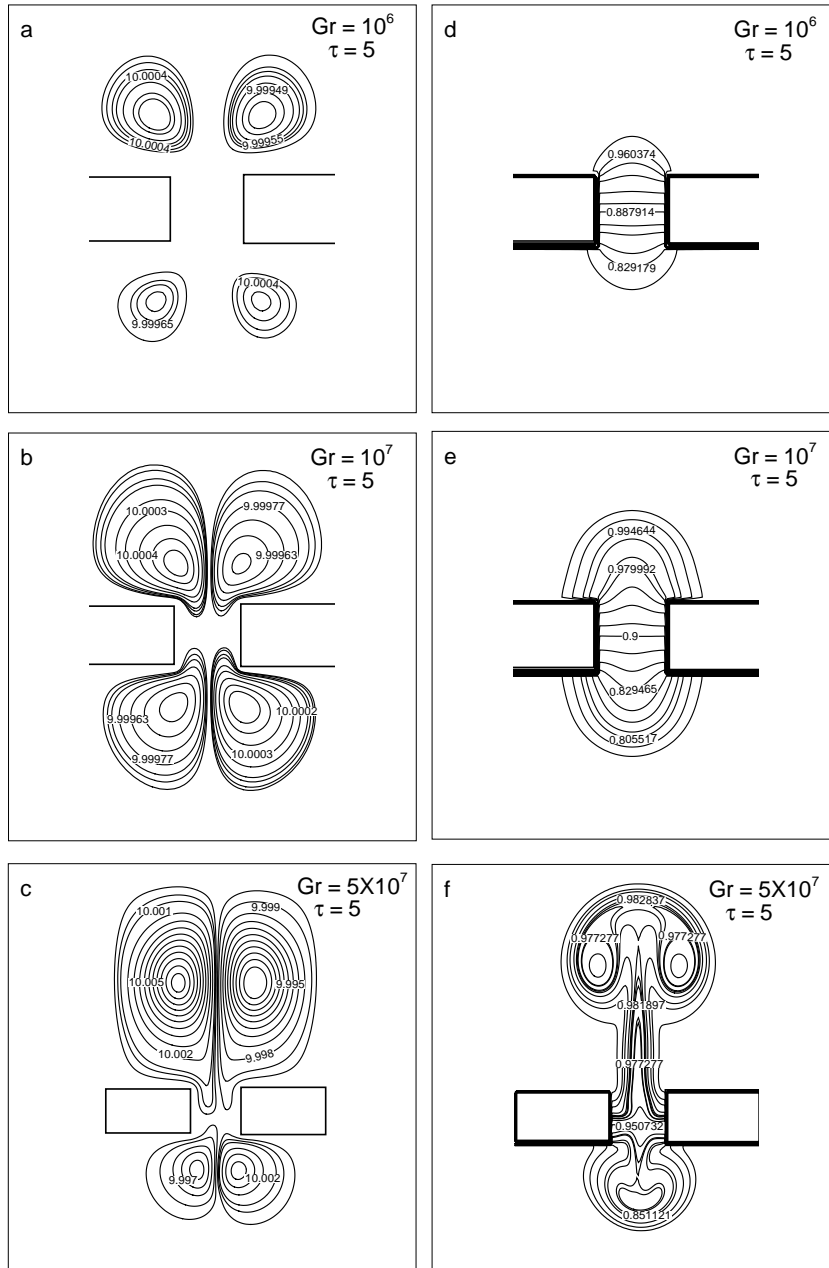


Figure 4.11: (a-c) Comparison of stream function contours for different Gr; (d-f) Comparison of density contours for different Gr.

$Gr = 10^7$ beyond which flow becomes chaotic due to instability. This intensifies the oscillation frequency. The initial instability patterns developed near horizontal passage are shown in Fig. 4.11 by comparing stream function (a-c) and density contours (d-f) for different Grashof numbers. It is evident that with rise in Grashof number, thermal buoyancy force dominates the flow and unstable flow patterns are seen evolving on either side of horizontal passage.

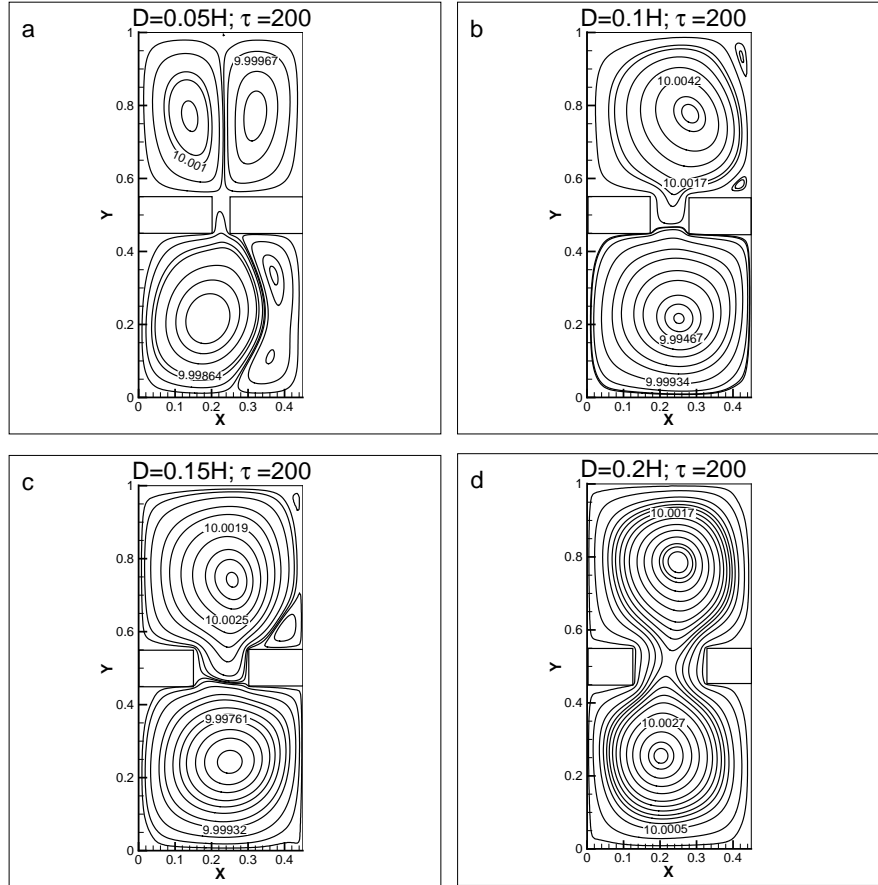


Figure 4.12: Stream function contours for different vent widths $Gr = 2.5 \times 10^7$.

4.1.7.3 Effect of vent width

Figures 4.12&4.13 indicates the stream function and temperature contours for different vent widths $D=0.05H$, $0.1H$, $0.15H$ & $0.2H$. The vent thickness is fixed as $0.1H$ for all cases. The results are shown at time $\tau = 200$ for Grashof number 2.5×10^7 . The stream line patterns for vent width $0.05H$ depicts evolution of pair of convective cells inside enclosures and merging of primary and secondary cells are delayed. This implies that volume flow rates through vent decreases with reduction in vent width. However with increase in vent width ($0.1H$ & $0.15H$), bidirectional exchange rate increases and pair of well mixed larger convective cells are visualized from the stream function contours. The flow resistance between lighter and denser fluids are seen developing across the horizontal passage. For vent width $D=0.2H$, flow resistance decreases and mixing rates between enclosures increases. From temperature contours in Fig. 4.13, for vent width $D=0.05H$, axisymmetric plume pattern is retained inside upper enclosure. This is due to decline in flow rate across the vent. With rise in vent widths, bulk quantity of hot fluid propagates into upper

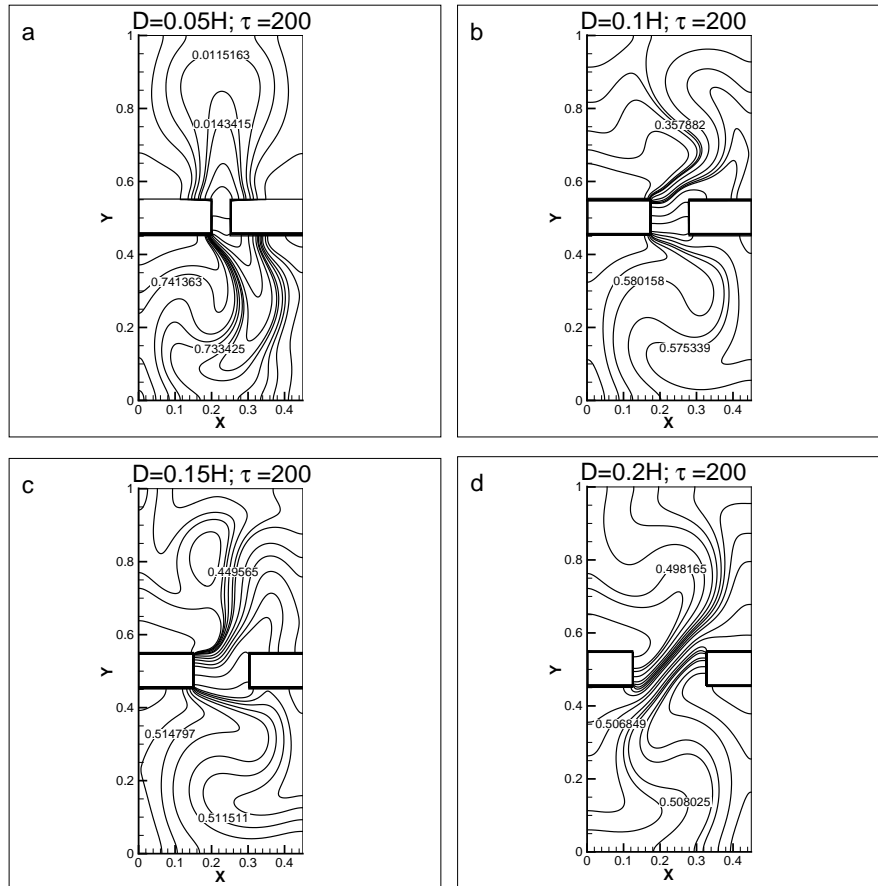


Figure 4.13: Temperature contours for different vent widths $Gr = 2.5 \times 10^7$

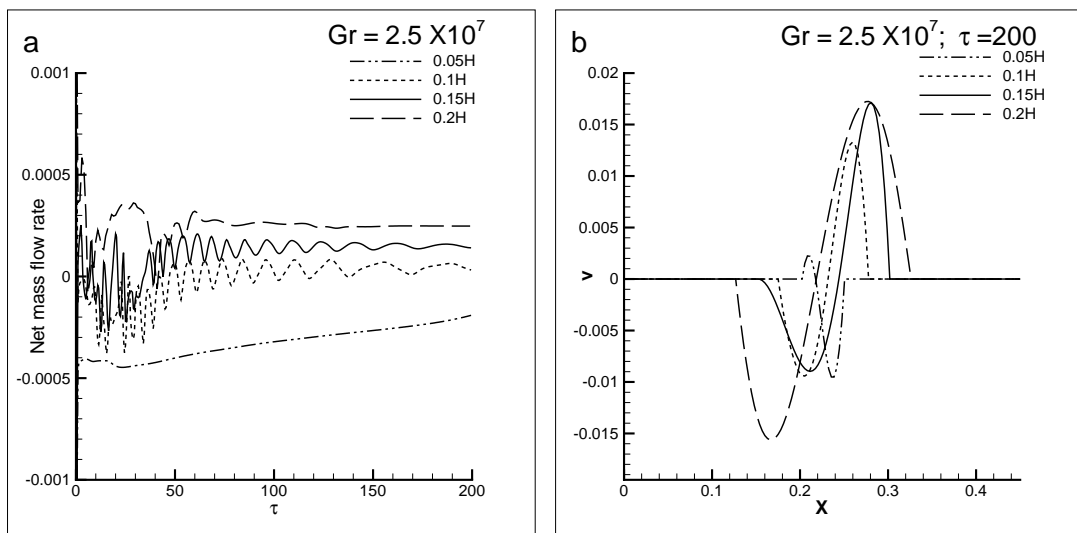


Figure 4.14: (a) Comparison of net mass flow rate for different vent widths; (b) Comparison of normal velocity profiles for different vent widths

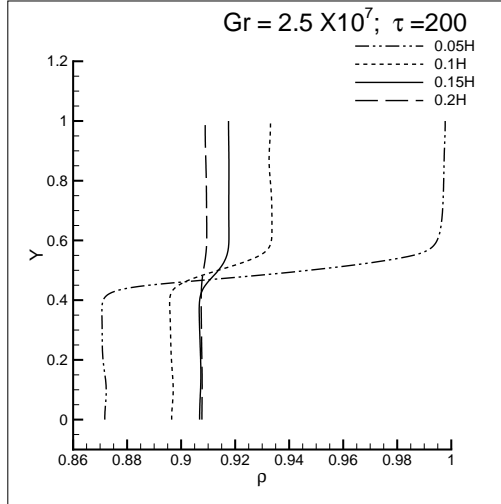


Figure 4.15: Density variation along the vertical axis for different vent size $Gr = 2.5 \times 10^7$

enclosure, meanwhile entrained cold air diffuses the heat inside lower enclosure. Hence for different vent widths, temperature magnitudes substantially rises and drops inside the upper and lower enclosures. The vent width $D=0.2H$ reduces thermal blockage across the vent and facilitates bidirectional diagonal exchange between the enclosures.

Figure 4.14(a) represents the net mass flow rate through the vent for different vent widths. For $D=0.05H$, stable flow behavior is observed across the vent. However higher vent widths results in the growth of instabilities and unstable oscillations evolves till the system reaches quasi-steady state. It is noticed that the frequency of oscillations increases till $D \leq 0.15$. The higher vent width $D=0.2H$ reduces instability patterns and promotes a balanced flow across the opening. The variation of normal velocity profiles are shown in Figure 4.14(b). The volume flow rate and velocity magnitudes increases for larger vent widths. Figure 4.15 shows the variation of density profiles along the central vertical axis of computational domain. It is noticed that for higher vent widths, density magnitudes increases inside lower enclosure, while opposite trend is observed inside the upper enclosure.

4.1.7.4 Effect of vent thickness

Figure 4.16 indicates the evolution of stream function contours for case without vent thickness ($H_v = 0$). The vent width is fixed as $D=0.1H$ and Grashof number is 10^7 . It is evident that as thickness of vertical passage reduces the interactions between enclosure increases. This is shown in the stream function contours at time $\tau = 50$.

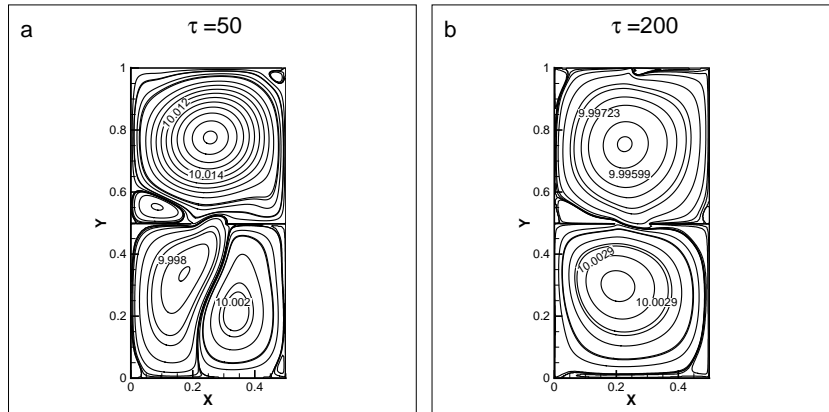


Figure 4.16: Stream function contours for zero vent thickness; $Gr = 10^7$.

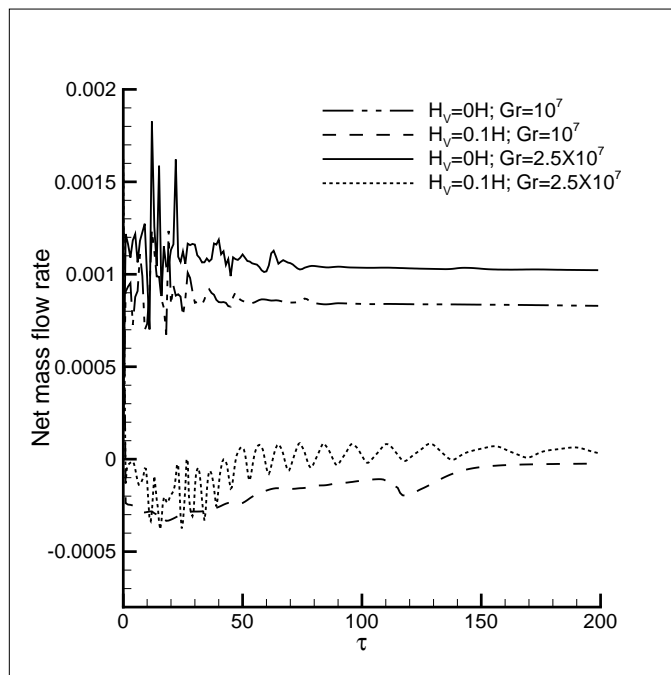


Figure 4.17: Comparison of net mass flow rate for different vent thickness and Grashof number.

Moreover unification of primary and secondary convective cells are seen in two enclosures at time $\tau = 200$. A comparison of net mass flow rate across the vent are shown in Figure 4.17 for cases with and without vent thickness. It is observed that flow perturbations increases with reduction in vent thickness and nonlinear interactions are significant for higher Grashof numbers.

4.2 Summary

The buoyancy driven flow characteristics between two square enclosures connected through central horizontal passage is numerically studied. The bidirectional flow exchanges between the enclosures are investigated by varying the vent aspect ratio. The results are presented for different Grashof numbers. The critical Grashof number is identified as 10^7 and further rise in Gr induces flow instabilities. A substantial rise in volume flow rates across the vent are observed for higher Grashof numbers and flow characteristics are highly unstable and complex inside the enclosures. With reduction in vent width from $D=0.1H$ to $0.05H$, less quantity of hot and cold fluids are exchanged and hence flow behavior is stable. However vent width $0.1H \leq D \leq 0.15H$ promotes flow disturbances and nonlinear oscillations are seen developing across the vent. The higher vent width $D=0.2H$ reduces flow perturbations and facilitates balanced flow across the vent. Reduction in vent thickness results in early unification of convective cells and frequency of oscillations increases aiding better mixing rates between the enclosures.

Chapter 5

Non-Boussinesq turbulent buoyant flows

In this chapter, turbulent combined convection flow in ceiling vented square enclosure with forced inlet port is numerically investigated. The plume behavior and discharge rate through ceiling vent are analyzed by supplying forced air through the inlet port. The present model is valid when the buoyancy effects are significant in comparison with forced convection effects. A turbulent non-Boussinesq variable density approach is implemented to evaluate the density variations.

5.1 Problem definition

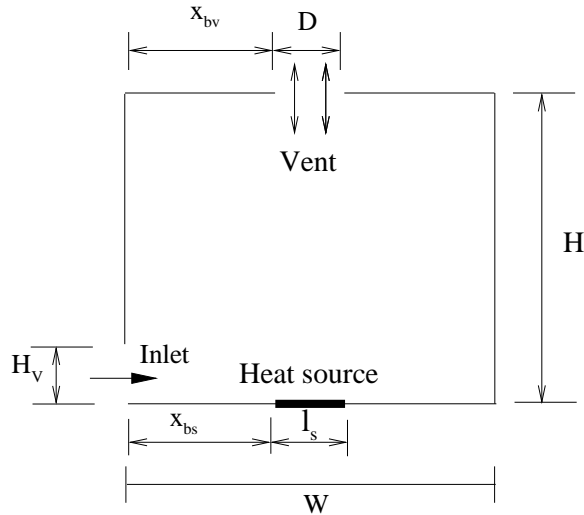


Figure 5.1: Schematic diagram of rectangular compartment connected to vertical shaft

Figure 5.1 represents the schematic diagram of square enclosure with ceiling vent and inlet port. There is a finite size heat source of constant wall temperature T_s

located at the bottom wall of enclosure. A horizontal vent of width D is opened to the ambient media and inlet port of height H_v facilitates the entry of forced air stream into the square enclosure.

5.2 Governing equations

The turbulent combined convection flow is modeled as unsteady, two-dimensional, compressible flow problem suitable for low Mach number flows. The thermo-physical properties of fluid are constant, except the change in density that are evaluated from ideal gas law. The governing equations comprise the Favre averaged Navier Stokes equation with turbulence modeled by buoyancy modified Lam-Bremhorst low Reynolds number $k - \varepsilon$ model.

The following non-dimensional variables are used to obtain the dimensionless governing equations:

The free convection velocity ($V_c = \sqrt{g\beta\Delta TH}$) is considered as the reference velocity scale. $X = \frac{x}{H}$; $Y = \frac{y}{H}$; $U = \frac{u}{V_c}$; $V = \frac{v}{V_c}$; $\tau = \frac{tV_c}{H}$; $\theta = \frac{T-T_\infty}{T_s-T_\infty}$; $V_c = (g\beta\Delta TH)^{\frac{1}{2}}$; $P = \frac{p-p_\infty}{\rho_\infty V_c^2}$; $\varrho = \frac{\rho}{\rho_\infty}$; $K = \frac{k}{(g\beta\Delta TH)}$; $\varepsilon = \frac{\epsilon}{((g\beta\Delta T)^3 H)^{\frac{1}{2}}}$

The non-dimensional form of governing equations are as follows:

$$\frac{\partial \varrho}{\partial \tau} + \frac{\partial(\varrho U)}{\partial X} + \frac{\partial(\varrho V)}{\partial Y} = 0 \quad (5.1)$$

$$\begin{aligned} \frac{\partial(\varrho U)}{\partial \tau} + \frac{\partial(\varrho U U)}{\partial X} + \frac{\partial(\varrho U V)}{\partial Y} = & -\frac{\partial P}{\partial X} + \frac{\partial}{\partial X} \left(\frac{2}{(Gr)^{\frac{1}{2}}} \frac{\partial U}{\partial X} - \frac{2}{3(Gr)^{\frac{1}{2}}} \left[\frac{\partial U}{\partial X} + \frac{\partial V}{\partial Y} \right] \right) \\ & + \frac{\partial}{\partial Y} \left(\frac{1}{(Gr)^{\frac{1}{2}}} \left[\frac{\partial U}{\partial Y} + \frac{\partial V}{\partial X} \right] \right) + 2 \frac{\partial}{\partial X} \left[\frac{1}{Re_t} \frac{\partial U}{\partial X} \right] + \frac{\partial}{\partial Y} \left[\frac{1}{Re_t} \frac{\partial U}{\partial Y} \right] + \frac{\partial}{\partial Y} \left[\frac{1}{Re_t} \frac{\partial V}{\partial X} \right] \end{aligned} \quad (5.2)$$

$$\begin{aligned} \frac{\partial(\varrho V)}{\partial \tau} + \frac{\partial(\varrho U V)}{\partial X} + \frac{\partial(\rho V V)}{\partial Y} = & -\frac{\partial P}{\partial Y} + \frac{\partial}{\partial X} \left(\frac{1}{(Gr)^{\frac{1}{2}}} \left[\frac{\partial U}{\partial Y} + \frac{\partial V}{\partial X} \right] \right) - \frac{(\rho - 1)}{Ga} \\ & + \frac{\partial}{\partial Y} \left(\frac{2}{(Gr)^{\frac{1}{2}}} \frac{\partial V}{\partial Y} - \frac{2}{3(Gr)^{\frac{1}{2}}} \left[\frac{\partial U}{\partial X} + \frac{\partial V}{\partial Y} \right] \right) + \frac{\partial}{\partial X} \left[\frac{1}{Re_t} \frac{\partial U}{\partial Y} \right] \\ & + \frac{\partial}{\partial X} \left[\frac{1}{Re_t} \frac{\partial V}{\partial X} \right] + 2 \frac{\partial}{\partial Y} \left[\frac{1}{Re_t} \frac{\partial V}{\partial Y} \right] \end{aligned} \quad (5.3)$$

$$\frac{\partial(\varrho \theta)}{\partial \tau} + \frac{\partial(\varrho U \theta)}{\partial X} + \frac{\partial(\rho V \theta)}{\partial Y} = \frac{\partial}{\partial X} \left[\left(\frac{1}{(Pr(Gr)^{\frac{1}{2}}} + \frac{1}{Pr_t Re_t} \right) \frac{\partial \theta}{\partial X} \right] + \frac{\partial}{\partial Y} \left[\left(\frac{1}{(Pr(Gr)^{\frac{1}{2}}} + \frac{1}{Pr_t Re_t} \right) \frac{\partial \theta}{\partial Y} \right] \quad (5.4)$$

$$\begin{aligned} \frac{\partial(\rho K)}{\partial \tau} + \frac{\partial(\rho U K)}{\partial X} + \frac{\partial(\rho V K)}{\partial Y} &= \frac{\partial}{\partial X} \left[\left(\frac{1}{(Gr)^{\frac{1}{2}}} + \frac{1}{\sigma_k Re_t} \right) \frac{\partial K}{\partial X} \right] + \frac{\partial}{\partial Y} \left[\left(\frac{1}{(Gr)^{\frac{1}{2}}} + \frac{1}{\sigma_k Re_t} \right) \frac{\partial K}{\partial Y} \right] \\ &\quad - \frac{1}{Re_t \sigma_t} \frac{\partial \rho}{\partial Y} - \varepsilon + \frac{1}{Re_t} \left[2 \left(\frac{\partial U}{\partial X} \right)^2 + 2 \left(\frac{\partial V}{\partial Y} \right)^2 + \left(\frac{\partial U}{\partial Y} + \frac{\partial V}{\partial X} \right)^2 \right] \end{aligned} \quad (5.5)$$

$$\begin{aligned} \frac{\partial(\rho \varepsilon)}{\partial \tau} + \frac{\partial(\rho U \varepsilon)}{\partial X} + \frac{\partial(\rho V \varepsilon)}{\partial Y} &= \frac{\partial}{\partial X} \left[\left(\frac{1}{(Gr)^{\frac{1}{2}}} + \frac{1}{\sigma_\varepsilon Re_t} \right) \frac{\partial \varepsilon}{\partial X} \right] + \frac{\partial}{\partial Y} \left[\left(\frac{1}{(Gr)^{\frac{1}{2}}} + \frac{1}{\sigma_\varepsilon Re_t} \right) \frac{\partial \varepsilon}{\partial Y} \right] \\ &\quad - C_{2\varepsilon} f_2 \frac{\varepsilon^2}{k} C_{1\varepsilon} f_1 \left[\frac{1}{Re_t} \left\{ 2 \left(\frac{\partial U}{\partial X} \right)^2 + 2 \left(\frac{\partial V}{\partial Y} \right)^2 + \left(\frac{\partial U}{\partial Y} + \frac{\partial V}{\partial X} \right)^2 \right\} - C_{3\varepsilon} \frac{1}{Re_t \sigma_t} \frac{\partial \rho}{\partial Y} \right] \frac{\varepsilon}{K} \end{aligned} \quad (5.6)$$

For low Reynolds number $k - \varepsilon$ turbulence model, constants used are $C_\mu = 0.09$; $C_{1\varepsilon} = 1.44$; $C_{2\varepsilon} = 1.92$; $C_{3\varepsilon} = 0.7$; $Pr_t = 0.9$; $\sigma_k = 1.0$; $\sigma_\varepsilon = 1.3$. The damping wall functions f_1 , f_2 and f_μ are as follows.

$$f_1 = 1 + \left(\frac{0.14}{f_\mu} \right)^3 \quad (5.7)$$

$$f_2 = [1 - 0.27 \exp(-R_t^2)] [1 - \exp(-R_n)] \quad (5.8)$$

$$f_\mu = \exp \left[-\frac{3.4}{1 + \left(\frac{R_t}{50} \right)^2} \right] \quad (5.9)$$

Where $Gr = \frac{g\beta\Delta TH^3}{\nu^2}$ is the Grashof number; $Ga = \beta\Delta T$ indicates Gay-Lussac's number; $Pr = \frac{\nu}{\alpha_t}$ represents Prandtl number; α_t is the thermal diffusivity; $Re_t = \frac{\varepsilon}{C_\mu \rho K^2}$; $R_t = Gr^{1/2} \left(\frac{K^2}{\varepsilon} \right)$; $R_n = Gr^{1/2} K^{1/2} n$; n is the normal distance from the nearest wall.

5.3 Boundary conditions

At the vent opening, mass and energy exchange occurs and flow modeling is complex due to the bidirectional exchange of hot and cold fluids. The solid walls are treated with adiabatic boundary conditions and no-slip boundary conditions are specified for velocity fields. The temperature of the heat source is specified with constant wall temperature. Across the horizontal vent, longitudinal velocity is set to zero and normal velocity is obtained from mass balance $\frac{\partial V}{\partial Y} = 0$. The temperature of fluid leaving through the vent satisfies the upwind boundary condition $\frac{\partial \theta}{\partial Y} = 0$. In solid walls, turbulent kinetic energy and normal gradient of dissipation is set to zero. At the vent, the normal gradients of kinetic energy and dissipation are set to zero. Uniform velocity and temperature field are specified across the inlet port. The dimensionless longitudinal velocity of ambient air at the inlet port is defined as

follows:

$$\alpha = \frac{u_\infty}{V_c} = \frac{u_\infty}{\sqrt{g\beta\Delta TH}} = \frac{Re}{Gr^{0.5}} = \frac{1}{\sqrt{Ri}} \quad (5.10)$$

Where $Ri = \frac{Gr}{Re^2}$ is the Richardson number. The Richardson number provides the measure of free convection in comparison with the forced convection.

The appropriate initial and boundary conditions in dimensionless form are as follows:

$$\text{at } \tau = 0: \quad U = V = \theta = 0 \quad (5.11)$$

for $\tau > 0$:

$$\begin{aligned} X = 0; X = 1.0; 0 < Y < 1.0: U = V = \frac{\partial\theta}{\partial X} = \frac{\partial P}{\partial X} = K = \frac{\partial\varepsilon}{\partial X} = 0; \\ X = 0; 0 < Y < H_v: V = \theta = P = 0; U = \frac{1}{\sqrt{Ri}} \end{aligned} \quad (5.12)$$

$$\begin{aligned} Y = 0; 0 < X < 1.0: U = V = \frac{\partial\theta}{\partial Y} = \frac{\partial P}{\partial Y} = K = \frac{\partial\varepsilon}{\partial Y} = 0 \\ Y = 0; 0 < X < X_{bs}: \frac{\partial\theta}{\partial Y} = 0 \\ X_{bs} < X < X_{bs} + l_s: \theta = 1.0 \\ X_{bs} + l_s < X < 1.0: \frac{\partial\theta}{\partial Y} = 0 \end{aligned} \quad (5.13)$$

$$\begin{aligned} Y = 1.0; 0 < X < X_{bv}: U = V = \frac{\partial\theta}{\partial Y} = \frac{\partial P}{\partial Y} = K = \frac{\partial\varepsilon}{\partial Y} = 0 \\ X_{bv} < X < X_{bv} + D: U = P = \frac{\partial V}{\partial Y} = \frac{\partial\theta}{\partial Y} = \frac{\partial K}{\partial Y} = \frac{\partial\varepsilon}{\partial Y} = 0 \\ X_{bv} + D < X < 1.0: U = V = \frac{\partial\theta}{\partial Y} = \frac{\partial P}{\partial Y} = K = \frac{\partial\varepsilon}{\partial Y} = 0 \end{aligned} \quad (5.14)$$

where X_{bs} is the distance upto the source; l_s is the source width; X_{bv} is the distance up to the vent; D is the vent width.

5.4 Results and Discussion

Results are presented for different inlet velocity and Grashof number. Further investigations are performed by varying inlet port size and location. The Prandtl number of air is fixed as 0.72. The value of Gay-Lussac number (Ga) for $Gr = 10^{11}$ & 10^{12} are 0.2 and 2.

5.4.1 Effect of inlet velocity

Figures 5.2&5.3 characterizes the evolution of stream function and temperature contours with and without forced inlet velocity. The width of the ceiling vent is $0.2H$ and the Grashof number is 10^{11} . An inlet port of size $H_v = 0.1H$ is located at the bottom portion of left boundary at $0.05H$. The stream function contours indicates the evolution of convective cell patterns that arises due to the density difference between the hot and cold fluids. The $\alpha = 0$ case indicates the flow situation where the inlet port is naturally opened to ambient without forced inlet velocity. For $\alpha = 0$, at time interval $\tau = 20$, primary and secondary convective cells of equal strengths are formed inside the cavity. As flow progresses, two convective cells merges to form unicellular pattern inside the enclosure. In Fig.5.2 (c&d), forced ambient air penetrates through the inlet port and strength of primary convective cell is greater than the secondary cell. The inlet air stream assists the buoyancy force and increases the outflow of hot fluid through bidirectional ceiling vent.

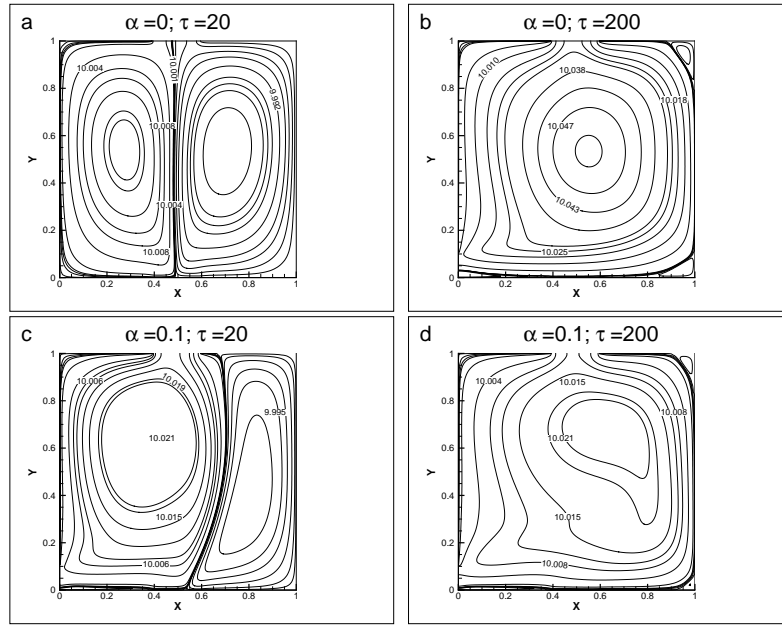


Figure 5.2: Evolution of stream function contours for different inlet velocities.

In Figure 5.3(a), axisymmetric plume evolves from the heat source, reaches the ceiling vent and spreads downwards. The plume is vented through horizontal passage and density difference drives ambient fluid to creep into the enclosure. The entrained air fills the right half of the enclosure and tilts thermal plume towards left boundary. Hence, in Fig.5.3(b) plume inclines and loses its momentum by impinging on left wall. For $\alpha = 0.1$ case where forced air supplied through inlet port, the

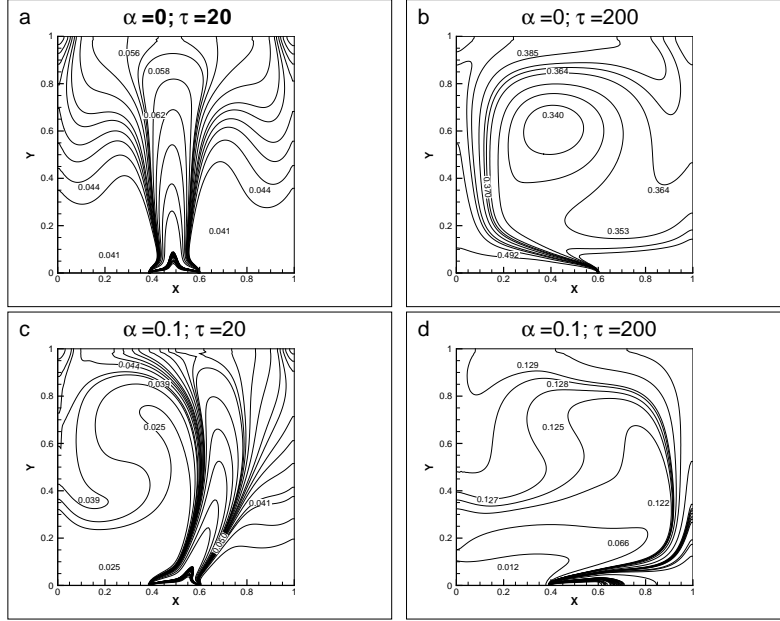


Figure 5.3: Evolution of temperature contours for different inlet velocities.

longitudinal air stream tilts thermal plume towards right boundary. A wall plume structure develops across the right boundary.

Figure 5.4(a&b) indicates the variation of temperature and density profiles along the horizontal wall at the center of square cavity. It is evident that by increasing inlet port velocity $\alpha = 0.01$ to 0.1 , the mid-height temperature distribution drastically decreases. The rise in inlet velocity assists the plume outflow rate through ceiling opening, and increases the convective heat loss from the cavity. Moreover, significant amount of cold fluid enters through inlet port and ceiling vent and reduces plume temperature. Hence, the mid-height density profiles increases with rise in inlet velocity.

Figure 5.4(c) represents the variation of net mass flow rate through ceiling vent with different inlet velocity. For $\alpha = 0$, the bidirectional exchange of hot and cold fluids are equal. Hence, the net mass flow rate magnitudes are close to zero. The net mass flow rate increases with rise in inlet velocity. The positive magnitudes indicate that plume discharge rate is higher in comparison to ambient entrainment rate.

Figure 5.5 indicates the comparison of mid-height temperature profile predicted by present non-Boussinesq and Boussinesq models for $Gr=10^{11}$ and $\alpha = 0.1$. The temperature values estimated by Boussinesq models are higher in comparison with

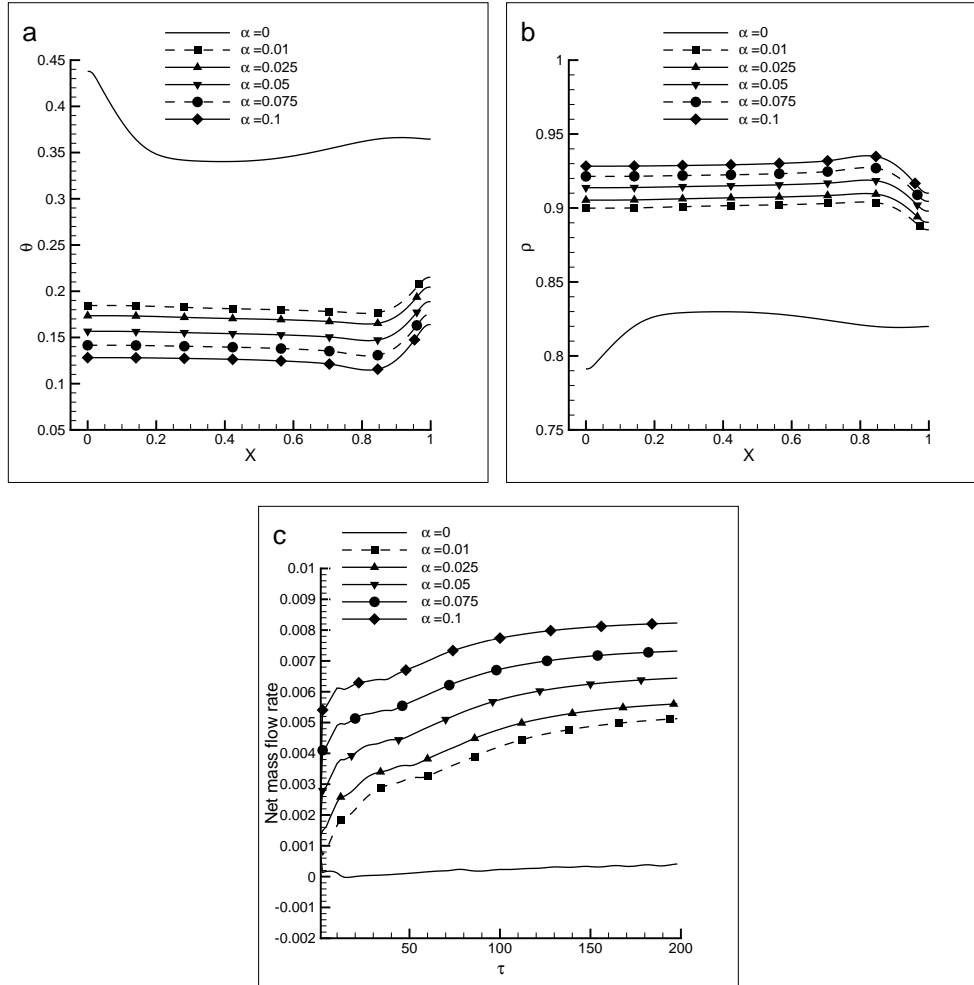


Figure 5.4: Comparison of midheight (a) temperature profile, (b) density profile and (c) net mass flow rates for different inlet velocities.

non-Boussinesq models. The deviations visualized in the temperature profiles are due to the difference in modeling of buoyancy force. The average Nusselt number estimated for Boussinesq and non-Boussinesq models are 107.53 and 105.86 respectively. It is identified that Boussinesq model over-predicts the temperature and Nusselt number variation.

5.4.2 Effect of Grashof number

Figure 5.6(a) indicates the variation of mid-height longitudinal velocity for two different Grashof numbers 10^{11} & 10^{12} and inlet velocity $\alpha = 0.01$ & 0.1 . With rise in Grashof number and inlet velocity, the base temperature difference and plume velocity increases and the location of peak longitudinal velocity is along the midsection of the square cavity. The normal velocity profiles across the horizontal opening are plotted in Fig.5.6(b) for $Gr=10^{11}$ & 10^{12} and $\alpha = 0.01$ & 0.1 . The positive

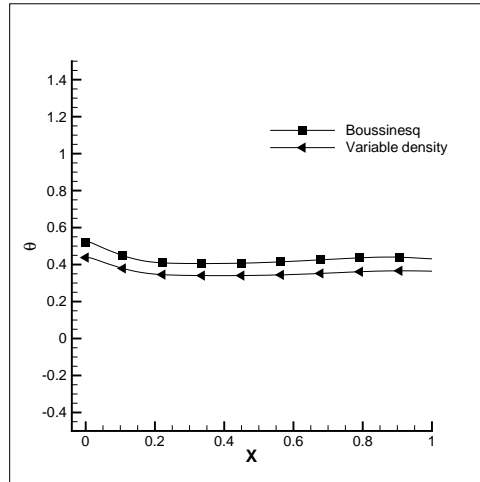


Figure 5.5: Comparison of midheight temperature profiles with Boussinesq and Non-Boussinesq approach.

and negative sign across the vent indicates hot and cold fluid velocities. It can be seen that the ambient entrainment rate is relatively very small in comparison with plume venting rate. Figure 5.6(c) represents the variation of ceiling vent net mass flow rates for different inlet velocity. The heat loss from the cavity increases by varying inlet velocity α from 0.01 to 0.1. The forced air stream assists buoyancy force and accelerates the plume out flow rate. Hence by increasing α , a steep rise in the net mass flow rate values are visible across the horizontal opening.

Figure 5.6(d) shows the plots of average Nusselt number by varying Gr and α . For $Gr=10^{11}$, α is varied from 0.0 to 0.1 and the average Nusselt number increases by 5.4%, 6.6%, 7.8%, 9% and 10.2 % respectively. From the Nusselt number plots it is evident that heat loss from the cavity increases with rise in inlet velocity. Moreover, a rise in Grashof number enhances heat transfer rate and the average Nusselt number for $Gr=10^{12}$ is 11 percent higher in comparison with $Gr=10^{11}$.

5.4.3 Effects of inlet port opening height (H_v)

The investigations are performed for inlet port opening height H_v , varied from $0.1H$ to $0.2H$ for $Gr=10^{11}$. Figure 5.7(a) represents the variation of temperature profiles along the horizontal wall plotted at the mid-height of square cavity for $H_v = 0.1H$ & $0.2H$ and $\alpha = 0.01$ to 0.1. It is visualized that with increase in inlet port height, significant amount of ambient fluid enters the cavity, and reduces the plume temperature. For $H_v = 0.2H$, and α varied from 0.01-0.1, the plume

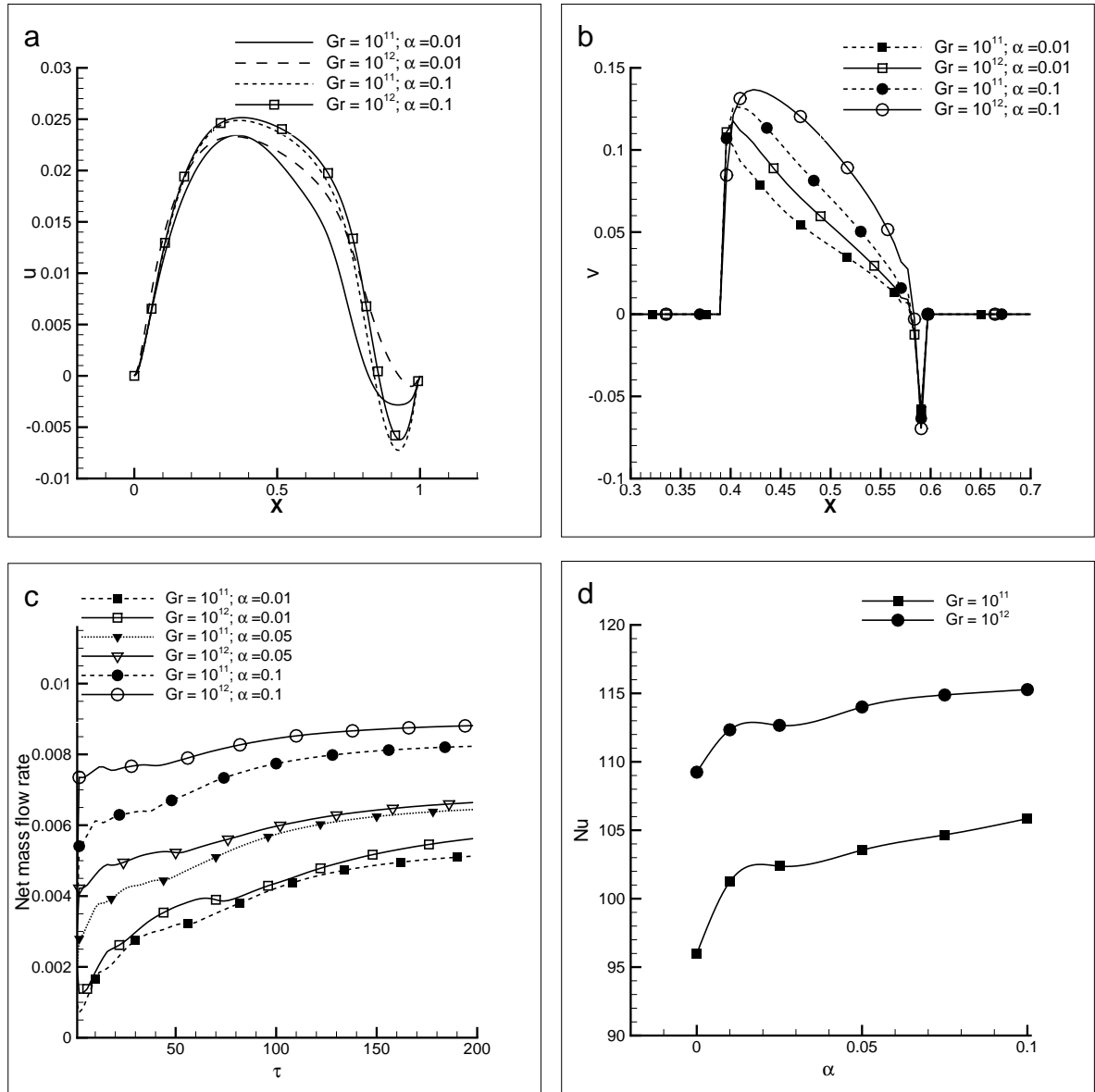


Figure 5.6: Effect of Gr & α on (a) Midheight longitudinal velocity profile; (b) Normal velocity profiles across horizontal vent; (c) Net mass flow rates and (d) Average Nusselt number.

temperature decreases by 24.3%, 26.7%, 28.6%, 30.5% and 33.2 % respectively. A comparison of net mass flow rate through the ceiling vent is shown in Fig.5.7(b) for different H_v & α . The assisting flow through inlet port strengthens the plume spread and further increases the discharge of hot fluid through ceiling vent. Hence the net mass flow rate increases with H_v & α .

The average Nusselt number variation for different H_v & α are plotted in Fig.5.7(c). The forced ambient inlet intensifies the heat transfer rate and the average Nusselt

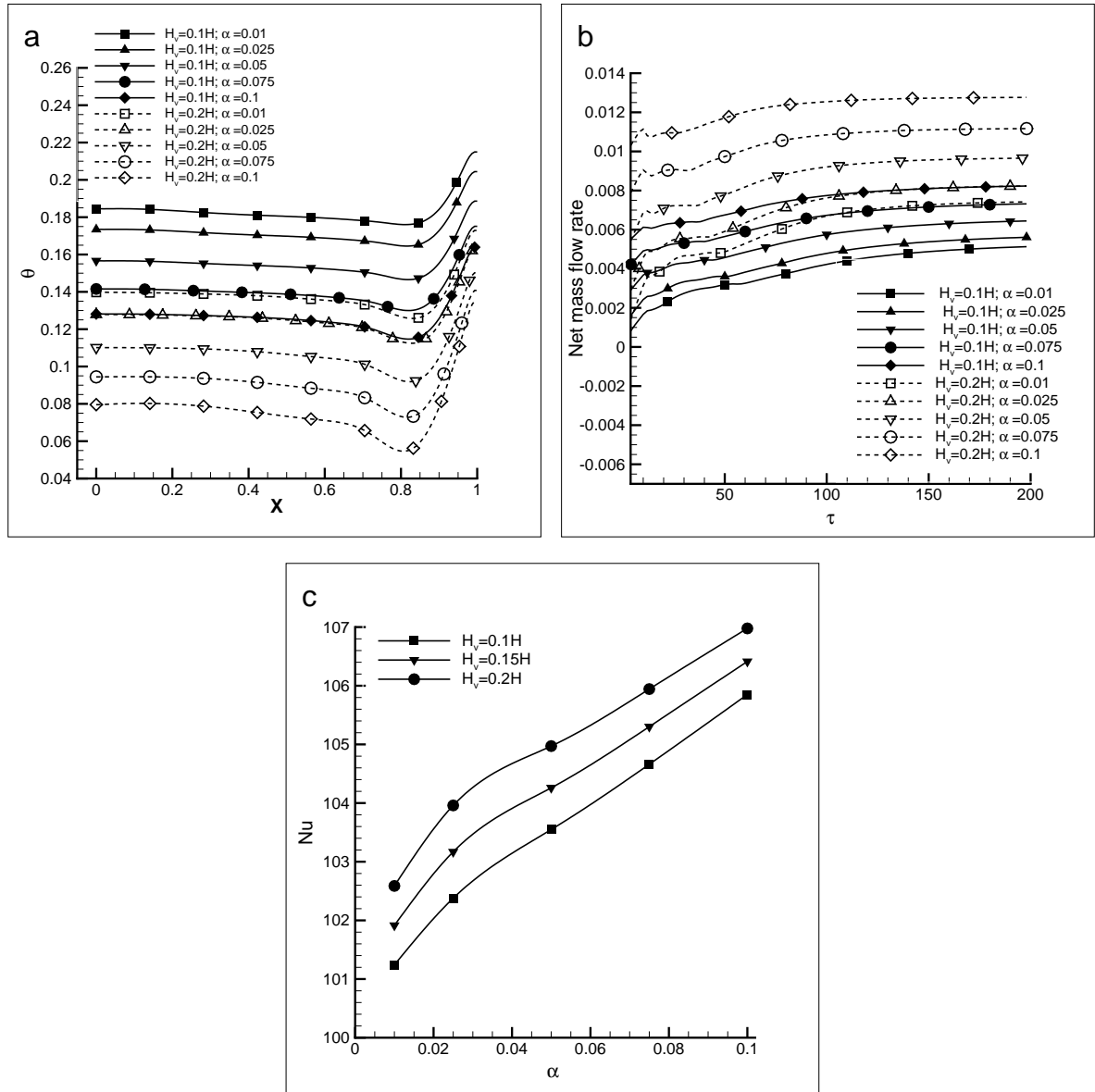


Figure 5.7: Comparison of midheight (a) temperature profile, (b) net mass flow rates and (c) average Nusselt number for different H_v & α .

number increases with H_v & α .

5.4.4 Effects of inlet port location (V_L)

The illustrations shown in Fig 5.8 indicates the stream function (a&b) and temperature (c&d) contours for $Gr = 10^{11}$. The width of the centrally located ceiling vent is $0.2H$. A forced inlet port of height $H_v = 0.1H$ is located at $\frac{3}{4}H$ of the left boundary. The forced air stream increases the strength of primary convective cell and well mixed unicellular pattern is visualized at $\tau = 200$. The opposing flow

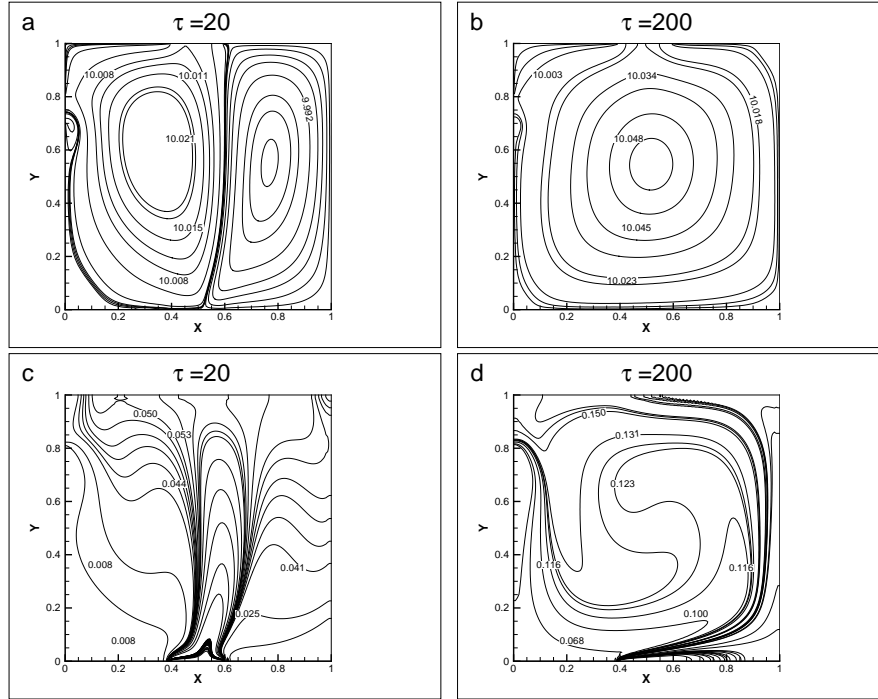


Figure 5.8: Evolution of stream function (a,b) and temperature (c,d) contours for $V_L = 0.75H$; $\alpha = 0.1$.

distorts the symmetric pattern of thermal plume, weakens thermal buoyancy force and shifts the plume movement towards right boundary. The temperature distribution along the horizontal wall at the center of square enclosure is plotted in Fig.5.9(a) for different V_L and α . The opposing flow reduces the convective heat loss from the cavity and increases the temperature concentration inside the enclosure. The mid-height temperature values increases with V_L & α .

The effect of inlet port location V_L on net mass flow rate through ceiling vent is represented in Fig.5.9(b). The forced air stream suppresses the buoyancy force and reduces the bidirectional exchange rate through vent. Hence, the net mass flow rates are significantly less for $V_L = 0.75H$ in comparison to $V_L = 0.05H$. Figure 5.9(c) illustrates the comparison of average Nusselt number by varying V_L & α . The convective heat loss from the cavity is minimized and the average Nusselt number values drops linearly with V_L & α . There is a 2 to 4.5 percent decrease in the average Nusselt number for $V_L = 0.75H$ in comparison to $V_L = 0.05H$.

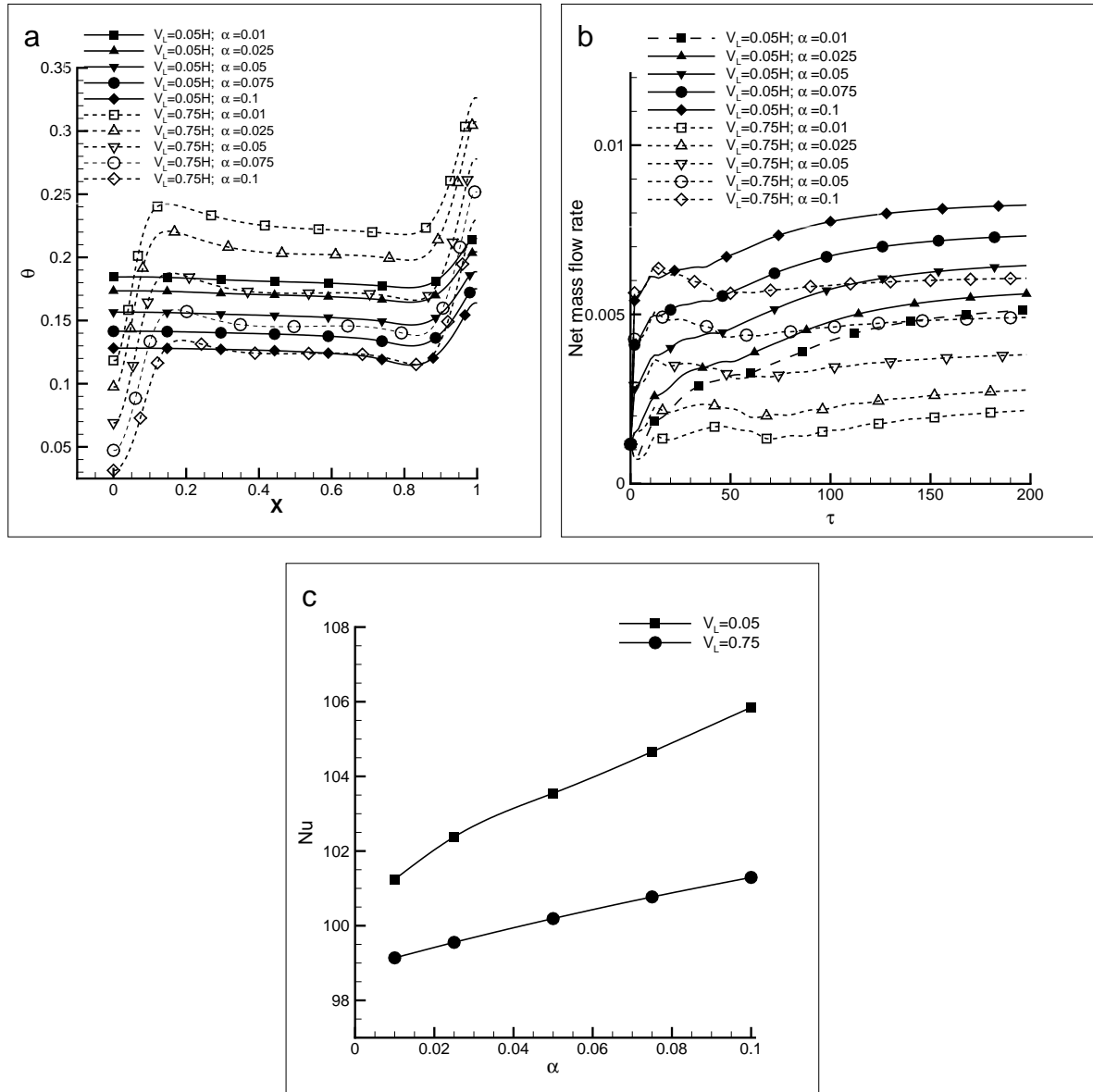


Figure 5.9: Comparison of midheight (a) temperature distribution (b) net mass flow rate (c) average Nusselt number for different inlet port location & α .

5.5 Summary

The buoyancy dominated combined convection flow in partially open enclosure with forced inlet port is numerically studied. The bidirectional exchange rates through ceiling vent are investigated by varying Grashof number, forced longitudinal velocity and inlet port location. For assisting flow case, forced air stream strengthens thermal buoyancy force and increases plume discharge rate through ceiling vent. This increased the convective heat loss from cavity, and temperature magnitudes decreased significantly inside the cavity. The average Nusselt number increases with

longitudinal velocity. The vent discharge rate increases with rise in Grashof number and the average Nusselt number for $Gr = 10^{12}$ is increased by 11 percent. An increase in inlet port height intensifies net mass flow rate through ceiling vent and decreases the temperature distribution inside the enclosure. The opposing flow weakens thermal buoyancy force and minimizes the convective heat loss from cavity. The opposing forced air stream reduces bidirectional exchange through ceiling vent. The present results are useful for understanding the growth and spread of thermal plume inside a vented enclosure.

Chapter 6

Tunnel ventilation

With increasing number of fire accidents in tunnels, it is necessary to understand the effects of natural ventilation system in controlling smoke propagation rate. However, studies on the effects of heat source locations and multiple ceiling vents in tunnels are limited. This chapter presents the significance of naturally ventilated roof openings in controlling the longitudinal propagation of hot gases. Transient three-dimensional simulations are performed in tunnel by Large Eddy Simulations (LES) using Fire Dynamic Simulator (FDS) code [105, 106].

6.1 Problem definition

Numerical simulations are carried out in a tunnel shown in Fig.6.1 which is 100 m long, 3m wide and 2.5m high. The tunnel model is scaled by a factor of $\frac{1}{6}$ according to Froude-Scaling law. This corresponds to full-scale tunnel which is 600 m long, 18 m wide and 15 m high. In scaled model, heat source with square cross-section $0.75m \times 0.75m$ releases heat at the rate of $1500kW/m^2$. The dimension of ceiling opening is $0.5m \times 0.5m$ and is opened to ambient environment. The temperature of hot gas moving upstream and downstream of the tunnel are monitored by mounting 100 thermocouples ($T_{c_1} - T_{c_{100}}$) located at 0.25 m below the ceiling.

6.2 Governing equations

The buoyancy induced flow problem is modeled by solving unsteady, three-dimensional compressible Navier-Stokes equation suitable for low Mach number flows. In present analysis, non-Boussinesq variable density solver is utilized

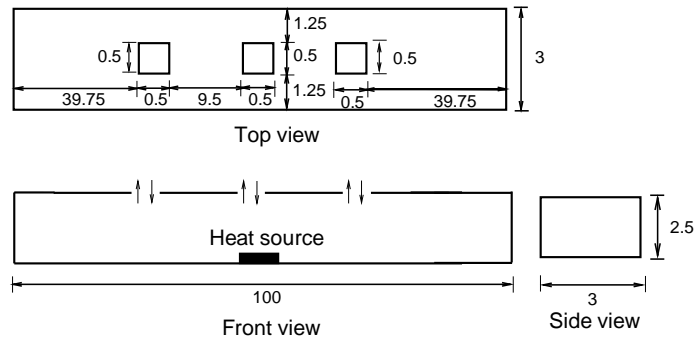
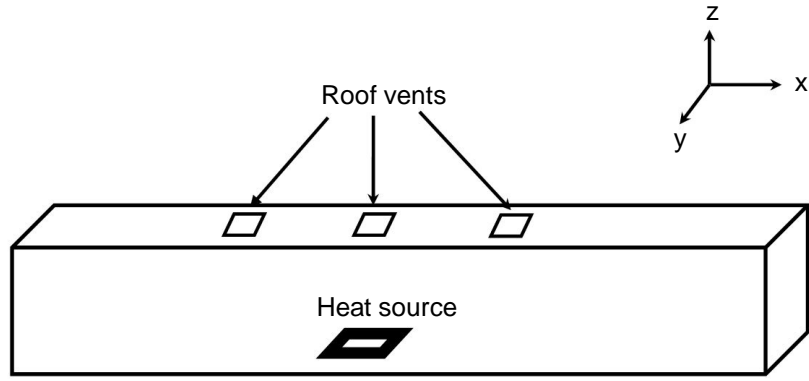


Figure 6.1: Schematic diagram of tunnel with roof openings 3-D view and 2-D view (dimensions in m).

in evaluating density differences. The turbulent eddies that account for most of mixing and large scale motions are obtained through filtering operations applied to momentum and energy equations leading to large scale momentum and thermal energy transport equations.

The velocity and temperature fields are defined as the sum of filtered component and residual component as shown below:

$$u_i = \bar{u}_i + u_i' \quad (6.1)$$

$$T = \bar{T} + T' \quad (6.2)$$

The filtered velocity and temperature fields are obtained by solving filtered Navier-Stokes equation and residuals are resolved using sub-grid model.

The mathematical form of filtered Favre-Averaged Navier-Stokes for buoyancy induced flows are as follows:

Conservation of mass:

$$\frac{\partial \rho}{\partial t} + \frac{\partial(\rho u_j)}{\partial x_j} = 0 \quad (6.3)$$

Conservation of momentum:

$$\frac{\partial}{\partial t}(\rho u_i) + \frac{\partial(\rho u_i u_j)}{\partial x_j} = -\frac{\partial p}{\partial x_i} + \rho g + \frac{\partial \tau_{ij}}{\partial x_j} \quad (6.4)$$

The stress tensor τ_{ij} is defined as follows:

$$\tau_{ij} = 2\mu S_{ij} + (\tau_{ij})_{SGS} \quad (6.5)$$

$$(\tau_{ij})_{SGS} = 2\mu_{LES} S_{ij} - \frac{2}{3}\delta_{ij}(\nabla \cdot u) \quad (6.6)$$

$$S_{ij} = \frac{1}{2} \left(\frac{\partial u_i}{\partial x_j} + \frac{\partial u_j}{\partial x_i} \right) \quad i, j = 1, 2, 3 \quad (6.7)$$

where $(\tau_{ij})_{SGS}$ is Subgrid Scale(SGS) stress tensor, μ represents the dynamic viscosity of fluid, μ_{LES} represents the Smagorinsky dynamic viscosity, S_{ij} denotes the strain tensor and δ_{ij} is the kronecker delta.

The above equations are coupled with the energy equation given below:

Conservation of energy:

$$\frac{\partial}{\partial t}(\rho T) + \frac{\partial(\rho u_i T)}{\partial x_i} = \frac{Dp}{Dt} - \frac{\partial}{\partial x_i} \left(\frac{k}{C_p} \frac{\partial}{\partial x_i} + q_{SGS} \right) + q_r \quad (6.8)$$

where q_{SGS} represents subgrid scale heat flux. The thermal radiation effects (q_r) that arise from fire source are determined by solving radiation transport equation.

The temperature variations are related to density and pressure by equation of state.

Ideal-gas law:

$$p = \rho RT \quad (6.9)$$

The small-scale turbulent eddies are resolved using sub-grid model developed by

Smagorinsky (Smagorinsky 1963). The Courant-Friedrichs-Lewy (CFL) criterion (Lax 1967) is used to assure numerical convergence. Smagorinsky dynamic viscosity is defined as

$$\mu_{LES} = \rho(C_s\Delta)^2 \left(2S_{ij}S_{ij} - \frac{2}{3}(\nabla \cdot u)^2 \right)^{\frac{1}{2}} \quad (6.10)$$

where C_s is an empirical Smagorinsky constant and Δ is called the filter width determined from the cube root of grid volume $\Delta = (\Delta x \Delta y \Delta z)^{\frac{1}{3}}$.

6.3 Grid Sensitivity

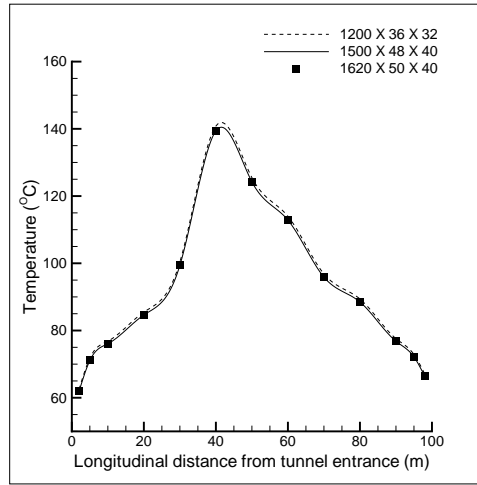


Figure 6.2: Temperature variation towards the tunnel upstream side measured from heat source.

Table 6.1: Grid Independence with three mesh sizes.

S.No	x cells	y cells	z cells	Total number of cells
1	1200	36	32	1,382,400
2	1500	48	40	2,880,000
3	1620	50	40	3,240,000

To ensure that numerical solutions are independent with selected mesh size, simulations are performed with three different grid sizes. The grid details in x,y&z directions are given in Table 6.1. The temperature variation along the entire tunnel measured at 0.25 m below the ceiling are plotted with three different mesh sizes. The heat source intensity is $1500kW/m^2$. The plots in Fig. 6.2 indicates that solution is grid independent with grid sizes of $1500 \times 48 \times 40$. Hence all results are

presented with the above grid system.

6.4 Validation

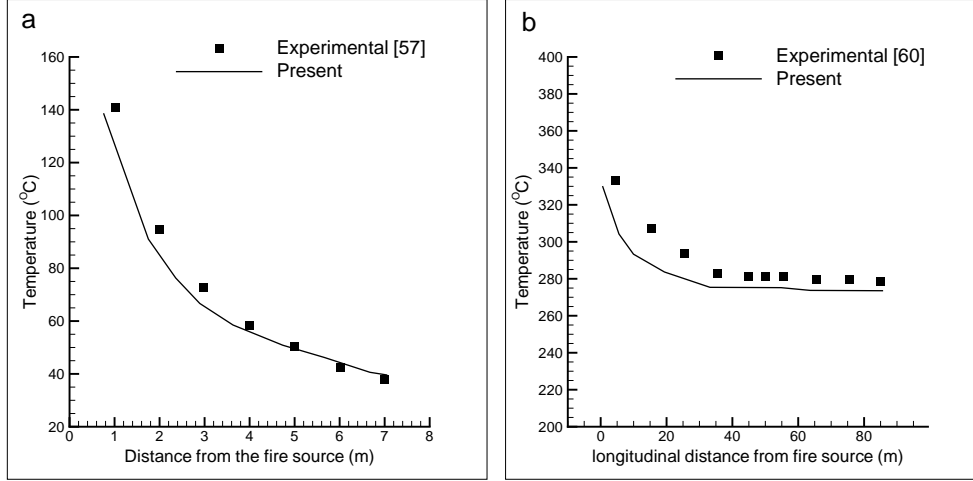


Figure 6.3: Validation of present results with experimental results

The capability of computational fluid dynamic model in predicting tunnel flow characteristics is validated by comparing present numerical results with the experimental results available in literature. Experimental study [57] in longitudinally ventilated tunnel were carried out with different aspect ratios. The aspect ratio was calculated as height divided by width and seven thermocouples were installed below the ceiling towards tunnel exit to measure temperature distribution. The tunnel is 10.4 m long and fire source is placed at a distance of 3 m from tunnel left opening. Simulations are performed with grid size of $650 \times 40 \times 20$. Figure 6.3(a) shows temperature profile under the ceiling in a tunnel of aspect ratio 0.5 with heat source intensity 8.27 kW. A comparison of present and experimental results are shown in Fig. 6.3(a). It is observed that as hot gas moves downstream towards tunnel exit, distance from the heat source increases and hence magnitude of ceiling temperature decreases. The simulation results are in good agreement with experimental [57] results. Further validations are performed in comparison with experimental investigations [60] reported in naturally ventilated tunnel with roof openings. The tunnel is 1410 m long with heat source of intensity 7.5 MW located at a distance of 135.2 m from tunnel right opening. Simulations are performed in scaled tunnel geometry with dimensions $230m \times 12.35m \times 5.75m$. The grid size is $650 \times 40 \times 20$. Fig. 6.3(b) shows the comparison of present results with experimental

data. The upstream longitudinal temperature distribution under the ceiling from heat source is plotted. The temperature profile decreases as longitudinal distance increases and present numerical model are in good agreement with experimental results [60]. The comparison in Fig 6.3(a,b) shows that present CFD model is relatively good in predicting buoyancy induced flows in tunnel.

Table 6.2: Smoke layering length for heat release rate of 80 kW.

Point extraction velocity (m/s)	Upstream		Downstream	
	Present (m)	Experimental (Chen et al.,[104]) (m)	Present (m)	Experimental (Chen et al.,[104]) (m)
1.5	18.48	19	19	18.5
1.8	14.1	14.5	15	14.5

The present numerical solutions are compared with experimental data [104] with roof ventilation. The computational domain for validation is $72m \times 1.5m \times 1.3m$, discretized with grid size of $1400 \times 36 \times 30$. Simulations are performed with two different point extraction velocities without longitudinal ventilation. The heat source intensity is 80 kW. Table 6.2 summarizes the comparison of smoke layering length measured by numerical simulation and experimental data. The numerical simulations are closer to experimental data and CFD LES model is capable of predicting buoyant flows in roof ventilated tunnel.

6.4.1 Results and discussion

The flow characteristics inside naturally ventilated tunnel are investigated with single and multiple roof openings by varying the locations of heat source. Further simulations are extended with multiple roof openings by changing the size of openings and by placing two heat sources.

6.4.1.1 Comparison of results with and without roof vent

Numerical simulations are carried out to understand the effect of ceiling vents in removing hot gases by comparing cases with and without roof vents. The time evolution of isosurfaces of thermal plume are shown in Fig. 6.4(a-d). The heat source is located at the center of tunnel at a distance of 50 m from tunnel entrance. The illustrations shown in Fig. 6.4(a&b) indicates the thermal plume isosurface for case without ceiling vent. Similarly Fig. 6.4(c&d) represents the results for case with centrally mounted ceiling vent. It is visualized from Fig. 6.4(a&b) that thermal

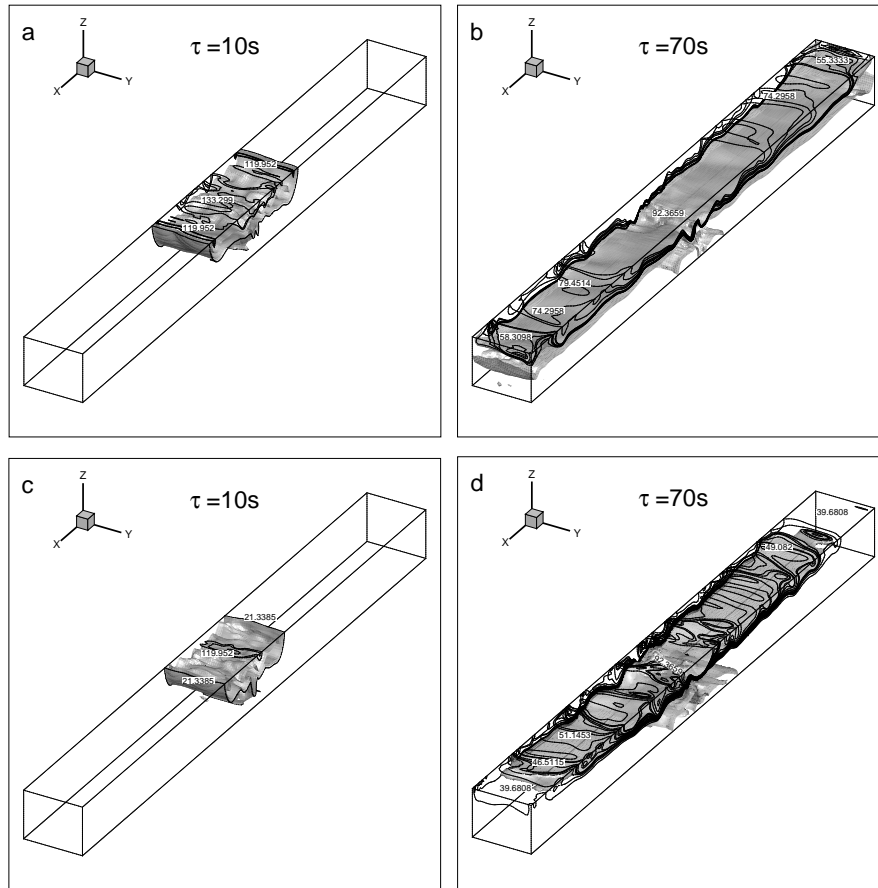


Figure 6.4: (a&b) Evolution of isosurfaces of thermal plume inside tunnel without ceiling vent (c&d) Evolution of isosurfaces of thermal plume inside tunnel with ceiling vent.

plume rises from heat source and impinges on tunnel ceiling at $\tau = 10s$. As flow progresses, at $\tau = 70s$, plume approaches the tunnel left and right openings. It is evident from Fig. 6.4(b) that buoyancy force drives the plume to spread along longitudinal and lateral directions. A significant rise in temperature is visualized near the upper half of tunnel when compared to lower half. In comparison with Fig. 6.4(b&d) for tunnel with ceiling vent, plume reaches tunnel entrance and exit locations at time $\tau > 70s$, since ceiling vent controls the spreading of thermal plume. Fig. 6.4(c&d) indicates that central ceiling vent removes hot gases and thermal plume lose its momentum and hence ceiling vent reduces the longitudinal movement of smoke and toxic gases.

The upstream and downstream smoke temperature distributions are shown in Fig. 6.5 for cases with and without ceiling opening. For tunnel with ceiling opening it is seen that there is a significant decrease in temperature magnitudes along the tunnel as ceiling vent minimizes the propagation of hot gas towards tunnel portals. The

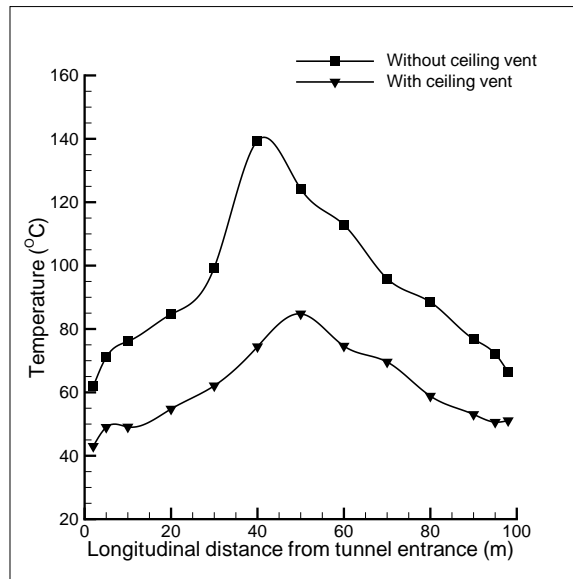


Figure 6.5: Temperature distribution along the entire length of tunnel.

plots shown in Fig. 6.6 (a&b) indicates comparison of net mass flow rate through the tunnel left and right openings without and with ceiling vent. In Fig. 6.6 (a), hot fluid leaves the tunnel through right and left openings. Fig. 6.6 (b) shows the inflow of ambient fluid through the tunnel portals. The entrainment effects across left and right openings are represented by positive and negative magnitudes. For tunnel with ceiling vent there is a significant decrease in the mass outflow rates which indicates that ceiling vent controls back layering of hot gas and restricts the longitudinal spreading of thermal plume.

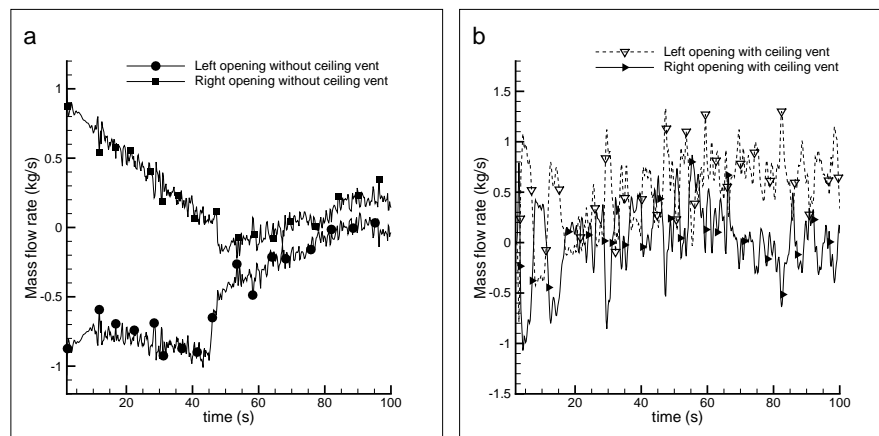


Figure 6.6: (a) Mass flow rate through tunnel portals without roof opening; (b) Mass flow rate through tunnel portals with roof opening.

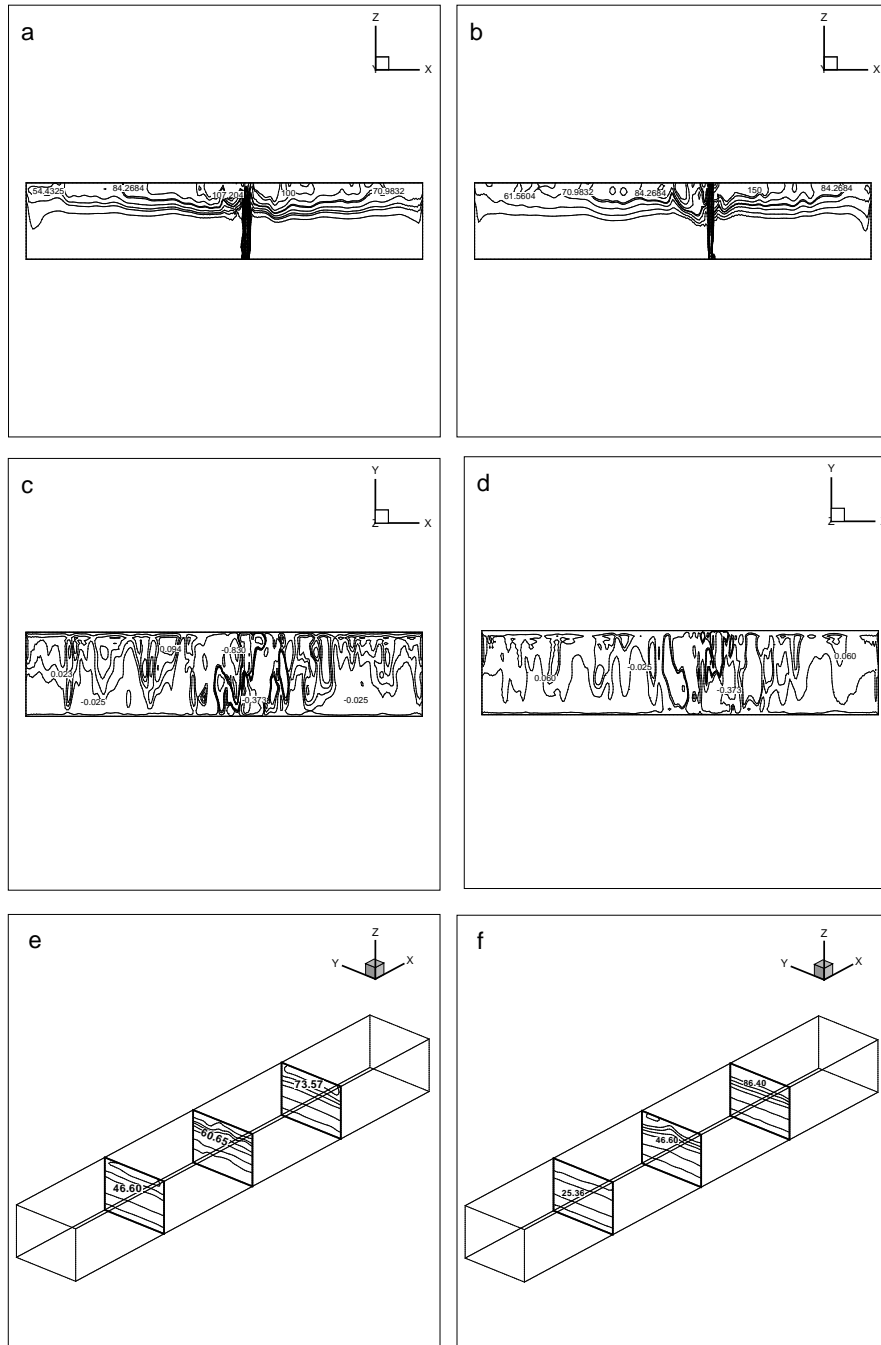


Figure 6.7: Comparison of temperature distribution inside roof vented tunnel with different heat source location: (a&b) Temperature contours along xz plane at $y=1.5$ m ; (c&d) Normal velocity contours along xy plane at $z=2.25$ m and (e&f) Temperature contours along yz plane.

6.4.1.2 Effect of heat source location

To understand the effects of heat source location and its influence on smoke removal efficiency, results are shown in Fig. 6.7 and 6.8 for tunnel with centrally mounted ceiling vent with different heat source locations. Simulations are carried out with

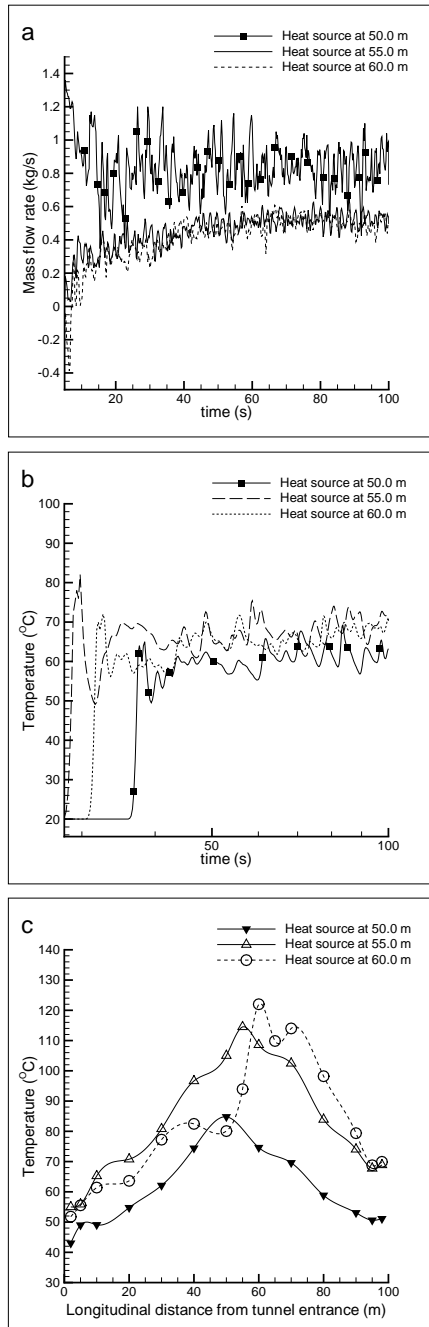


Figure 6.8: (a) Mass flow rate through roof opening; (b) Temperature variation with time monitored by thermocouple at 30.0 m from tunnel entrance; (c) Temperature distribution along the entire tunnel.

two different heat source locations at distance of 55.0 m and 60.0 m measured from tunnel entrance. The temperature contours are shown in Fig. 6.7(a&b) along the xz plane at $y = 1.5$ m for two heat source locations. It is observed from the magnitude of temperature contours that longitudinal propagation of thermal plume towards downstream side of tunnel is higher than upstream side. Since heat source is located

at $x = 60.0$ m, concentration of temperature magnitudes are higher near downstream side of the tunnel and temperature decreases towards upstream side of tunnel. Fig. 6.7(c&d) represents the comparison of normal velocity contours along xy axis at $z = 2.25$ m. The positive and negative magnitudes represents the plume and ambient air velocities. It is visualized from Fig. 6.7(c) that entrainment of ambient air from central roof vent is higher for heat source located at 55.0 m. In Fig. 6.7(d) there is slight decrease in the concentration of velocity patterns near tunnel upstream side. Fig. 6.7(e&f) represents the temperature contours along yz plane at three different locations along tunnel horizontal axis at $x = 25.0$ m, 50.0 m and 75.0 m. It is observed that as the upstream and downstream longitudinal distances from fire source increases the temperature magnitude decreases.

However in the present analysis shown in Fig. 6.7, ceiling vent is not located directly above the heat source and as flow progresses plume impinges towards ceiling, further gains momentum and spreads longitudinally. From temperature contours in Fig. 6.7 it is evident that temperature magnitudes are higher when heat source is located away from central vent. The thermal plume bypasses the ceiling opening and propagates towards upstream side. As longitudinal distance between fire source and ceiling vent increases, smoke venting efficiency through ceiling vent decreases.

Figure 6.8 (a) represents the comparison of net mass flow rates through ceiling vent for cases with centrally located heat source and with heat source placed at 55.0 m and 60.0 m from tunnel entrance. The net mass flow rates are higher for centrally located heat source when compared to heat source located at 55.0 m and 60.0 m. Figure 6.8 (b) represents the temperature variation with time recorded by thermocouple placed at 30.0 m from tunnel entrance and comparison is shown for three different heat source locations. The temperature distribution along the entire tunnel is shown in Fig. 6.8 (c) for different heat source locations. From Fig. 6.8 (b&c) it is observed that magnitude of temperature is lower for heat source placed above the roof opening when compared to other two cases. Moreover there is a significant increase in the longitudinal velocity and propagation of smoke towards upstream side of tunnel for heat source placed at 55.0 m and 60.0 m. Hence it is concluded that for tunnel with centrally mounted ceiling vent, as longitudinal distance between heat source and vent varies a single naturally ventilated roof opening is insufficient to exhaust all hot gases.

6.4.1.3 Effect of multiple roof openings

To investigate the impact of heat source locations with multiple ceiling vents further simulations are performed in tunnel to identify whether additional openings are

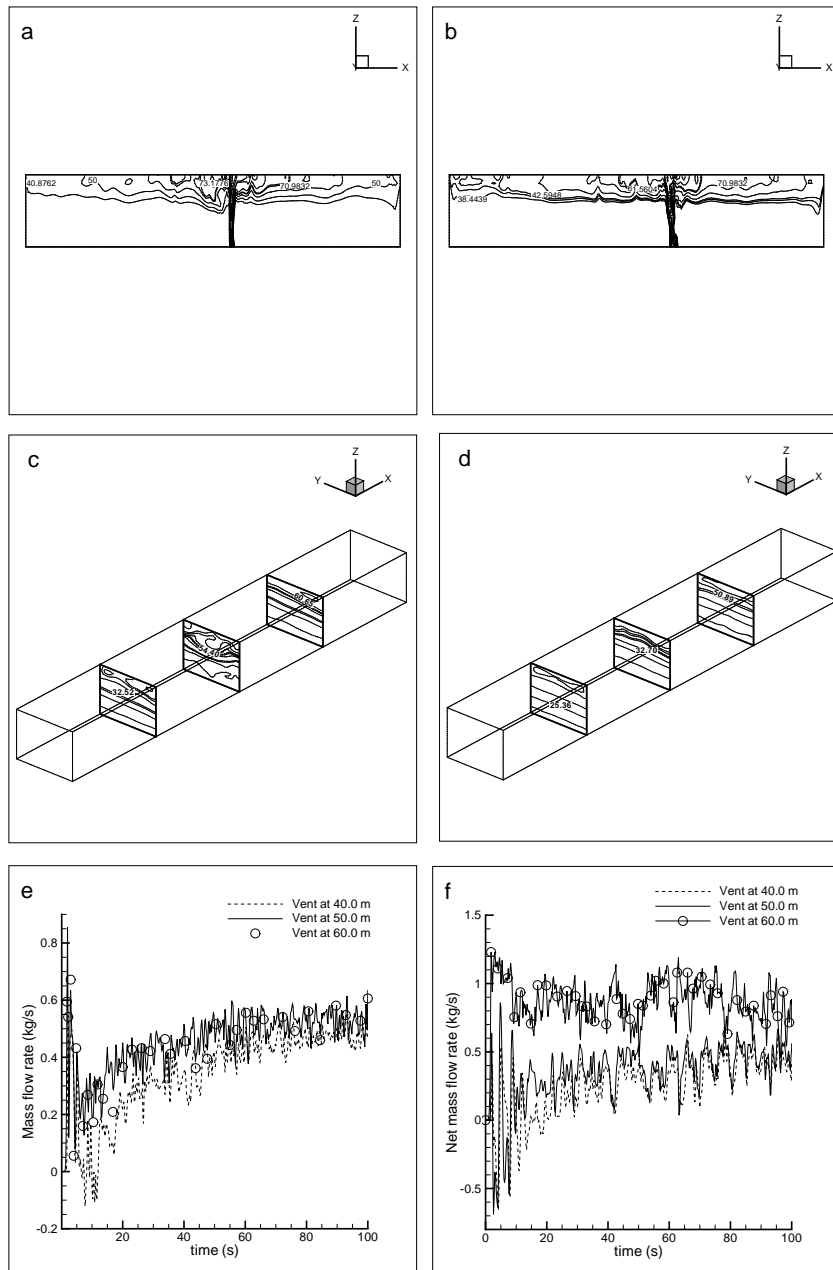


Figure 6.9: (a-d) Comparison of temperature distribution inside multiple roof vented tunnel with different heat source location;(e) Comparison of mass flow rate through three roof openings for heat source placed at 55.0 m; (f) Comparison of mass flow rate through three roof openings for heat source placed at 60.0 m

effective for hot gas removal. Figure 6.9 indicates the results for vent dimension $0.5m \times 0.5m$. Three ceiling vents are mounted on the roof top at distance of 40.0 m, 50.0 m and 60.0 m measured from tunnel entrance. The analysis is performed by placing heat source of size $0.75m \times 0.75m$ at two different locations at distance of 55.0 m and 60.0 m measured from tunnel entrance. Figure 6.9 (a-d) indicates the

temperature contours for heat source placed at 55.0 m and 60.0 m respectively. The additional openings located at $x=40.0$ m & 60.0 m are capable of removing hot gases that bypasses the central opening and further reduces the magnitude of longitudinal temperature distribution. Hence multiple ceiling vents are effective in transferring the hot gases to ambient atmosphere. Figure 6.9 (e&f) shows the comparison of net mass flow rate through three ceiling vents with different heat source locations. For heat source located at 55.0 m, significant amount of hot fluid leaves through vent placed at tunnel center. For heat source located at 60.0 m, significant amount of hot fluid leaves through the vent placed at $x= 60.0$ m when compared to center vent. Moreover thermal plumes that bypass the center opening are vented to ambient through roof vent mounted at $x= 40.0$ m. Hence it is concluded that multiple openings are effective in removing the buoyancy driven hot gases and reduces the temperature inside the tunnel environment.

6.4.1.4 Effect of roof vent size

Figure 6.10 indicates the comparison of results with two different vent sizes $0.5m \times 0.5m$ and $0.3m \times 0.3m$ for heat source placed at 55.0 m. Figure 6.10 (a) represents the net mass flow rate through central roof opening and with reduction in opening dimensions the net quantity of hot fluid leaving through vent decreases. Figure 6.10 (b) shows temperature profile variation with time measured by thermocouple placed at 30.0 m from tunnel entrance. The plot indicates that with decrease in vent size, less quantity of hot fluid is vented to ambient and temperature inside the tunnel increases. The temperature distribution inside the tunnel are shown in Fig. 6.10 (c) for two vent sizes. With decrease in vent size relatively larger proportion of thermal plume propagates towards upstream and downstream side of the tunnel and hence temperature inside the tunnel increases with decrease in vent size.

6.4.1.5 Effect of dual heat sources

Further simulations are carried out in tunnel with multiple vents of dimensions $0.5m \times 0.5m$ by simultaneously placing two heat sources of size $0.5m \times 0.5m$ with intensity of $1500kW/m^2$. The heat sources are positioned at two intermediate locations at 40.0 m and 60.0 m from tunnel entrance. The temperature contours are shown in Fig. 6.11 (a-c). The plume from two heat sources are unified near tunnel central portion. In Fig. 6.11 (a-c) the concentration of maximum temperature magnitude are near the central portion of tunnel and as longitudinal distance from heat source increases temperature decreases. Figure 6.11 (d) shows the net mass flow rate comparison through three roof openings. It is seen that net quantity of

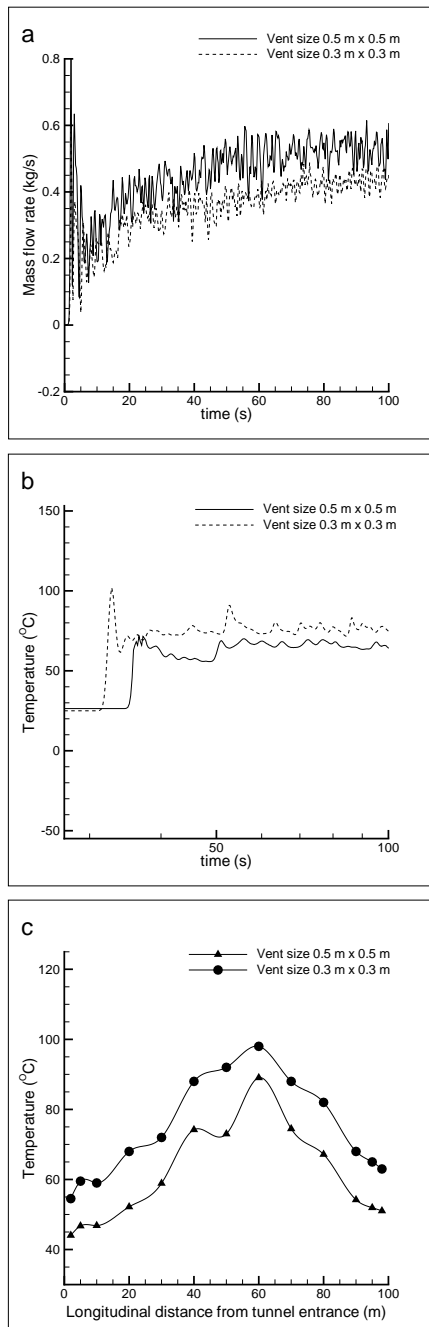


Figure 6.10: (a) Comparison of mass flow rate through central roof opening for two vent sizes; (b) Temperature variation with time monitored by thermocouple at 30.0 m from tunnel center; (c) Temperature distribution along the entire tunnel.

fluid leaving through central ceiling vent is higher when compared to the other two vents since longitudinal plume velocity is higher near central portion of the tunnel. Hence it is concluded that for tunnel with multiple openings with two heat sources, central ceiling vent is effective in removing the hot gases.

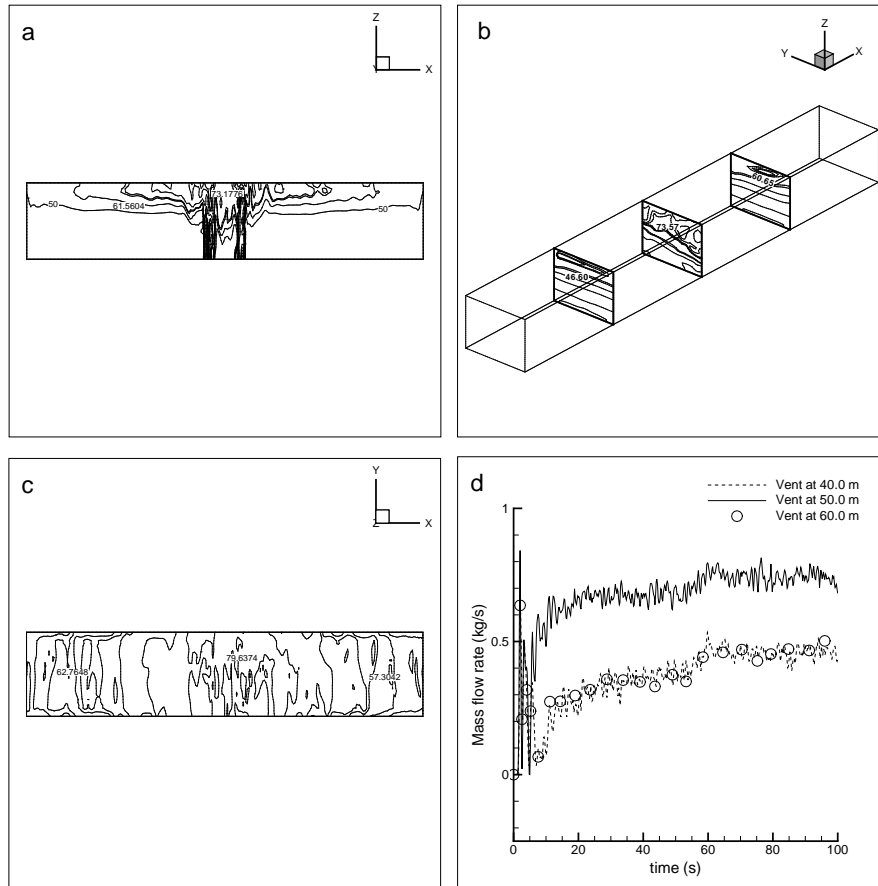


Figure 6.11: (a-c) Temperature distribution inside multiple roof vented tunnel with two heat sources; (d) Comparison of mass flow rate through three roof openings.

6.4.1.6 Quantification of smoke traveling time and maximum longitudinal velocity

Table 6.3 represents the hot gas traveling time and maximum longitudinal velocities near the tunnel left and right openings for different cases in the present investigation. It is evident from Table 6.3 that naturally vented roof openings removes the hot toxic gases and reduces the smoke longitudinal velocities and travel time thereby reduces the smoke concentration and improves visibility inside the tunnel.

Table 6.3: Smoke traveling time and maximum longitudinal velocity near the tunnel left and right openings

Cases	τ_u	Upstream (U_{max})	τ_d	Downstream (U_{max})
	(s)	(m/s)	(s)	(m/s)
Center Heat source without ceiling vent	65	1.2	65	1.2
Center Heat source with central ceiling vent	75	0.7	75	0.7
Heat source at 55 m with central ceiling vent	70	0.9	68	1.08
Heat source at 60 m with central ceiling vent	72	0.65	50	1.15
Heat source at 55 m with multiple ceiling vents	75	0.8	70	0.89
Heat source at 60 m with multiple ceiling vents	78	0.62	65	0.94
Multiple ceiling vents reduced size	70	0.69	65	0.87
Two heat sources with multiple ceiling vents	75	0.78	75	0.8

Table 6.4: Smoke layering length.

Cases	Upstream		Downstream	
	FDS (m)	Eq.(6.11) (m)	FDS (m)	Eq.(6.11) (m)
Center Heat source without ceiling vent	24.5	25.8	24.5	25.8
Center Heat source with central ceiling vent	16.8	17.2	16.8	17.2
Heat source at 55.0 m with central ceiling vent	17.8	18.3	18.4	18.9
Heat source at 60.0 m with central ceiling vent	16.5	16.7	19.2	19.5
Heat source at 55.0 m with multiple ceiling vents	15.7	16.0	16.4	16.8
Heat source at 60.0 m with multiple ceiling vents	15.2	15.6	16.0	16.2
Multiple ceiling vents reduced size	16.3	16.5	16.8	17.0
Two heat sources with multiple ceiling vents	17.2	17.6	17.8	17.6

The smoke back-layering length under the influence of roof ventilation was proposed by Chen et al., [104].

$$l^* = 18.5 \ln \left(0.81 \frac{Q_0^{*1/3}}{v^*} \right), Q^* \leq 0.15 \quad (6.11)$$

$$l^* = 18.5 \ln \left(\frac{0.43}{v^*} \right), Q^* > 0.5$$

$$Q^* = \frac{Q_0 - C_p \rho V S \Delta T_{max}}{\rho_0 C_p T_0 g^{1/2} H^{5/2}} \quad (6.12)$$

$$v^* = \frac{v + \frac{\rho V S}{2A\rho_0}}{\sqrt{gH}}, \text{ for upstream} \quad (6.13)$$

$$v^* = \frac{\frac{\rho V S}{2A\rho_0} - v}{\sqrt{gH}}, \text{ for downstream} \quad (6.14)$$

where l^* is the smoke back-layering length, v is longitudinal velocity, V is roof ventilation velocity, ΔT_{max} is maximum smoke temperature, Q_0 is heat release rate from fire source, S is area of ceiling vent, A is tunnel cross sectional area, H represents tunnel height, C_p is specific heat of air, ρ_0 is ambient air density and ρ represents hot gas density.

Table 6.4 summarizes the smoke layering length and CFD results are compared

with theoretical model proposed in eqn [6.11]. The smoke layering length decreases for roof ventilated tunnel. In tunnel with single roof opening, with heat source located at 60.0m smoke layering length is higher towards the downstream side. However for tunnel with three roof vents, the relative deviations between upstream and downstream smoke layering length is reduced. The present CFD results are in good agreement with the proposed theoretical model.

6.4.2 Summary

The buoyancy induced turbulent flow characteristics inside naturally ventilated tunnel with roof openings are investigated numerically to understand the importance of ceiling openings in removing hot gases. The flow through the ceiling openings are bidirectional and oscillatory. For a tunnel with heat source and vent located at center, significant amount of thermal plume escapes through ceiling opening and reduces the longitudinal smoke propagation. For tunnel with centrally mounted ceiling vent, as longitudinal distance between heat source and vent varies a single naturally ventilated roof opening is insufficient to exhaust all hot gases. For tunnel with multiple openings with two heat sources, central ceiling vent is effective in removing the hot gases. The smoke temperature inside the tunnel increases with decrease in vent size. The smoke layering length decreases in roof ventilated tunnel. When heat source is located at 60.0m smoke layering length is higher towards the tunnel downstream side. The present CFD results are in good agreement with the theoretical model proposed by Chen et al., [104]. The present investigation would be useful to understand the influence of naturally vented tunnel roof openings in removing smoke and toxic gases.

Chapter 7

Wind effects on thermal plume behavior

The movement of smoke arising from fire accidents inside buildings has been a major concern since toxic gases such as carbon monoxide poses threat to human safety and environment. The ambient wind flow through openings such as doors and windows

...

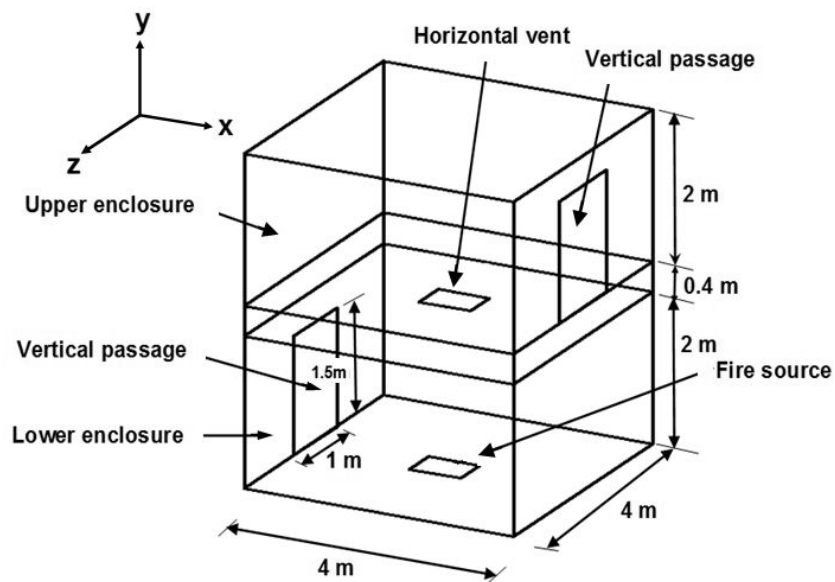


Figure 7.1: Schematic diagram of dual enclosure connected by a horizontal vent (All dimensions in m).

7.1 Problem definition

The schematic diagram of dual enclosure is shown in Fig. 7.1. The upper and lower enclosures have door openings through which pressurized ambient air propagates into the chamber. The two enclosures are 4m long, 4m wide and 2m high and are separated by ceiling obstruction of dimension $4m \times 4m \times 0.4m$. The ceiling obstruction has vent of dimension $0.4m \times 0.4m \times 0.4m$ which acts as horizontal passage in connecting dual enclosures. The left wall of lower enclosure and right wall of upper enclosure has centrally located door passages of width 1m, height 1.5m and thickness 0.2m. A heat source of square cross section $0.4m \times 0.4m$ releases heat at the rate of $1500kW/m^2$.

7.2 Results and discussions

The thermal plume characteristics with and without forced ventilations are presented and assisting or opposing effects of forced flow on thermal buoyancy force are analyzed by varying inlet velocities. Results are analyzed by changing heat source locations. Large Eddy Simulations (LES) are performed with Fire Dynamic Simulator code.

7.2.1 Effects of doorway flow with heat source placed in lower enclosure

To understand the flow characteristics through horizontal vent inside dual enclosures, investigations are performed under natural ventilation conditions by positioning a centrally located heat source in lower enclosure. The door passages in enclosures are opened to ambient atmosphere for bidirectional flow of hot and cold fluids. Figure 7.2 (a-f) characterizes the evolution of thermal plume inside dual compartment at three different time intervals. In Fig. 7.2, (a-c) represents iso-surfaces of emerging thermal plume, and (d-f) represents two-dimensional temperature contours along the xy plane at $z=2.0m$ which indicates core temperature distribution of iso-surface. It is evident from iso-surface contours that plume reaches horizontal passage at time $\tau = 2s$, propagates further into upper enclosure and impinges on roof ceiling at $\tau = 15s$. The thermal buoyancy force is significant along the normal direction and base ignition source temperature difference accelerates the plume to gain momentum to reach enclosure ceiling. It is seen from Fig. 7.2 (b) that in upper enclosure, bulk motion of hot fluid is significant along the longitudinal and lateral directions and plume spreads downwards. Fig. 7.2 (c&f) indicates that as flow progresses both compartments are filled with hot fluid, density difference increases flow resistance along the horizontal passage, and significant amount of plume leaves dual enclosures through door openings.

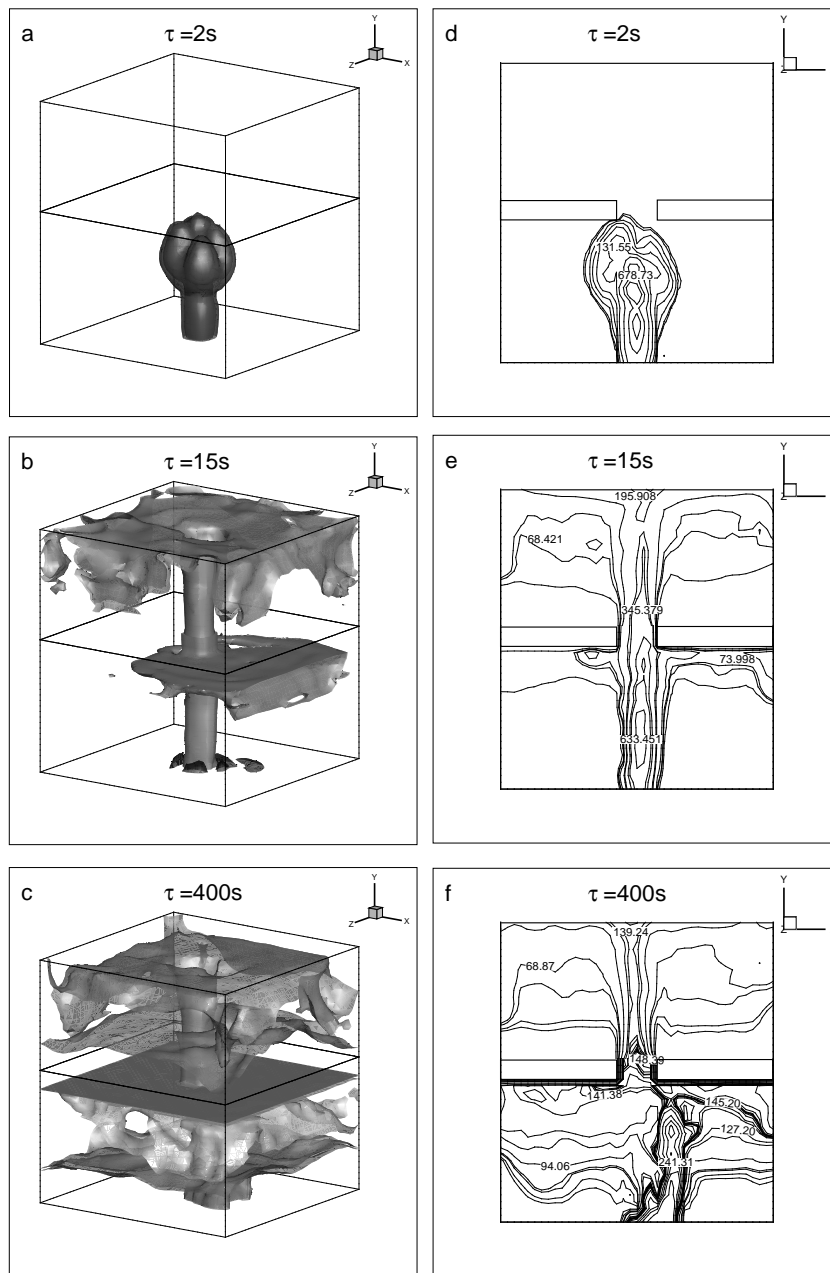


Figure 7.2: (a-c) Isosurface of thermal plume; (d-f) Evolution of temperature contours.

The flow along vertical passage is bidirectional. Significant amount of thermal plume leaves the enclosure through upper half, while ambient air is entrained into the enclosure through lower half of the opening. It is evident from Fig. 7.2 (d-f) as time evolves, substantial amount of hot gases leaves the enclosure, and entrained ambient air reduces heat from fire; hence, plume temperature decreases. It is seen from Fig. 7.2 (f) that hot gases accumulate near the ceiling of upper and lower

compartments and temperature magnitudes decreases near the lower half of the compartment. The ambient air entrains through the lower vertical passage, while flow resistance is developed along the ceiling vent as a result of back flow from upper enclosure; hence in Fig. 7.2 (f) slight tilting of thermal plume is visualized inside the lower enclosure.

7.2.2 Effects of forced air flow through lower enclosure doorway

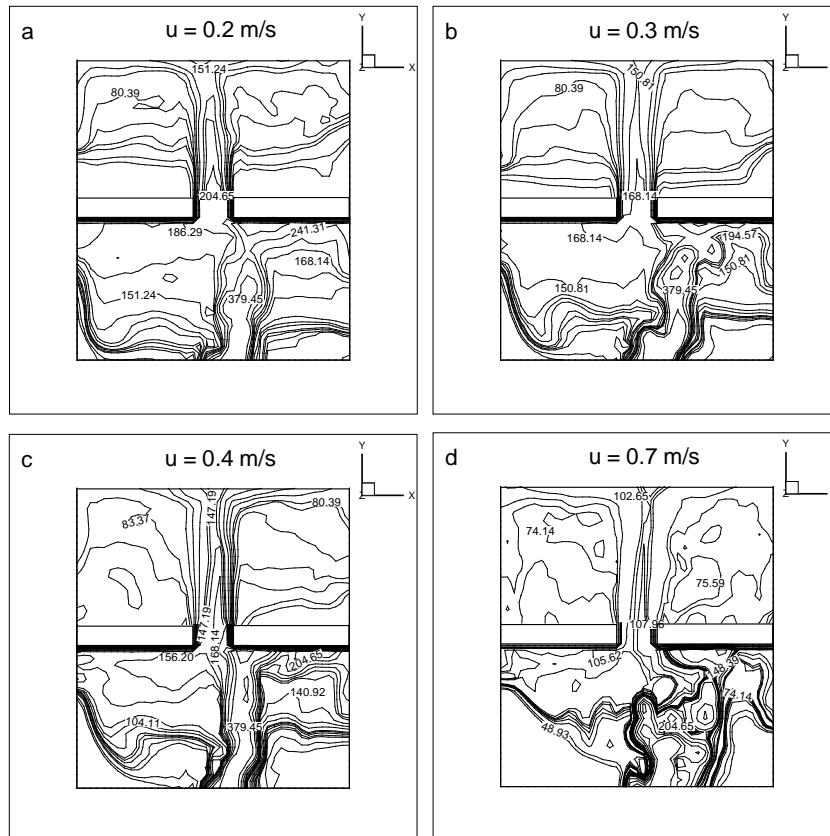


Figure 7.3: (a-d) Comparison of temperature contours for different ventilation velocities.

Simulations are performed with different inlet velocities (0.2 to 0.7m/s) to understand the influence of forced ventilation through bottom door way in affecting the flow characteristics in dual compartment enclosure. The lower compartment has a centrally located fire source, and forced air is supplied through the left wall door way. Figure 7.3 (a-d) illustrates the temperature contours at $\tau = 400s$ for different inlet velocities. It is determined that forced velocity of 0.2m/s assists the plume; hence an increase in temperature magnitude is visualized inside the dual enclosure. However from Fig. 7.3 (b&c), with increase in inlet velocities, significant amounts of

cold air enter into the enclosure; hence slight decrease in temperature magnitudes are visualized near the lower compartment left wall, horizontal passage and upper enclosure. From illustration shown in Fig. 7.3 (d), it is evident that forced ambient inlet of 0.7 m/s creates more turbulence inside the lower enclosure, and tilts the plume towards right wall and carries away heat thereby reducing temperature intensity inside the dual enclosures.

Figure 7.4 (a&b) represents the net mass flow rate through horizontal passage and upper enclosure door way. It is visualized from Fig. 7.4 (a&b) that with increase in inlet velocities bulk quantity of fluids are transferred through horizontal passage into the upper enclosure and are vented into the ambient media through upper enclosure door way passage. Table 7.1 summarizes the average mass flow rate through openings and average plume temperature inside the enclosures. The average plume temperatures inside the upper and lower enclosures are determined by measuring the temperature distribution along the vertical centerline of compartments. The average mass flow rates increases linearly with forced inlet velocities. Even though the net quantity of fluid flowing through the horizontal passage is higher, substantial decrease in temperature magnitudes are visualized inside enclosures.

Table 7.1: Average mass flow rate and plume temperature for forced inlet velocities through lower enclosure doorway

Inlet velocity (m/s)	Horizontal vent mass flow rate (kg/s)	Top doorway mass flow rate (kg/s)	Lower enclosure plume temperature (°C)	Upper enclosure plume temperature (°C)
0.2	0.45	0.38	308.25	170.58
0.3	0.61	0.54	316.74	183.62
0.4	0.78	0.71	302.21	165.53
0.5	0.95	0.83	281.76	146.15
0.6	1.18	1.06	250.68	121.37
0.7	1.45	1.32	223.05	105.46

7.2.3 Effects of forced air flow through upper enclosure doorway

The illustrations shown in Fig. 7.5 (a-f) represents the effects of forced ventilation through upper enclosure door way passage for different inlet velocities. The lower compartment door way is naturally ventilated and heat source is located at the center of bottom enclosure. Figure 7.5 (a&b) indicates the evolution of temperature

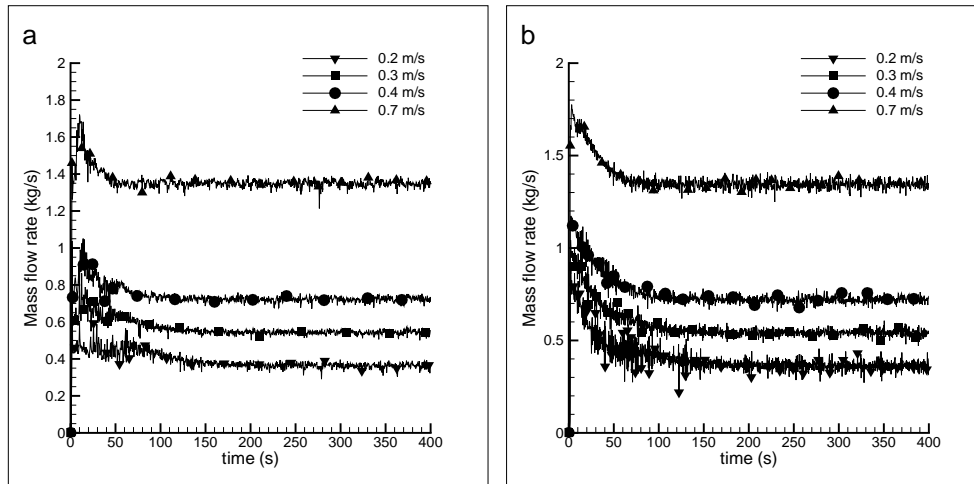


Figure 7.4: (a) Mass flow rate through horizontal opening; (b) Mass flow rate through top enclosure door-way.

contours for inlet velocity 0.2m/s. The forced air stream travels from the right wall in the upper enclosure and creates resistance across the horizontal passage and restricts the entry of thermal plume into upper enclosure. During the initial fire propagation stage at $\tau = 60s$, thermal plume overcomes the air stream and advances into upper enclosure; hence temperature magnitude increases slightly near the horizontal passage and ceiling. As flow progresses, at $\tau = 400s$ the forced flow builds pressure inside upper enclosure and air stream enters lower enclosure and distorts the shape of plume, and a significant quantity of hot fluid is vented through bottom door way passage.

Figure 7.5 (c&d) depicts the time evolution of temperature contours for velocity 0.3m/s. In comparison with Fig. 7.5 (a&b) it is seen that with increase in inlet velocity, propagation of plume through horizontal vent decreases; hence the upper compartment temperature distribution decreases. At time $\tau = 60$, the air stream tilts the plume axis towards the left side of the enclosure while an opposite trend is observed at later time $\tau = 400$. At later time the plume is confined along the right half of the lower enclosure, and in comparison with Fig. 7.5 (b&d) it is determined that at higher velocities the forced air stream reduces the heat intensity and removes hot gases through the lower enclosure vertical passage. Figure 7.5(e) represents the normal velocity contours, the positive and negative magnitude represents the plume and air stream velocities. It is visualized that the concentrations of thermal plume are near the right portion of the compartment and air stream enters through the horizontal passage and is concentrated near the left half of the enclosure. Figure 7.5 (f) illustrates the isosurface temperature distribution and it is evident that the

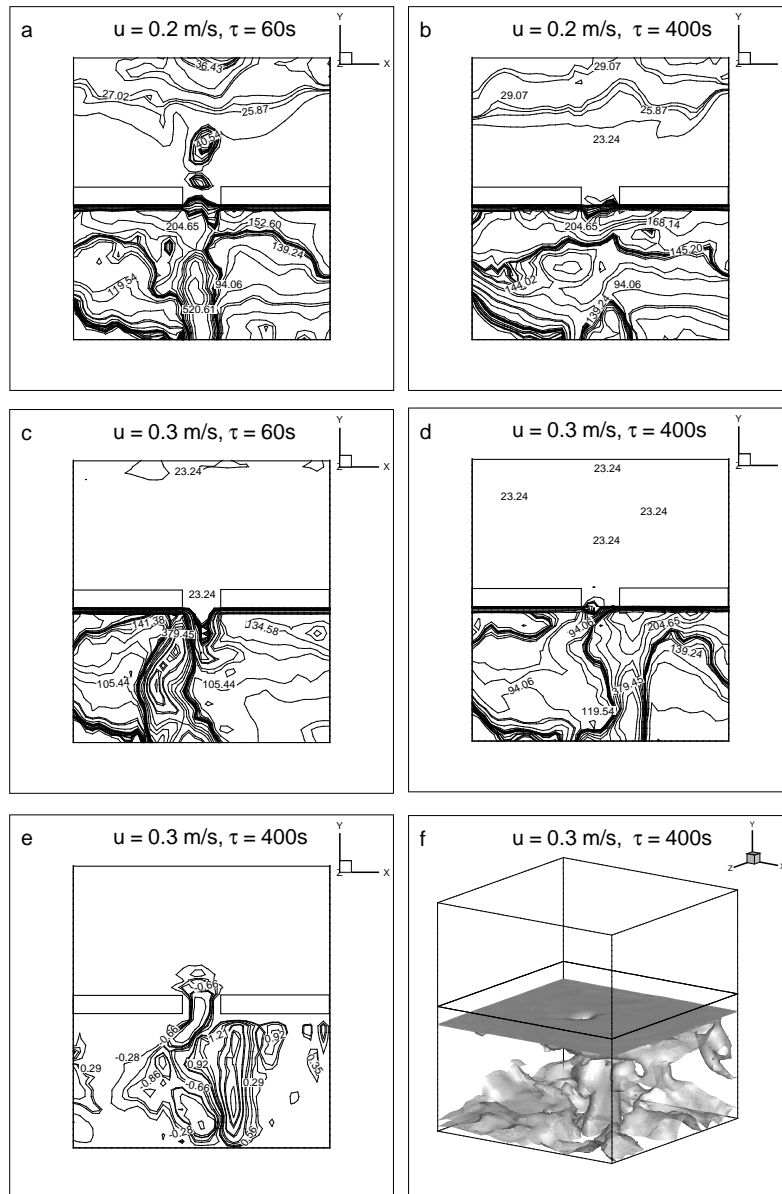


Figure 7.5: (a-d) Comparison of temperature contours for different ventilation velocity; (e) Normal velocity contours; (f) Isosurface of thermal plume.

inflow directions of forced ventilations have significant effect on thermal buoyancy force and affects the fire flow characteristics in dual enclosure.

Figure 7.6 (a&b) represents the net mass flow rate through horizontal vent and lower enclosure door way passage. The negative magnitude in Fig. 7.6 (a) indicates the inflow of air stream, while in Fig. 7.6 (b) the outflow of hot fluid are represented with negative magnitudes. Table 7.2 indicates the average mass flow rates and plume temperature inside the enclosures. It is evident that with increase in inlet

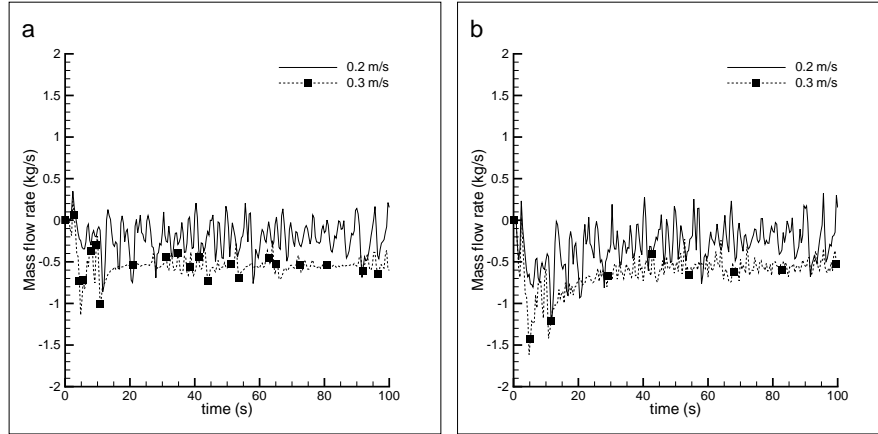


Figure 7.6: (a) Mass flow rate through horizontal opening; (b) Mass flow rate through bottom door way.

velocities, plume flow rate through bottom doorway increases, meanwhile plume temperature inside lower enclosure gradually decreases.

Table 7.2: Average mass flow rate and plume temperature for forced inlet velocities through upper enclosure doorway

Inlet velocity (m/s)	Horizontal vent mass flow rate (kg/s)	Bottom doorway mass flow rate (kg/s)	Lower enclosure plume temperature ($^{\circ}\text{C}$)	Upper enclosure plume temperature ($^{\circ}\text{C}$)
0.2	-0.28	-0.58	280.48	45.83
0.3	-0.75	-0.97	220.72	32.67
0.4	-1.21	-1.45	200.35	25.14

7.2.4 Forced air flow through upper enclosure doorway with heat source placed in upper enclosure

To understand the effects of forced ventilation from upper compartment door way opening, investigations are carried out by placing heat source inside the top compartment. The heat source is placed at two different locations 1m and 3m measured from the left wall. Forced air with inlet velocities 0.2 to 0.4m/s are supplied through upper compartment door-way opening, meanwhile the lower compartment door way passage is naturally ventilated. Figure 7.7 (a-f) illustrates the isosurface temperature distribution, velocity and temperature contours for two different heat source locations with forced inlet velocity 0.4m/s. The isosurface contours for heat source placed at 1m is depicted in Fig. 7.7 (a), and it indicates that thermal plume approaches the compartment ceiling and spreads inside the

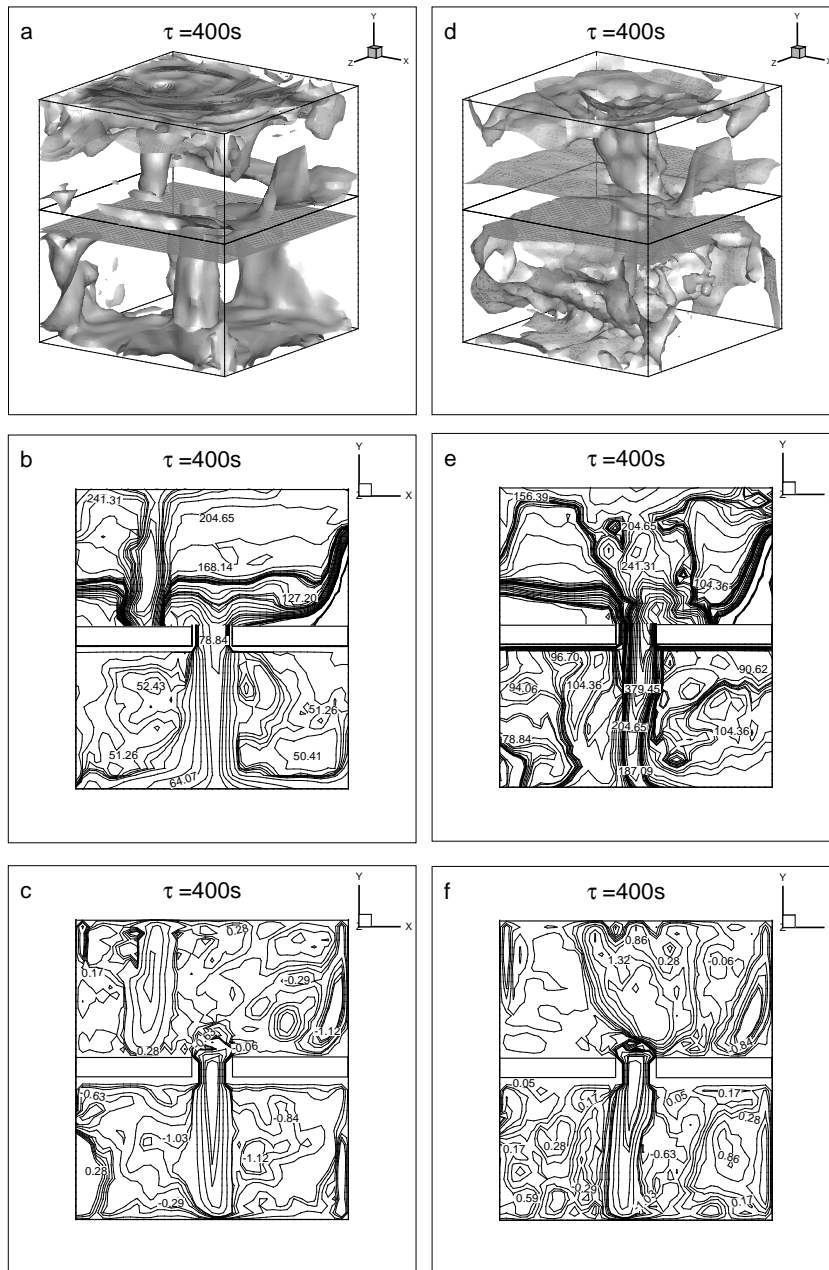


Figure 7.7: Comparison of results for two different heat source locations: (a,d) Isosurface of thermal plume; (b,e) Temperature contours; (c,f) Normal velocity contours.

upper enclosure. Meanwhile the forced air stream from right opening builds pressure inside the upper enclosure, and ample amount of hot fluids are forced into the lower enclosure through the horizontal passage as seen in Fig. 7.7 (a). The temperature contours depicted in Fig. 7.7 (b) highlights that forced flow diffuses the heat from the upper compartment and transmits the heat by impinging hot fluid into the lower compartment.

The forced inlet affects the thermal buoyancy force in upper compartment and drives the plume to travel in the direction opposite to buoyancy force. The corresponding normal velocity contours are shown in Fig. 7.7 (c). The positive magnitudes in upper compartment represents the plume velocity and negative magnitudes in lower compartment illustrates that forced air stream carries away the heat from the upper compartment into the lower compartment, and are vented through the left door way passage. Figure 7.7 (b) shows the isosurface contours for heat source located at 3m, and when compared to Fig. 7.7 (a) it is evident that more hot fluid is transferred into the lower compartment since fire source is located near the forced inlet passage. From the corresponding temperature contours shown in Fig. 7.7 (e) it is determined that an immense amount of hot fluid enters the lower enclosure, and temperature magnitudes increases significantly in comparison with Fig. 7.7 (b). From the normal velocity contours depicted in Fig. 7.7 (f) it is seen that concentrations of plume velocity are higher inside lower enclosure since additional inflow of hot fluid increases the turbulence mixing process.

Table 7.3: Average mass flow rate and plume temperature for fire source located at 1.0m inside upper enclosure with forced flow through upper enclosure doorway

Inlet velocity (m/s)	Horizontal vent mass flow rate (kg/s)	Bottom doorway mass flow rate (kg/s)	Lower enclosure plume temperature (°C)	Upper enclosure plume temperature (°C)
0.2	-0.31	-0.38	44.27	262.58
0.3	-0.44	-0.47	52.19	228.74
0.4	-0.54	-0.59	65.22	215.31

Table 7.4: Average mass flow rate and plume temperature for fire source located at 3.0m inside upper enclosure with forced flow through upper enclosure doorway

Inlet velocity (m/s)	Horizontal vent mass flow rate (kg/s)	Bottom doorway mass flow rate (kg/s)	Lower enclosure plume temperature (°C)	Upper enclosure plume temperature (°C)
0.2	-0.37	-0.44	96.57	240.16
0.3	-0.51	-0.56	138.14	210.53
0.4	-0.68	-0.83	180.18	193.14

Figure 7.8 (a&b) indicates the horizontal passage center point temperature and normal velocity variations with time, and for heat sources located at 3m more hot fluid is transmitted into the lower enclosure; hence the temperature and normal velocity variations are higher with time evolution. Figure 7.8 (c) illustrates the temperature variation with time at the center of lower enclosure vertical passage,

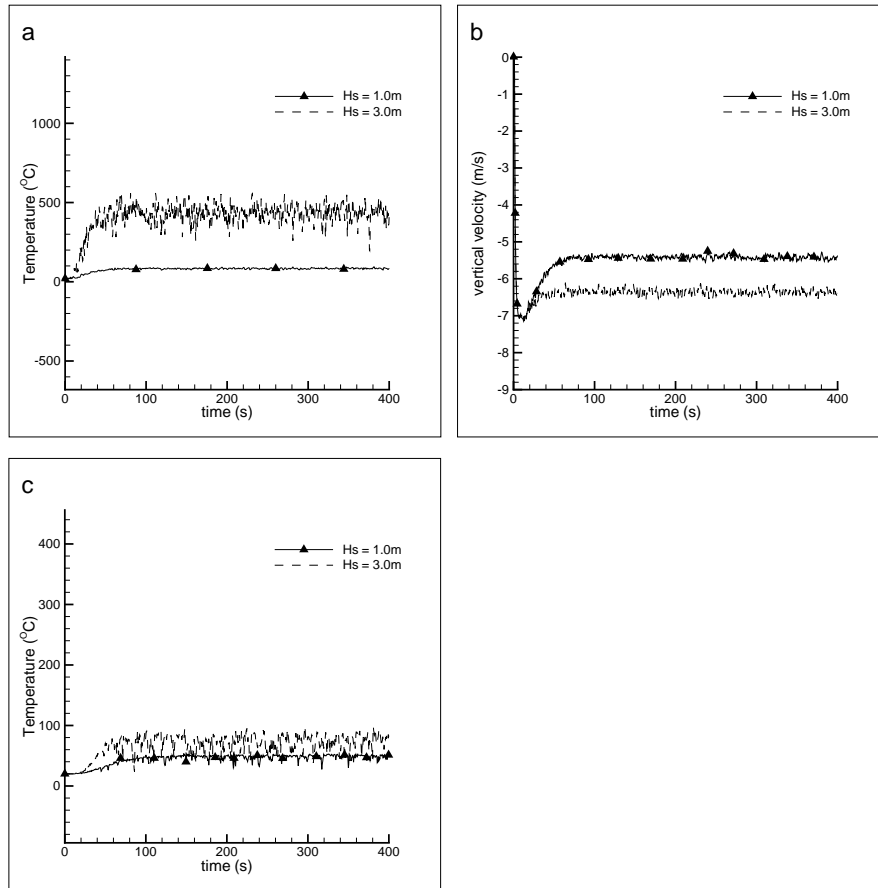


Figure 7.8: (a) Horizontal vent center point temperature variation; (b) Horizontal vent center point normal velocity variation; (c) Lower enclosure door way center point temperature variation.

and temperature magnitudes are higher for heat source placed at 3m. Table 7.3 & 7.4 indicates the flow rates and enclosure temperatures for heat source located at 1.0m & 3.0m. The net mass flow rate through openings and lower enclosure plume temperature are higher for heat source located near top enclosure doorway at 3.0m.

7.2.5 Summary

The buoyancy induced flow characteristics in dual enclosures connected through horizontal passage are investigated numerically under forced and naturally ventilated conditions. The assisting or opposing behavior of forced air stream on thermal buoyancy force is studied by varying the heat source locations and inlet velocities. In naturally ventilated dual enclosures, isosurface contours suggest that buoyancy force drives the plume through horizontal passage to reach enclosure ceiling, and initial movement is significant along normal direction. The oscillatory exchange flow through door way passages are bidirectional. The low forced

ventilation velocity ($u \leq 0.4m/s$) through lower enclosure door-way promotes plume growth rate, while higher velocities diffuses heat intensity and reduces the compartment temperature. It is determined that forced flow from upper enclosure restricts free flow of thermal plume and opposes upward buoyancy force. When heat source location is shifted to upper enclosure under natural ventilation conditions, the buoyancy force prevents the downward movement of plume into lower enclosure. The forced air stream from upper compartment door-way, guides the thermal plume evolving from top compartment to propagate into lower compartment and significantly affects fire transport phenomena. The present investigation would be useful to understand assisting and opposing effects of forced ventilation in spreading smoke and toxic gases during fire accidents.

Chapter 8

Water spray interaction with thermal plume

The smoke vents and sprinkler systems are the major fire safety measures in buildings to remove toxic gases and to reduce heat released from fire accidents. When automatic sprinkler fails to activate, smoke vent plays a crucial role by discharging hot combustion gases and improves visibility for safe evacuation of building occupants. However there are concerns about the performance of smoke vents under water sprays, since drag force from falling water droplets opposes smoke buoyancy force and affects discharge rate through vents. This chapter investigates the effects of water droplets in affecting plume characteristics under natural and forced ventilation conditions.

8.1 Problem definition

The physical model shown in Fig. 8.1 consists of a two compartmental enclosure connected to adjacent tall vertical shaft. The two enclosures are connected internally through a ceiling vent. Numerical investigations are performed in a two compartmental enclosure connected to tall shaft. The horizontal vent and doorway openings facilitate fire driven flow from lower enclosure to propagate into upper enclosure and tall shaft. The two rectangular enclosures are 4m long, 4m wide and 2m high and are connected to an adjacent vertical shaft of dimension $0.8m \times 1.2m \times 10m$. The two compartments are separated by ceiling obstruction and horizontal vent of dimension $0.4m \times 0.4m \times 0.4m$ is located centrally. The enclosures are fitted with 3 doorway passages of width 1m, height 1.5m and thickness 0.2m. The lower enclosure consists of a water spray sprinkler system (Sp1), which is installed at 1.9m above the floor, 3m away from left wall and

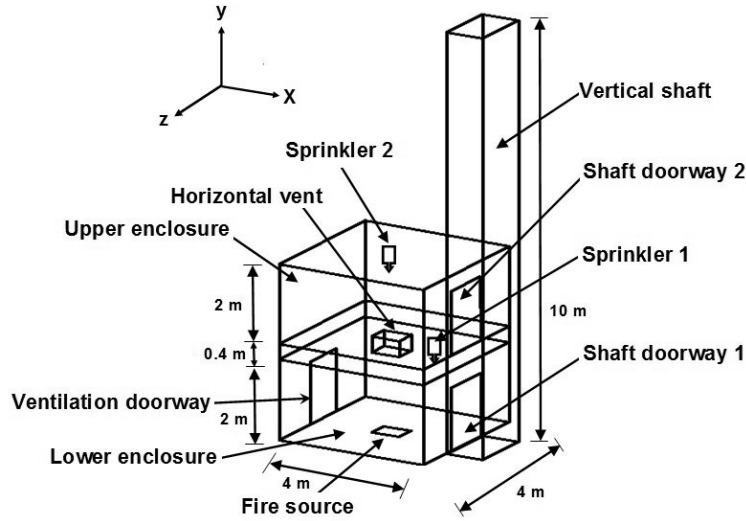


Figure 8.1: Schematic diagram of dual enclosure connected by a horizontal vent (All dimensions in m).

positioned near the shaft doorway1. Similarly the upper compartment ceiling has a centrally located sprinkler system (Sp2), which is installed directly above the horizontal vent. In lower compartment a centrally located fire source of square cross section $0.4m \times 0.4m$ releases heat at the rate of $1500kW/m^2$. The vertical temperature distribution are measured by three thermocouple trees. The lower and upper enclosures are installed with Thermocouple trees 1 &2. It consists of 8 thermocouples each, located centrally at $x=2.0m$, separated by vertical distance of $0.25m$. Thermocouple tree 3 consists of 20 thermocouples placed along the vertical centerline of shaft to measure the temperature variation with height.

8.2 Results and discussions

The preliminary investigations are performed to analyze plume transport phenomena without activating water spray systems. The subsequent simulations are carried out under the action of water sprays by varying flow rates and operating pressure. Moreover the complex interactions between smoke layer and water particles are analyzed by supplying forced air through lower enclosure left doorway opening. Large Eddy Simulations (LES) are performed with Fire Dynamic Simulator code.

8.2.1 Fire transport phenomena without activating water spray system

Figure 8.2 (a-f) characterizes the evolution of fire driven thermal plume inside dual enclosures and adjacent shaft. The thermal plume reaches horizontal passage at time $\tau = 2s$, propagates into upper enclosure and impinges on the roof ceiling, further spreads longitudinally ($\tau = 15s$). The thermal buoyancy force is significant along normal direction and base ignition source accelerates the plume to gain momentum. Density difference arises between hot and ambient fluids present inside the enclosures and across door openings. The plume leaves the lower enclosure through the naturally ventilated left doorway passage. As the flow progresses, significant quantity of hot fluid migrates into the shaft through right doorway openings ($\tau = 25 - 50s$). The shaft side walls restrict the plume horizontal movement and are transformed as wall plume.

Figure 8.3 (a) indicates isosurface of fire plume with complex flow structure and swirl flow patterns across the core region of vertical shaft. Figure 8.3 (b) quantifies variation of mass flow rate across the openings. The flow patterns through openings are oscillatory. The outflow of hot fluid through horizontal vent, shaft doorways 1&2 are represented with positive magnitudes, meanwhile negative magnitudes indicates inflow of entrained air or backflow through these openings. However across the lower enclosure left ventilation doorway, positive and negative magnitudes represent the ambient and hot fluid flow rates respectively. Significant quantity of hot fluid leaves the lower enclosure through the horizontal vent and ventilation doorway. The discharge rate through shaft doorway1 illustrates combination of entrainment and backflow from vertical shaft into the lower enclosure.

8.2.2 Effects of water sprays on fire transport phenomena

Table 8.1: Sprinkler operating conditions

S.No	Flow rate (l/min)	Operating pressure P_d (bar)	Mean droplet diameter (μm)	Initial droplet velocity (m/s)
1	30	1.0	828	5.58
2	40	1.2	779.17	6.11
3	50	1.4	740.15	6.6
4	60	1.6	708	7.05

The temperature distribution after the activation of water spray systems (Sp1&Sp2) are shown in Fig. 8.4 (a-d). The sprinklers are activated after $\tau = 15s$ from fire ignition. The water flow rates are varied from 30-60 l/min as shown in Table 8.1.

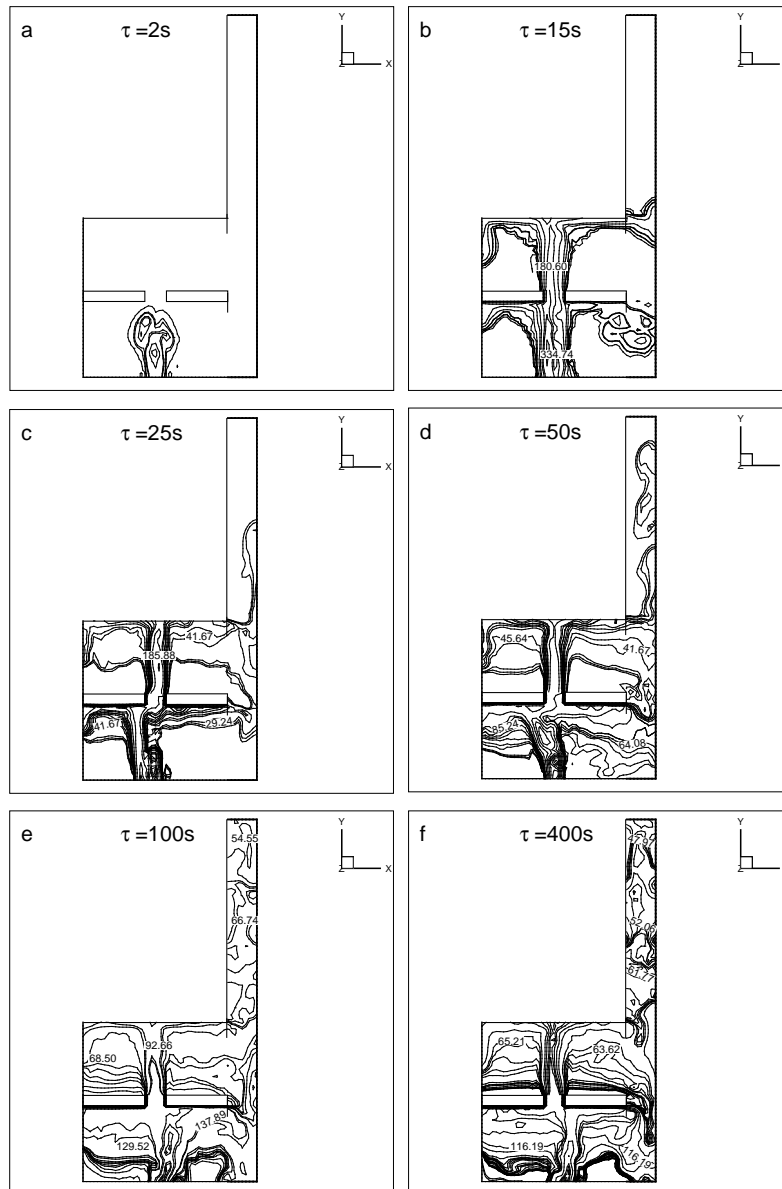


Figure 8.2: (a-f) Evolution of temperature contours.

The temperature field decreases apparently with sprinkler activation. The complex temperature patterns illustrate the interactions between water droplets and thermal plume. The cooling and drag effect of water particles opposes smoke buoyancy force and decreases the plume temperature. The drag force depends on the water flow rate and velocity of water particles. Hence with increase in sprinkler operating pressure the drag force increases. For sprinkler flow rate of 30 l/min, the buoyancy force is greater than drag force and significant quantity of hot fluid propagates into the upper enclosure and vertical shaft. However as the sprinkler flow rate and operating pressure increases, the vertical momentum of thermal plume decreases

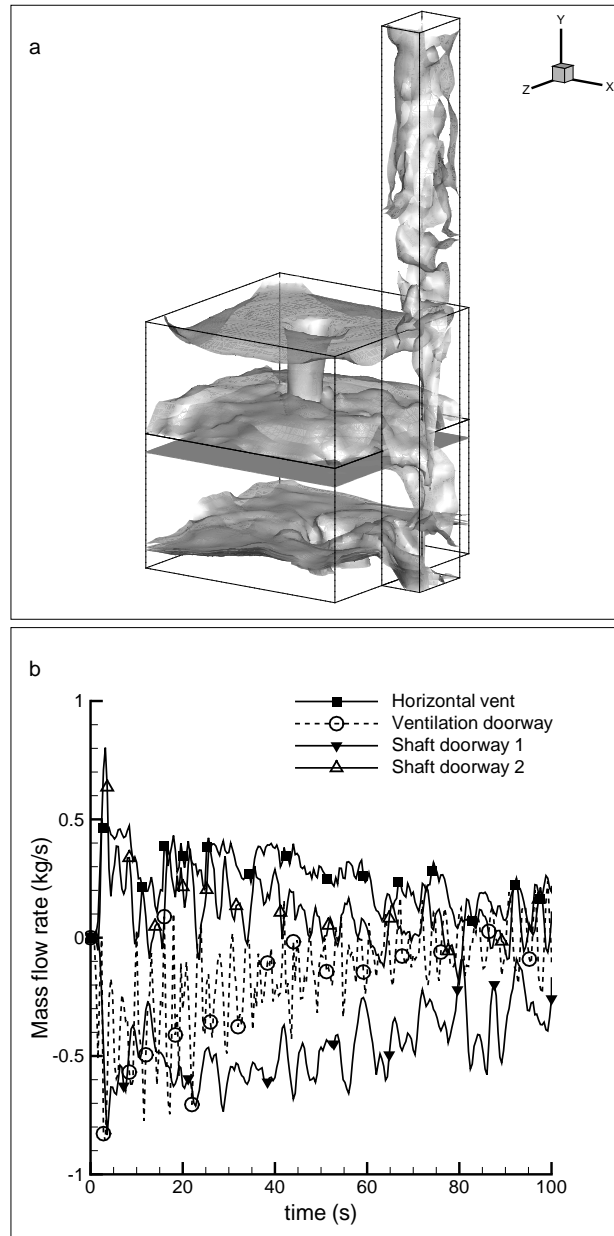


Figure 8.3: (a) Isosurface of thermal plume; (b) Variation of net mass flow rate.

and smoke layer turns unstable. For water flow rate of 40-50 l/min, the buoyancy force reduces and temperature magnitudes inside the upper enclosure and shaft decreases substantially. The peak temperature inside the upper enclosure is reduced to 34°C. It is interesting to note from Fig. 8.4 (d) that spray drag force pulls the smoke layer downwards and restricts the plume discharge through horizontal vent. When sprinkler operating pressure is higher than smoke venting velocity, drag force dominates the buoyancy force. Hence smoke could not flow out through horizontal vent and leads to smoke logging. This further increase the risk on human evacuation

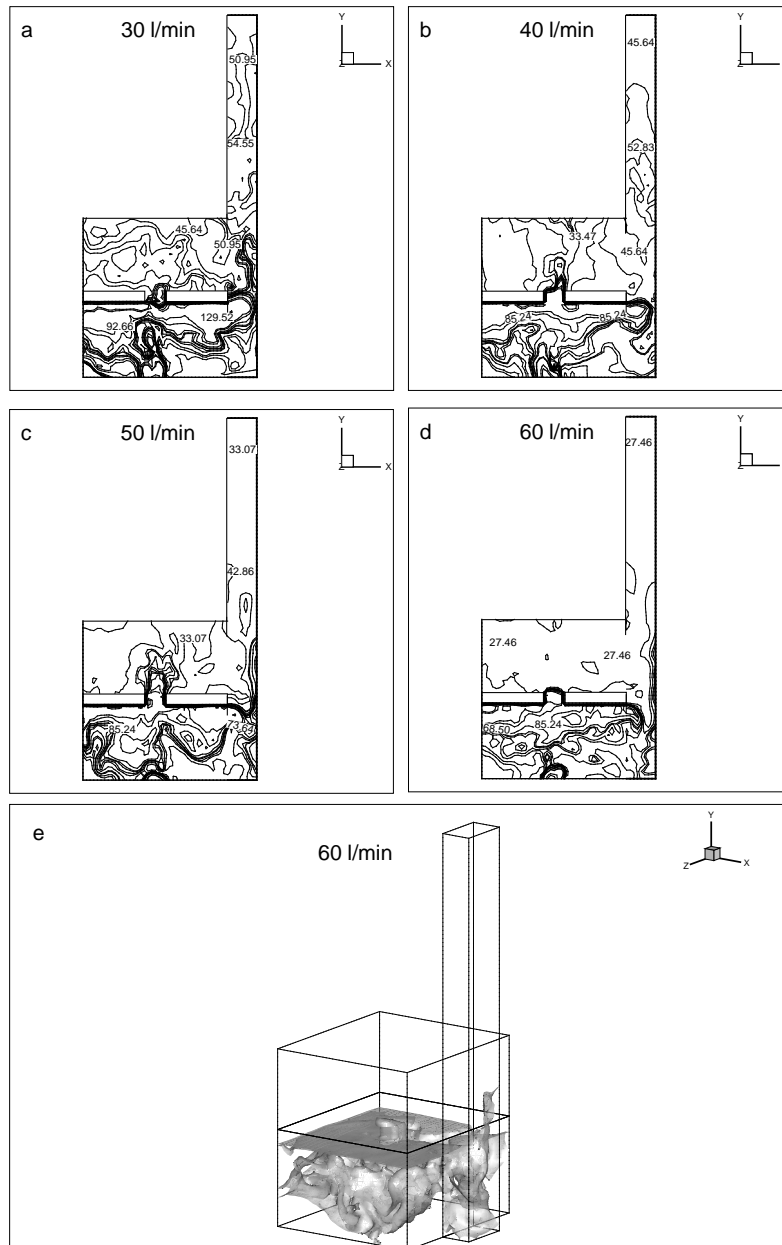


Figure 8.4: (a-d) Comparison of temperature contours for different sprinkler discharge rates; (e) Isosurface of thermal plume.

since the smoke moves downwards and accumulates near the compartment floor. The sprinkler operating pressure at which smoke logging occurs is called initial logging pressure. Moreover sprinkler spray (Sp1) acts as water curtain, reduces the plume horizontal momentum and decreases hot fluid discharge into shaft doorway1. The isosurface patterns in Fig. 8.4 (e) illustrates smoke logging situation inside the lower compartment.

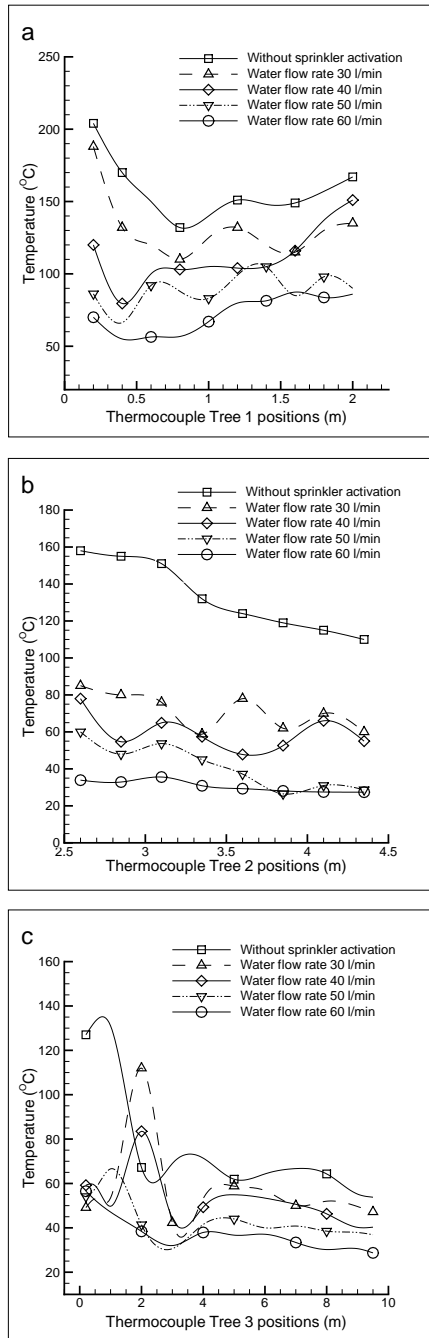


Figure 8.5: Temperature distribution inside (a) lower compartment; (b) Upper compartment; (c) tall shaft.

Figure 8.5 (a-c) indicates the temperature profile measured by thermocouple trees 1-3. In Fig. 8.5 (a) for base case without water sprays, the maximum temperature magnitudes are near the fire source and ceiling. The hot gases accumulate near the ceiling due to buoyancy. The maximum ceiling temperature recorded is 170 °C. The temperature magnitude decreases gradually after sprinkler

activation. For flow rates above 40 l/min, the cooling and drag effect moves the hot plume layer downwards and temperature magnitudes recorded in the compartment middle layer is closer to the ceiling and heat source temperatures. The temperature deviations further decreases and the average temperature is reduced to 75 °C for flow rate of 60 l/min.

In Fig. 8.5 (b) peak temperature between the base case and sprinkler flow rate of 40 l/min decreases drastically from 160 °C to 85 °C. This is due to weakening of buoyancy force as plume propagates through horizontal vent and comes in direct contact with water droplets. As sprinkler operating pressure increases, pressure difference across the horizontal vent decreases. This further reduces plume discharge rate and decreases the temperature magnitude. However sprinkler operating pressure of 1.6 bar, flow rate 60 l/min eventually blocks the entry of hot gas into the upper enclosure. This is visualized from the relatively constant temperature profile and temperature magnitude is reduced to 35 °C. The sprinkler pressure of 1.6 bar is the initial logging pressure and leads to smoke logging. In Fig. 8.5 (c), the maximum temperature distribution inside the shaft is higher near the doorway1 and reduces as the vertical distance increases. For sprinkler flow rate of 30-40 l/min, temperature magnitude increases by 20 – 40 °C near the shaft doorway1. This is due to an increase in the plume horizontal momentum under sprinkler sprays (Sp1).

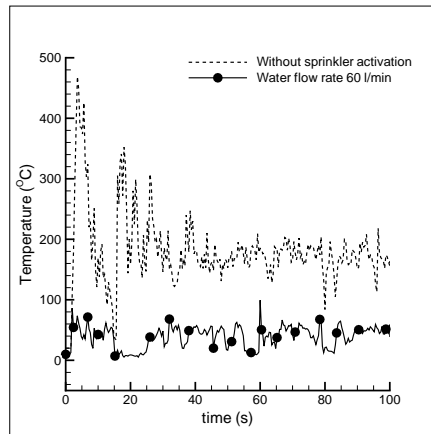


Figure 8.6: Horizontal vent center point temperature variations.

The variation of horizontal vent center point temperature distribution is plotted in Fig. 8.6. It is shown that the temperature fluctuation decreases significantly under water spray system. The average vent temperature measured without activating sprinkler is 173 °C and is reduced to 40 °C with sprinkler flow rate of 60

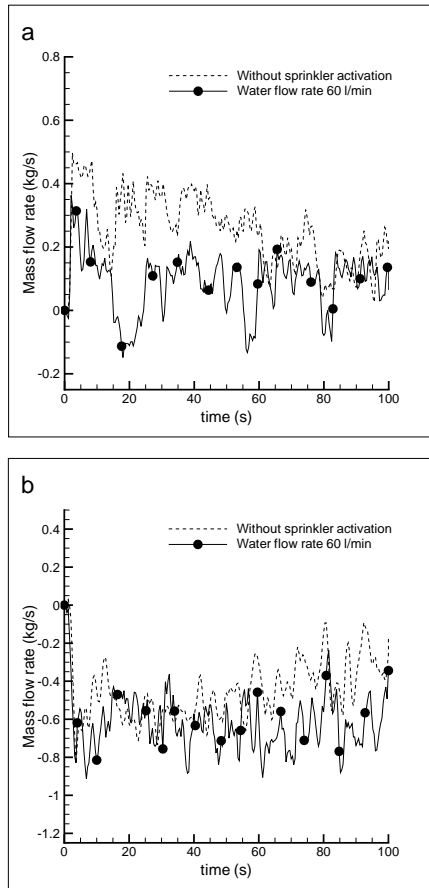


Figure 8.7: (a) Mass flow rate through horizontal opening; (b) Mass flow rate through shaft doorway1.

l/min. Figure 8.7 (a&b) illustrates the mass flow rates through horizontal vent and shaft doorway 1 and results are compared for cases with and without water sprays. The smoke venting velocity decreases apparently under water sprays. However from Fig. 8.7 (a&b), the effect of drag force is significant on plume vertical momentum when compared to the reduction in horizontal momentum. The mass flow rate across the horizontal and shaft doorway1 reduces by 59.46% and 20.85% respectively with sprinkler flow rate of 60 l/min.

Table 8.2: Average fire plume temperature for different water discharge rates

Sprinkler flow rate (l/min)	Lower enclosure (°C)	Upper enclosure (°C)	Shaft (°C)
0.0	156.8	133.5	80.4
30	131	71.2	56.5
40	112	59.6	52.6
50	89.3	41.3	44.2
60	72.3	30.7	38.4

The average thermal plume temperature inside the upper, lower compartment

and shaft are summarized in Table 8.2 for different sprinkler flow rates. The temperature decrease is linear to the sprinkler flow rates.

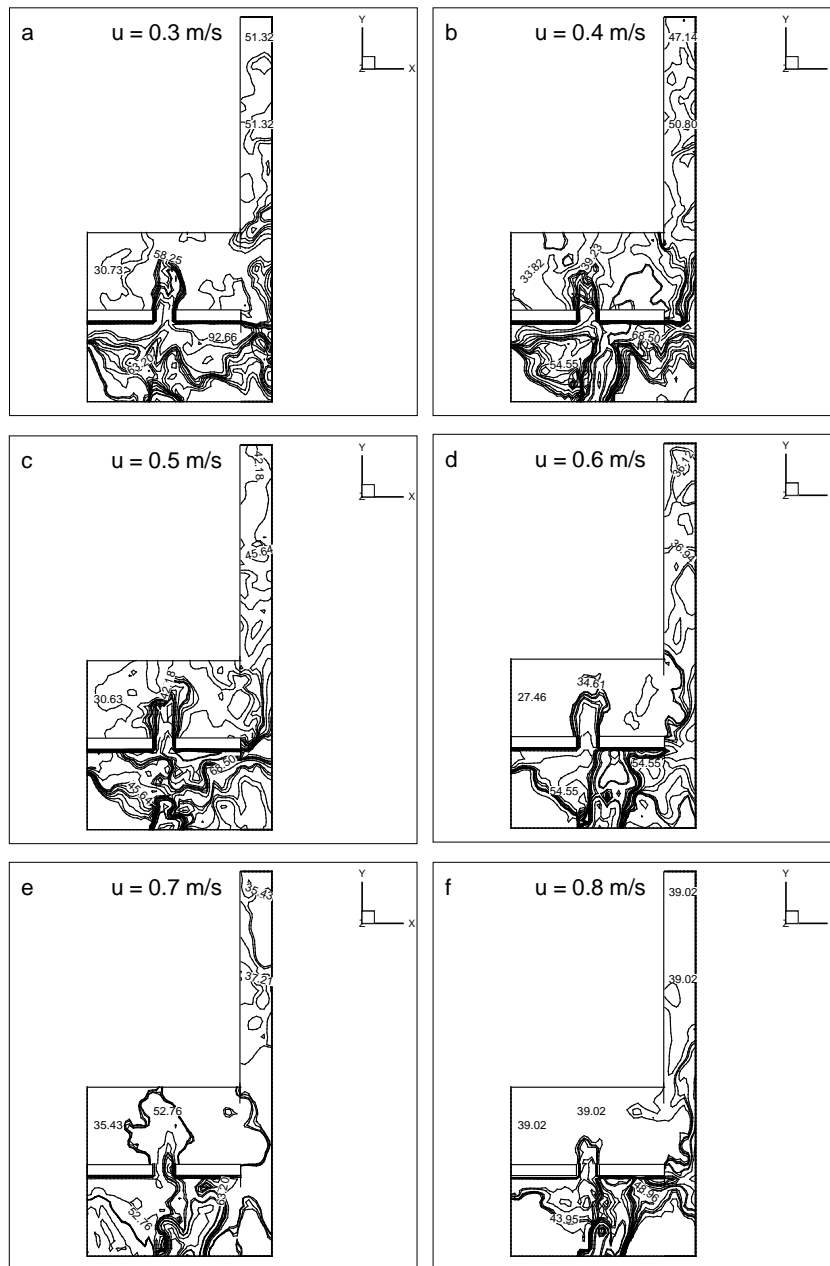


Figure 8.8: (a-f) Comparison of temperature contours for different inlet velocities.

8.2.3 Effect of forced air flow on thermal buoyancy and sprinkler drag force

Forced air is supplied through the lower enclosure ventilation doorway and sprinkler flow rate is maintained at 60 l/min with operating pressure of 1.6 bar. The forced inlet velocities are varied from 0.3-0.8 m/s. Figure 8.8 represents the temperature contours for different inlet velocities. The forced air stream strengthens the thermal buoyancy force and assists the plume to overcome the water drag force. Significant quantity of hot fluid propagates into the upper enclosure and vertical shaft. Hence smoke logging is not visualized inside the enclosures. The discharge rate through horizontal and doorway openings increases linearly with the inlet velocities. The inlet velocities $u=0.3-0.5\text{m/s}$ intensifies the plume vertical and horizontal momentum and increases the plume temperature. For inlet velocities above $u > 0.5$ m/s, the heat loss from plume to water particles eventually increases. Even though air stream opposes drag force, it intensifies the cooling effect by increasing the interactions between water droplets and hot fluid.

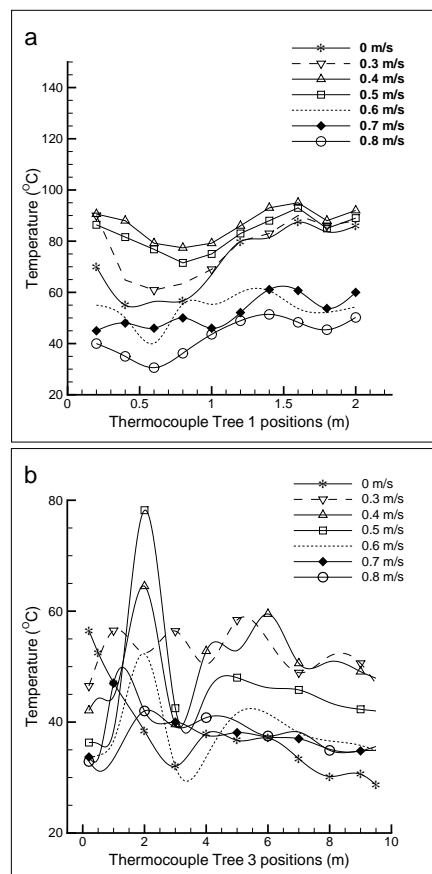


Figure 8.9: Temperature distribution inside (a) lower compartment; (b) tall shaft.

Figure 8.9 (a&b) represents the temperature profile measured by thermocouple trees 1&3. Figure 8.9 (a) shows a substantial increase in temperature magnitudes till $u \leq 0.5\text{m/s}$. A further increase in inlet velocity $u > 0.5\text{m/s}$ increases the horizontal momentum and tilts the thermal plume towards the sprinkler head (sp1). Hence the buoyancy force weakens due to cooling effect and temperature decreases. In Figure 8.9 (b) for $u=0.3-0.5\text{ m/s}$, the shaft lower portion temperature rises by $20 - 40^\circ\text{C}$. For $u=0.3-0.4\text{ m/s}$ the temperature magnitudes rises by $20 - 25^\circ\text{C}$ near the midheight of shaft since the plume discharge through shaft doorway2 increases. With further increase in $u > 0.5\text{m/s}$, the ambient air stream and water droplets diffuses the plume temperature and heat loss increases gradually.

Table 8.3: Average fire plume temperature for sprinkler flow rate 60 l/min with different inlet velocities

Inlet velocity (m/s)	Lower enclosure ($^\circ\text{C}$)	Upper enclosure ($^\circ\text{C}$)	Shaft ($^\circ\text{C}$)
0.0	72.3	30.7	38.4
0.3	73	61.9	52.1
0.4	76.2	45.2	49.9
0.5	67.3	51.7	45.4
0.6	53.7	40.2	37.6
0.7	52.3	45.6	37.6
0.8	43	37.9	36.7

Table 8.3 summarizes the average temperature distribution inside the two room enclosure and shaft with different inlet velocity. The temperature increases linearly till $u \leq 0.5\text{m/s}$ and substantially decreases for higher velocities.

8.3 Summary

The fire driven flow characteristics under water sprays is numerically studied in two room enclosure attached to adjacent shaft. The analysis is performed under forced and natural ventilation conditions. As water discharge rate increases (50-60 l/min), drag force reduces plume vertical momentum and hot gases accumulate near the compartment floor. Sprinkler operating pressure of 1.6 bar causes smoke logging inside the lower compartment. Water discharge rate of 60 l/min reduces horizontal vent mass flow rate by 59.46%. The temperature inside the compartments decreases linearly with sprinkler operating pressure. Forced ventilation velocities $u=0.3-0.5\text{ m/s}$ assists the buoyancy force and increases the plume propagation rate. Meanwhile inlet velocities $u=0.6-0.8\text{ m/s}$ diffuses plume temperature, intensifies cooling effect by enhancing the water spray interactions with fire plume. Present

results will benefit fire safety evaluation of natural smoke vents in buildings under the influence of sprinkler sprays and external wind.

Chapter 9

Conclusions

In this thesis, numerical investigations were performed to study the thermal plume behavior in ceiling vented enclosures and buoyant flows in vertical shaft within the frame work of Boussinesq approximation. The flow through ceiling vent is oscillatory due to buoyancy effects. As Grashof number is varied from $Gr = 10^8$ to 10^{10} , turbulence intensity increases and infiltration rate rises through horizontal vent. For centrally located ceiling vent, thermal plume spreading rate from heat source located at $0.5H$ is higher, in comparison with near wall heat source ($0.25H$ & $0.75H$). It is identified that ceiling vent and heat source locations are important parameters for growth and propagation of thermal plume. The vent discharge rate reduces by increasing the vent thickness from $0.1H$ to $0.2H$. This also decreases the normal velocity and temperature profiles across horizontal vent.

In case of rectangular compartment connected to vertical shaft, multi-recirculating convective cell patterns are visualized due to the interactions between hot and cold fluids. The vertical passage height ($H_v=0.05H$ & $0.1H$) reduces plume discharge rate through vertical opening and decreases the temperature distribution inside shaft. In rectangular compartment, for $Gr = 10^{10}$ with centrally located ceiling vent, significant amount of hot fluid leaves the enclosure through ceiling vent and thermal plume intensity is reduced inside vertical shaft. Hence ceiling vent is preferred for effective removal of plume from rectangular enclosure. By shifting compartment location, buoyancy force drives thermal plume towards shaft upper portion and plume transport phenomena changes significantly.

In case of buoyancy induced flows between two enclosures filled with hot and cold fluids, critical Grashof number is identified as 10^7 and further rise in Gr induces flow instabilities. The buoyancy driven mixing develops a new vortex pattern across the

horizontal passage and it evolves in cyclic pattern. The flow pattern through horizontal passage is stable for reduced vent width $D=0.05H$ and bidirectional exchange between the enclosures decreases. The vent width $0.1H \leq D \leq 0.15H$ enhances buoyancy driven mixing between enclosures and nonlinear oscillations develops across horizontal vent. The vent width $D=0.2H$ reduces flow perturbations and facilitates balanced flow across the vent. Reduction in vent thickness results in early unification of convective cells and frequency of oscillations increases aiding better mixing rates between the enclosures. For turbulent combined convection flows in square cavity with inlet port, assisting flow case enhances thermal buoyancy, increases plume discharge rate through ceiling vent and decreases temperature distribution inside the square cavity. The opposing flow weakens thermal buoyancy, minimizes convective heat loss and reduces bidirectional exchange through ceiling vent.

The buoyant flows in naturally ventilated tunnel with roof openings highlighted the importance of ceiling vents in removing hot gases. For a tunnel with centrally mounted ceiling vent, as longitudinal distance between heat source and vent increases, plume discharge rate through ceiling vent decreases. The multiple roof vents are effective in reducing plume longitudinal velocity and decreases the temperature inside the tunnel. The ceiling vent discharge rate decreases by reducing vent size and temperature magnitudes rises inside the tunnel. In dual enclosures with bottom wall heat source, lower ventilation velocity through bottom enclosure doorway assists plume growth, while higher velocity diffuses the heat and reduces compartment temperature. Similarly, forced flow from upper enclosure doorway opposes the buoyancy force and reduces plume discharge through horizontal passage. When heat source is placed in top enclosure, the forced flow from top enclosure doorway accelerates the plume to propagate into the lower enclosure. The drag force from water droplets opposes thermal buoyancy force and sprinkler operating pressure of 1.6 bar leads to smoke logging. Hence, temperature inside the compartment decreases with sprinkler operating pressure. The present mathematical model and numerical method showed good agreement with the existing results available in literature.

In future, the study conducted in this thesis can be extended to include species reactions and radiation effects which are highly involved in fire situations. This work may be further extended to study bidirectional exchange through vents of different shapes.

References

- [1] W.G Brown and K.R. Solvason. Natural convection through rectangular openings in partitions-1: vertical partitions. *Int. J. Heat Mass Transfer* 5, (1962) 859–868.
- [2] F. Allard and Y. Utsumi. Airflow through large openings. *Energy Build* 18, (1992) 133–145.
- [3] J. Prahl and H.W. Emmons. Fire induced flow through an opening. *Combust. Flame* 25, (1975) 369–385.
- [4] J. Rockett. Fire induced gas flow in an enclosure. *Combust. Sci. Technol* 12, (1976) 165–175.
- [5] K.D. Steckler, J.G. Quintiere and W.J. Rinkinen. Flow induced by fire in a compartment. *Proceedings of the 19th International Symposium on Combustion* Combust. Inst. Pittsburgh. PA, (1962) 869–878.
- [6] H.W. Emmons. SFPE Handbook of Fire Protection Engineering, second ed. *Society of Fire Protection Engineers* Boston, MA 12, (1995).
- [7] W.B. Gosney and H.A.L. Olama. Heat and enthalpy gains through cold room doorways. *Proceedings of the Institute of Refrigeration* 72, (1975) 31–41.
- [8] Q.T. Pham and D.W. Oliver. Infiltration of air into cold stores. *Proceedings of the International Institute of Refrigeration* Paris, 4, (1983) 67–72.
- [9] M. Santamouris, A. Argiriou, D. Asimakopoulos, N. Klitsikas and A. Dounis. Heat and mass transfer through large openings by natural convection. *Energy Build.* 23, (1995) 1–8.
- [10] G.P. Mercier and Y. Jaluria. Fire-induced flow of smoke and hot gases in open vertical enclosures. *Exp. Therm. Fluid Sci.* 19, (1999) 77–84.
- [11] S.E. Ozcan, E. Vranken and E. Berckmans. Measuring ventilation rate through naturally ventilated air openings by introducing heat flux. *Building and Environment* 44, (2009) 27–33.

- [12] J. Tanny, V. Haslavsky and M. Teitel. Airflow and heat flux through the vertical opening of buoyancy-induced naturally ventilated enclosures. *Energy Build.* 40, (2008) 637–646.
- [13] A.H. Abib and Y. Jaluria. Numerical simulation of the buoyancy induced flow in a partially open enclosure. *Numer. Heat Transfer.* 14, (1988) 235–254.
- [14] W.K. Chow and G.W. Zou. Correlation equations on fire-induced air flow rates through doorway derived by large eddy simulation. *Build. Environ.* 40, (2005) 897–906.
- [15] P. Favarolo and H. Manz. Temperature-driven single-sided ventilation through a large rectangular opening. *Build. Environ.* 40, (2005) 689–699.
- [16] P. Ravikumar and D.Prakash. Analysis of thermal comfort in an office room by varying the dimensions of the windows on adjacent walls using CFD: A case study based on numerical simulation. *Building Simulation* 2, (2009) 187–196.
- [17] J.O. Cheung and C.H. Liu. CFD simulations of natural ventilation behaviour in high-rise buildings in regular and staggered arrangements at various spacings. *Energy and Buildings* 43, (2011) 1149–1158.
- [18] C. Allocca, Q. Chen and L.R. Glicksman. Design analysis of single-sided natural ventilation. *Energy and Buildings* 35, (2003) 785–795.
- [19] W. Brown. Natural convection through rectangular openings in partitions - 2: Vertical partitions. *Int. J. Heat Mass Transfer* 5, (1962) 295–299.
- [20] M. Epstein. Buoyancy-Driven Exchange Flow Through Small Openings in Horizontal Partitions. *Journal of Heat Transfer* 110, (1988) 885–893.
- [21] Y. Jaluria, S.H.K. Lee, G.P. Mercier and Q. Tan. Transport processes across a horizontal vent due to density and pressure differences. *Exp. Thermal Fluid Sci.* 16, (1998) 260–273.
- [22] Y. Jaluria, W.K.S. Chiu and S.H.K. Lee. Flow of smoke and hot gases across horizontal vents in room fires. *Combust. Sci. Technol.* 110-111, (1995) 197–208.
- [23] Q. Tan and Y.Jaluria. Mass flow through a horizontal vent in an enclosure due to pressure and density differences. *Int. J. Heat and Mass transfer.* 44, (2001) 1543–1553.
- [24] A.A Peppes, M. Santamouris and D.N. Asimakopoulos. Buoyancy-driven flow through a stairwell. *Building and Environment* 36, (2001) 167–180.

- [25] C. Blomqvist and M. Sandberg. Air movements through horizontal openings in buildings - a model study. *International Journal of Ventilation* 3 , (2004) 1–10.
- [26] P. Heiselberg and Z. Li. Experimental study of buoyancy driven natural ventilation through horizontal openings. *Proceedings of ROOMVENT Finland* 2 , (2007) 141–150.
- [27] P. Heiselberg and Z. Li. Buoyancy driven natural ventilation through horizontal openings. *Int. J. Vent.* 8 , (2009) 219–231.
- [28] S. Vera, P. Fazio and J. Rao. Interzonal air and moisture transport through large horizontal openings in a full-scale two-story test-hut: part 1 - experimental study. *Build. Environ.* 45 , (2010) 1192–1201.
- [29] C.F. Than and B. Savilonis. Modelling fire behaviour in an enclosure with a ceiling vent. *Fire Safety J.* 20 , (1993) 151–174.
- [30] L. Kerrison, E.R. Galea and M.K. Patel. A Two-dimensional Numerical Investigation of the Oscillatory Flow Behaviour in Rectangular Fire Compartments with a Single Horizontal Ceiling Vent. *Fire Safety J.* 30 , (1988) 357–382.
- [31] A.A. Mishra, Hasan Nadeem, Sanghi Sanjeev, Kumar Ranganathan. Two dimensional buoyancy driven thermal mixing in a horizontally partitioned adiabatic enclosure. *Phys Fluids.* 20 , (2008) 063601.
- [32] A.K. Sleiti. Effect of vent aspect ratio on unsteady laminar buoyant flow through rectangular vents in large enclosures. *Int J Heat Mass Transfer.* 51, (2008) 4850–4861.
- [33] A.K. Sleiti. Transient flow of air through rectangular vents in a horizontal partition. *HVAC&R Res.* 15, (2009) 1145–1163.
- [34] K. Venkatasubbaiah, Y. Jaluria. Numerical simulation of enclosure fires with horizontal vents. *Numer Heat Transfer Part A.* 62, (2012) 179–196.
- [35] W.K.Chow and Y.Gao. Buoyancy and inertial force on oscillations of thermalinduced convective flow across a vent. *Building and Environment* . 46, (2011) 315–323.
- [36] W.K.Chow and Y.Gao. Oscillating behaviour of fire-induced air flow through a ceiling vent. *Applied Thermal Engineering.* 29, (2009) 3289–3298.

- [37] J.M Holford and G.R. Hunt. Fundamental atrium design for natural ventilation. *Building and Environment* . 38, (2003) 409–426.
- [38] Y. Ji. Numerical studies of displacement natural ventilation in multi-storied buildings connected to an atrium. *Building Services Engineering Research and Technology*. 28, (2007) 207–222.
- [39] N.R. Marshall. The behavior of hot gases flowing within a staircase. *Fire Saf. J.* 9, (1985) 245–255.
- [40] N.R. Marshall. Air entrainment into smoke and hot gases in open shafts. *Fire Saf. J.* 10, (1986) 37–46.
- [41] J.Y.Zhang, J.Ji, R.Huo, H.Y.Yuan and R.Yang. A comparison of simulation and experiment on stack effect in long vertical shaft. *Journal of Fire Sciences*. 24, (2006) 121–136.
- [42] W.K.Chow and W.Y.Hung. On the fire safety for internal voids in high rise buildings. *Building and Environment* 38, (2003) 1317–1325.
- [43] F.Battaglia, K.B.McGrattan, R.G.Rehm and H.R.Baum. Simulating fire whirls. *Combustion Theory and Modelling* 4, (2000) 123–138.
- [44] G.R. Hunt and P.F Linden. The fluid mechanics of natural ventilation - displacement ventilation by buoyancy-driven flows assisted by wind. *Building and Environment* 34, (1999) 707–720.
- [45] M. Poreh and S. Trebukov. Wind effects on smoke motion in buildings. *Fire SafetyJournal* 35, (2000) 257–273.
- [46] W.Z. Lu, S.M. Lo, Z. Fang and K.K Yuen. A CFD Study of Air Movement in Designated Refuge Floor. *International Journal of Computational Fluid Dynamics* 15, (2001) 169–176.
- [47] C.C.K Cheng, K.M Lam, R.K.K Yuen, S.M. Lo and J. Liang. A study of natural ventilation in a refuge floor. *Building and Environment* 42, (2007) 3322–3332.
- [48] C.C.K Cheng, K.M Lam and F.N. Demirbilek. Effects of building wall arrangements on wind-induced ventilation through the refuge floor of a tall building *Journal of Wind Engineering and Industrial Aerodynamics* 96, (2008) 656–664.
- [49] Y. Li and A. Delsante. Natural ventilation induced by combined wind and thermal forces. *Building and Environment* 36, (2001) 59–71.

- [50] H. Chen, N.Liu and W. Chow. Wind effects on smoke motion and temperature of ventilation-controlled fire in a two-vent compartment. *Building and Environment* 44, (2009) 2521–2526.
- [51] K.T Andersen. Airflow rates by combined natural ventilation with opposing wind-unambiguous solutions for practical use. *Building and Environment* 42, (2007) 534–542.
- [52] P. Karava, T. Stathopoulos and A.K. Athienitis. Wind-induced natural ventilation analysis. *Solar Energy* 81, (2007) 20–30.
- [53] Z. Liu, B. Zhao and X.A. Yang. A Method for Calculating a Ventilation Bypass Factor *Indoor and Built Environment* 16, (2007) 472–481.
- [54] J. Lassus, L. Courty, J.P. Garo, E. Studer, P. Jourda and P. Aine. Ventilation effects in confined and mechanically ventilated fires. *International Journal of Thermal Sciences* 75, (2014) 87–94.
- [55] H. Huang, R. Ooka, N. Liu, L. Zhang, Z. Deng and S. Kato. Experimental study of fire growth in a reduced-scale compartment under different approaching external wind conditions. *Fire Safety Journal* 44, (2009) 311–321.
- [56] Y. Oka and G.T. Atkinson. Control of smoke flow in tunnel fires. *Fire Safety Journal* 25, (1995) 305–322.
- [57] S.R. Lee and H.S. Ryou. An experimental study of the effect of the aspect ratio on the critical velocity in longitudinal ventilation tunnel fires. *J.Fire Sci.* 23, (2005) 119–138.
- [58] G. Hyun Ko, S.R. Kim and H.S. Ryou . An experimental study on the effect of slope on the critical velocity in tunnel fires. *J.Fire Sci.* 28, (2010) 27–47.
- [59] K.C. Tsai, H.H. Chen and S.K. Lee. Critical ventilation velocity for multi-source tunnel fires. *J. Wind Eng. Ind. Aerodynam.* 98, (2010) 650–660.
- [60] Y. Wang, J. Jiang and D. Zhub. Diesel oil pool fire characteristic under natural ventilation conditions in tunnels with roof openings. *J.Hazard. Mater.* 166, (2009) 469–477.
- [61] Y. Wang, J. Jiang and D. Zhub. Full-scale experiment research and theoretical study for fires in tunnels with roof openings. *Fire Safety J.* 44, (2009) 339–348.
- [62] H. Yuan-dong, G.X. Lu, P.Y. Jiao, L.Xiao-yu and K.C. Nyung. Effects of the ventilation duct arrangement and duct geometry on ventilation performance in a subway tunnel. *Tunn. Undergr. Space Technol.* 26, (2011) 725–733.

- [63] J. Ji, Z.H. Gao, C.G. Fan, W. Zhong and J.H. Sun. A study of the effect of plugholing and boundary layer separation on natural ventilation with vertical shaft in urban road tunnel fires. *Int. J. Heat Mass Transfer.* 55, (2012) 6032–6041.
- [64] C.G. Fan, J. Ji, Z.H. Gao, J.Y. Han and J.H. Sun. Experimental study of air entrainment mode with natural ventilation using shafts in road tunnel fires. *Int. J. Heat Mass Transfer.* 56, (2013) 750–757.
- [65] W. Zhong, C.G. Fan, J. Ji and J.P. Yang. Influence of longitudinal wind on natural ventilation with vertical shaft in a road tunnel fire. *Int. J. Heat Mass Transfer.* 57, (2013) 671–678.
- [66] H. Ingason, Y.Z. Li. Model scale tunnel fire tests with point Extraction ventilation. *J. Fire Protect. Eng.* 21, (2011) 5–36.
- [67] L.F. Chen, L.H. Hu, W. Tang and L. Yi. Studies on buoyancy driven two directional smoke flow layering length with combination of point Extraction and longitudinal ventilation in tunnel fires. *J. Fire Protect. Eng.* 59, (2013) 94–101.
- [68] N.C. Markatos, K.A. Pericleous. Laminar and turbulent natural convection in an enclosed cavity. *Int. J. Heat Mass Transfer* 27, (1984) 755–772.
- [69] M.J. Cook and K.J. Lomas. Buoyancy-driven displacement ventilation flows: Evaluation of two eddy viscosity models for prediction. *Building Services Engineering Research and Technology* 19, (1998) 15–21.
- [70] G.M. Stavrakakis, N.C. Markatos, Simulation of airflow in one- and two-room enclosures containing a fire source. *Int. J. Heat Mass Transfer* 52, (2009) 2690–2703.
- [71] S. Kenjeres and K.Hanjalic. Transient analysis of Rayleigh-Benard convection with a RANS model. *International Journal of Heat and Fluid Flow* 20, (1999) 329–340.
- [72] S. Kenjeres and K.Hanjalic. Convective rolls and heat transfer in finite-length Rayleigh-Benard convection: a two-dimensional numerical study. *Physical Review E* 62, (2000) 7987–7998.
- [73] S. Kenjeres, S.B.Gunarjo and K.Hanjalic. Contribution to elliptic relaxation modelling of turbulent natural and mixed convection. *International Journal of Heat and Fluid Flow* 26, (2005) 569–586.
- [74] S. Kenjeres and K.Hanjalic. Tackling complex turbulent flows with transient RANS. *Fluid Dynamics Research* 41, (2009) 1–32.

- [75] Anil Kumar Sharma and K. Velusamy. Interaction of turbulent natural convection and surface thermal radiation in inclined square enclosures. *Heat and Mass Transfer* 44, (2010) 1153–1170.
- [76] J. Xaman, J. Arce, G. Alvarez and Y. Chavez. Laminar and turbulent natural convection combined with surface thermal radiation in a square cavity with a glass wall. *Int. J. Therm. Sci.* 47, (2008) 1630–1638.
- [77] G.V. Kuznetsov and M.A. Sheremet. Numerical simulation of turbulent natural convection in a rectangular enclosure having finite thickness walls. *Int. J. Heat Mass Transfer*. 53, (2010) 163–177.
- [78] A.H. Abib and Y. Jaluria. Turbulent penetrative and recirculating flow in a compartment fire. *J. Heat Transfer*. 117, (1995) 927–935.
- [79] Lars Davidson. Calculation of the turbulent buoyancy driven flow in a rectangular cavity using an efficient solver and two different low reynolds number $k - \varepsilon$ turbulence models. *Numer. Heat Transfer A*. 18, (1990) 129–147.
- [80] Akhilesh Gupta, V. Eswaran, Prabhat Munshi, N.K. Maheshwari and P.K. Vijayan. Thermal stratification studies in a side heated water pool for advanced heavy water reactor applications. *Heat and Mass Transfer* 45, (2009) 275–285.
- [81] W.Zhang and Q. Chen. Large eddy simulation of indoor airflow with a filtered dynamic subgrid scale model. *International Journal of Heat and Mass Transfer* 43, (2000) 3219–3231.
- [82] H. Hu, R. Huo and D. Yang. Large eddy simulation of fire-induced buoyancy driven plume dispersion in an urban street canyon under perpendicular wind flow. *Journal of Hazardous Materials* 166, (2009) 394–406.
- [83] W.K. Chow and G.W. Zou. Correlation equations on fire-induced air flow rates through doorway derived by large eddy simulation. *Building and Environment* 40, (2005) 897–906.
- [84] S. Gavrilakis. Numerical simulation of low-Reynolds-number turbulent flow through a straight square duct. *J. Fluid Mech* 244, (1992) 101–129.
- [85] Karim Van Maele and Bart Merci. Application of two buoyancy-modified $k - \varepsilon$ turbulence models to different types of buoyant plumes. *Fire Safety J* 41, (2006) 122–138.
- [86] S.J. Wang and A.S. Mujumdar. A comparative study of five low Reynolds number $k - \varepsilon$ models for impingement heat transfer. *Appl. Therm. Eng* 25, (2005) 31–44.

- [87] C.W. Li and B. Zhu. A Sigma coordinate 3D $k-\varepsilon$ model for turbulent free surface flow over a submerged structure. *Appl. Math. Model.* 26, (2002) 1139–1150.
- [88] N.G. Wright and G.J. Easom. Non-linear $k-\varepsilon$ turbulence model results for flow over a building at full-scale. *Appl. Math. Model.* 27, (2003) 1013–1033.
- [89] Jamel Kechiche, Hatem Mhiri, Georges Le Palec and Philippe Bournot. Application of low Reynolds number $k-\varepsilon$ turbulence models to the study of turbulent wall jets. *Int. J. Therm. Sci.* 43, (2004) 201–211.
- [90] Vierendeels Jan, Merci Bart and Dick Erik. Numerical study of natural convective heat transfer with large temperature differences. *Int J Numer Method Heat Fluid Flow* . 11, (2001) 329–341.
- [91] Becker Roland and Braack Malte. Solution of a stationary benchmark problem for natural convection with large temperature difference. *Int J Therm Sci.* 41, (2002) 428–439.
- [92] T. Pessa and S.Piva. Laminar natural convection in a square cavity: low Prandtl numbers and large density differences. *Int J Heat Mass Transfer* 52, (2009) 1036–1043.
- [93] K. Szewc, J. Pozorski and A.Taniere. Modeling of natural convection with smoothed particle hydrodynamics: non-Boussinesq formulation. *Int J Heat Mass Transfer* 54, (2011) 4807–4816.
- [94] P. Kumar and V. Eswaran. A Numerical Simulation of Combined Radiation and Natural Convection in a Differential Heated Cubic Cavity. *J. Heat Transfer* 132, (2009) 023501.
- [95] E. Sourtiji, S.F. Hosseinizadeh and M. Gorji-Bandpy. Numerical simulation of compressible high gradient thermobuoyant flow in square enclosures with localized heating from below. *Int Commun Heat Mass Transfer* 39, (2012) 987–994.
- [96] P. Venkata Reddy, G.S.V.L. Narasimham, S.V. Raghurama Rao, T. Johny, and K.V. Kasiviswanathan. Non-Boussinesq conjugate natural convection in a vertical annulus *Int Commun Heat Mass Transfer* 37, (2010) 1230–1237.
- [97] T.K.Sengupta, S.K.Sirkar and A.Dipankar. High accuracy schemes for DNS and acoustics. *J. Sci. Comput.* 26, (2006) 151–193..
- [98] H.N. Dixit and V. Babu. Simulation of high Rayleigh number natural convection in a square cavity using the lattice Boltzmann method. *Int. J. Heat Mass Transfer* 49, (2006) 727–739.

- [99] Y.S.Tian and T.G. Karayiannis. Low turbulence natural convection in an air filled square cavity part I: the thermal and fluid flow fields. *Int. J. Heat Mass Transfer* 43, (2000) 849–866.
- [100] J.P.Xaman,J.F.Hinojosa,J.J.Flores and R.E.Cabanillas. Effect of surface thermal radiation and turbulent natural convection in tall cavities of facade elements. *Heat and Mass Transfer* 45, (2008) 177–185.
- [101] P.L.Betts and I.H.Bokhari. Experiments on turbulent natural convection in an enclosed tall cavity. *Int. J. Heat Mass Transfer* 21, (2000) 675–683.
- [102] Vierendeels Jan, Merci Bart and Dick Erik. Numerical study of natural convective heat transfer with large temperature differences. *Int J Numer Method Heat Fluid Flow* 11, (2001) 329–341.
- [103] Becker Roland and Braack Malte. Solution of a stationary benchmark problem for natural convection with large temperature difference. *Int J Therm Sci* 41, (2002) 428–439.
- [104] L.F. Chen, L.H Hu, W.Tang and L.Yi. Studies on buoyancy driven two directional smoke flow layering length with combination of point extraction and longitudinal ventilation in tunnel fires. *Fire Safety J.* 59, (2013) 94–101.
- [105] K. McGrattan, S. Hostikka, J. Floyd, H. Baum, R. Rehm. Fire Dynamics Simulator (Version 5) Technical Reference Guide. NIST Special Publication. *NIST Special Publication* (2007) 1018.
- [106] K. McGrattan, B. Klein, S. Hostikka, J. Floyd. Fire Dynamics Simulator (Version 5) Users Guide. *NIST Special Publication* (2007) 1019.